Title

Semiconducting Half-Heusler Based Compounds and Heterostructures Grown by Molecular Beam Epitaxy

Permalink

https://escholarship.org/uc/item/6184m7kb

Author

Harrington, Sean David

Publication Date

2018

Peer reviewed|Thesis/dissertation

UNIVERSITY of CALIFORNIA
Santa Barbara

Semiconducting Half-Heusler Based Compounds and Heterostructures Grown by Molecular Beam Epitaxy

A Dissertation submitted in partial satisfaction of the
requirements for the degree

Doctor of Philosophy
in
Materials

by

Sean David Harrington

Committee in charge:

Professor Christopher Palmstrøm, Chair
Professor Arthur Gossard
Professor Ram Seshadri
Professor James Allen

March 2018

The dissertation of Sean David Harrington is approved.

Arthur Gossard

Ram Seshadri

James Allen

Christopher Palmstrøm, Chair

February 2018

Semiconducting Half-Heusler Based Compounds and Heterostructures Grown
by Molecular Beam Epitaxy

by

Sean David Harrington

Acknowledgements

The work presented in this dissertation would not have been possible without the guidance and support of many people and groups. First and foremost, I'd like to thank my adviser, Professor Chris Palmstrøm. Through the years, Chris has provided me an enormous amount of direction while still giving me the autonomy necessary to grow as an independent researcher. Chris' expertise in science and technology, and in particular vacuum equipment, has never ceased to amaze me. I have come to realize though that much of this expertise has been attained by his willingness to tackle any problem head on, a trait that I have tried to embrace. Beyond Chris, I'd also like to thank my other committee members: Professors Arthur Gossard, Jim Allen, and Ram Seshadri for their assistance and unique perspectives on my research projects.

Thank you to all the Palmstrøm lab members, past and present, who I have had the privilege to work with: Alex, Anisa, Anthony, Aranya, Bo, Brian, Dan, Elliot, Hadass, Jay, Jason, Javad, Joon Sue, Michelle, Mihir, Mitchell, Nate, Rachel, Ryan, Sahil, Shouvik, Sukgeun, Tobias, and Tony. Working alongside such a great group of individuals has made tackling the challenges of such a large interconnected UHV system a much more manageable feat. In particular, I would like to thank Jay for being a great scientific companion from the beginning, navigating classes, multiple week long beamline sessions, lengthy discussions, and many late nights working on UHV equipment.

Beyond our lab, I'd like to thank the UCSB MBE community. In particular, I'd like to thank John English and Kurt Olsson for their help and advice while tackling my experimental challenges, even though our lab is well outside their job description. The weekly MBE meetings have been an excellent learning experience, giving me the opportunity to learn about MBE of other material systems, as well as provided feedback and a different perspective on my research projects. In addition, the support staff of CNSI and Nanofab were vital to keep the characterization and fabrication tools up and running despite how many used the equipment.

Much of the research presented in this thesis has been done in collaboration with individuals outside of the Palmstrom group, and I would like to thank all those I had the privilege to collaborate with. Our Lund collaborators including Anderson Mikkelson, Johan Knutsson, and the beamline scientists Balu Thiagarajan and Craig Polley were incredibly helpful in making our time in Lund productive and enjoyable. In addition, calculations provided by Abhishek Sharan and Anderson Janotti gave insight and support to a number of the experiments presented here. Finally, the Fe doped CoTiSb project received not only inspiration but a large amount of experimental support from a number of individuals including, Leyla Colakerol Arslan, Andre Petukhov, and Bastien Bonef.

Outside of work, I have had the opportunity to gain close friendships with a number of people, giving me something else to think and talk about when research was not going well. My roommates Brian, Drew, Jared, and Stefan always made home an enjoyable place to be. In addition, the UCSB Triathlon team has been a huge part of my time in Santa Barbara. In particular my coaches Mateo and Matt and teammates Jon, Nirala, and Will (as well as many others) have been incredibly supportive as well as just generally fun to be around, making my time at UCSB incredibly memorable.

Finally, I would like to thank my parents John and Susan, my brothers Scott and Erik, my girlfriend Laura, and the rest of my family for their encouragement, love, and unwavering support through the years. I can't say how much I have appreciated their patience and continual interest in what I have been doing that last six years of my life, even if they did not fully understand it themselves.

Curriculum Vitæ

Sean David Harrington

EDUCATION

Doctor of Philosophy in Materials Engineering, 2018
University of California, Santa Barbara
Adviser: Christopher J. Palmstrøm

Bachelor of Science in Physics with Optics Emphasis, 2011
University of Wisconsin, La Crosse

Bachelor of Science in Mathematics, 2011
University of Wisconsin, La Crosse

WORK EXPERIENCE

Graduate Student Researcher
University of California, Santa Barbara, 2012 - Present
Adviser: Professor Christopher J. Palmstrøm

National Lab Researcher
National Institute of Standards and Technology (NIST), 2012
Supervisor: Rich Mirin, PhD

Undergraduate Student Researcher
University of Wisconsin, La Crosse, 2008 - 2011
Adviser: Professor Eric Gansen

Summer Undergraduate Research Fellowship
National Institute of Standards and Technology (NIST), 2011
Mentor: Martin Stevens, PhD

Electrical Engineering Intern
Engineering Solutions Experts (ESE) Automation, 2008

AWARDS

AVS Dorthy M. and Earl S. Hoffman Travel Grant
October, 2017

PCSI 2016 Young Scientist Award
January, 2016

Best Student Oral Presentation *NAMBE 2015*
Epitaxial growth and electronic structure of $Co_{1-x}Ni_xTiSb$
October, 2015

International Center for Materials Research Fellowship
June 2014, January 2015

National Science Foundation Graduate Research Fellowship
April, 2012

TEACHING EXPERIENCE

Graduate student mentor for undergraduate students Aamir Shahzad, Vinh Ta, and Mayer Feldman 2014 - 2017

Teaching assistant for MAT 100A (Introduction to Materials Science) with James Speck at University of California, Santa Barbara, Winter, 2014

Physics and Mathematics Tutor at the University of Wisconsin, La Crosse - 2008 - 2012

PUBLICATIONS

"Nanometer scale structural and compositional homogeneities of half-Heusler $CoTi_{1-x}Fe_xSb$ thin films", B. Bonef, **S.D. Harrington**, D.J. Pennachio, J.S. Speck, C.J. Palmstrøm. *In Preparation*

"Epitaxial growth and electronic structure of half-Heusler $Co_{1-x}Ni_xTiSb$", **S.D. Harrington**, J.A. Logan, S. Chatterjee, S.J. Patel, A.D. Rice, M.M. Feldman, C.M. Polley, T. Balasubramanian, A. Mikkelsen, and C.J. Palmstrøm. *Applied Physics Letters In Preparation*

"Surface Reconstructions in the Ni-Ti-Sn System" Anthony Rice, Nate Wilson, **Sean Harrington**, and Chris Palmstrøm. *Journal of Vacuum Science and Technology:B In Preparation.*

"Growth, electrical, structural, and magnetic properties of half-Heusler $\mathrm{CoTi}_{1-x}\mathrm{Fe}_x\mathrm{Sb}$", **S.D. Harrington**, A.D. Rice, T.L. Brown-Heft, B. Bonef, A.P. McFadden, J.A. Logan, M. Pendharkar, M.M. Feldman, O. Mercan, A.G. Petukhov, L. Colakerol Arslan, and C.J. Palmstrøm. *Physical Review Materials* **2**, 014406 (2018).

"Valence-band Offsets of CoTiSb/$\mathrm{In}_{0.53}\mathrm{Ga}_{0.47}\mathrm{As}$ and CoTiSb/$\mathrm{In}_{0.52}\mathrm{Al}_{0.48}\mathrm{As}$ Heterojunctions " **S.D. Harrington**, A. Sharan, A.D. Rice, J.A. Logan, A.P. McFadden, M. Pendharkar, D. Pennachio, N.S. Wilson, Z. Gui, A. Janotti, and C.J. Palmstrøm. *Applied Physics Letters* **111**, 061605 (2017).

"Growth, Structural, and Magnetic Properties of Single-Crystal $\mathrm{Co}_2\mathrm{TiGe}$ Thin Films" J.A. Logan, T.L. Brown-Heft, **S.D. Harrington**, N.S. Wilson, A.P. McFadden, A.D. Rice, M. Pendharkar, and C.J. Palmstrøm. *Journal of Applied Physics* **121**, 213903 (2017).

"Observation of a topologically non-trivial surface state in half-Heusler PtLuSb (001) thin films" J.A. Logan, S.J. Patel, **S.D. Harrington**, C.M. Polley, B.D. Schultz, T. Balasubramanian, A. Janotti, A. Mikkelsen, and C.J. Palmstrøm. *Nat. Commun.* **7**, 11993 (2016).

"Surface reconstructions and transport of epitaxial PtLuSb (001) thin films grown by MBE" S.J. Patel, J.A. Logan, **S.D. Harrington**, B.D. Schultz, and C.J. Palmstrøm. *J. Cryst. Growth* **436**, 145 (2016).

"Temperature dependence of the single-photon sensitivity of a quantum dot, optically gated, field-effect transistor" E.J. Gansen, M.A. Rowe, **S.D. Harrington**, J.M. Nehls, S.M. Etzel, S.W. Nam, R.P. Mirin *Journal of Applied Physics* **114**, 093103 (2013).

"Detecting single infrared photons with 93% system efficiency", F. Marsili, V. B. Verma, J. A. Stern, **S.D. Harrington**, A.E. Lita, T. Gerrits, I. Vayshenker, B. Baek, M.D. Shaw, R.P. Mirin, and S.W. Nam. *Nat. Photonics* **7**, 210 (2013).

"A three-dimensional, polarization-insensitive superconducting nanowire avalanche photodetector", V. B. Verma, F. Marsili, **S.D. Harrington**, A.E. Lita, R.P. Mirin, and S.W. Nam. *Applied Physics Letters* **101**, 251114 (2012).

Conference Presentations

“Measurement of band-alignments in semiconducting half-Heusler heterojunctions grown by MBE” **S.D. Harrington**, A.D. Rice, A.P. McFadden, D.J. Pennachio, M.M. Feldman, M. Pendharkar, A. Sharan, A. Janotti, and C.J. Palmstrøm. *Physics and Chemistry of Surfaces and Interfaces.* Kona, HI, USA (2018).

“Growth, electronic, structural, and magnetic properties of half-Heusler $\mathrm{CoTi}_{1-x}\mathrm{Fe}_x\mathrm{Sb}$” **S.D. Harrington**, A.D. Rice, T.L. Brown-Heft, B. Bonef, A.P. McFadden, J.A. Logan, M. Pendharkar, M.M. Feldman, O. Mercan, A.G. Petukhov, and C.J. Palmstrøm. *AVS 64th International Symposium & Exhibition.* Tampa, FL, USA (2017).

“Semiconducting Half-Heusler Heterostructures Grown by Molecular Beam Epitaxy” A.D. Rice, **S.D. Harrington**, D.J. Pennachio, M. Pendharkar, and C.J. Palmstrøm. *AVS 64th International Symposium & Exhibition.* Tampa, FL, USA (2017).

“Growth and characterization of half-Heusler half-metal candidate $\mathrm{CoTi}_{1-x}\mathrm{Fe}_x\mathrm{Sb}$” **S.D. Harrington**, T. Brown-Heft, A.D. Rice, O. Mercan, L. Olakerol Arslan, and C.J. Palmstrøm. *American Physical Society March Meeting.* New Orleans, LA, USA (2017).

“Investigation of the Half-Heusler CoTiSb/III-V Heterointerfaces” **S.D. Harrington**, A.D. Rice, T. McFadden, J.K. Kawasaki and C.J. Palmstrøm. *Physics and Chemistry of Surfaces and Interfaces.* Palm Springs, CA, USA (2016).

“Growth and electronic structure of half-Heusler $\mathrm{Co}_{1-x}\mathrm{Ni}_x\mathrm{TiSb}$” **S.D. Harrington**, J.A. Logan, S.J. Patel, J.K. Kawasaki, T. Balasubramanian, A. Mikkelson, and C.J. Palmstrøm. *North American Molecular Beam Epitaxy Conference.* Mayan Riviera, Mexico (2015).

“Epitaxial growth and electronic structure of half-Heusler $\mathrm{Co}_{1-x}\mathrm{Ni}_x\mathrm{TiSb}$” **S.D. Harrington**,J.A. Logan, S.J. Patel, J.K. Kawasaki, T. Balasubramanian, A. Mikkelson, and C.J. Palmstrøm. *Physics and Chemistry of Surfaces and Interfaces.* Snowbird, UT (2015).

Abstract

Semiconducting Half-Heusler Based Compounds and Heterostructures Grown by Molecular Beam Epitaxy

by

Sean David Harrington

Heusler compounds are an exciting class of intermetallics due to their diverse electrical and magnetic properties, including semiconducting, half metallic, and topologically insulating behaviors. With a crystal structure and lattice parameters similar to III-V compound semiconductors, the possibility of Heusler/III-V semiconductor as well as Heusler/Heusler heterostructures with unique properties is achievable. However, the integration of epitaxial Heusler compounds into functional devices still faces a number of challenges. The tunability of the electronic and magnetic properties of Heusler compounds must first be better understood. In addition, Heusler-based device demonstrations have been limited to magnetic Heuslers, leaving the semiconducting and topologically non-trivial variants relatively unexplored. Finally, most experimental studies of the semiconducting half-Heusler compounds have been limited to bulk polycrystalline samples, which cannot be easily used for device applications.

Here, the semiconducting half-Heusler, CoTiSb is grown by molecular beam epitaxy and used to explore the both the tunability of Heusler compound properties as well as the interface properties of Heusler alloys with III-V and other Heusler compounds. A semiconductor to metal transition is examined by substitutionally alloying Ni for Co. The evolution of the electronic structure in the alloy $Co_{1-x}Ni_xTiSb$ is examined by electrical transport, Seebeck measurements, and angle-resolved photoemission spectroscopy. A gradual transition from semiconducting to metallic behavior is observed for films with $x \geq 0.1$. The effects of

Ni alloying as well as the surface reconstruction on the valence band, conduction band, and Fermi level positions are examined.

Next, the introduction of ferromagnetism into CoTiSb is achieved by substitutionally alloying Fe on the Ti site, a predicted half-metallic compound for intermediate levels of alloying. The magnetic, electronic, and nano-structural properties of the epitaxial thin films are shown to depend strongly on Fe composition. In particular, a large dependence of the magnetic moment on the site which Fe atoms occupy is found. In addition, evidence of nano-level phase separation is observed and shows a clear compositional dependence.

Finally, the band alignments between CoTiSb and the III-V compounds InAlAs and InGaAs as well as another semiconducting half-Heusler, NiTiSn, are explored using a combination of X-ray photoemission spectroscopy, density functional theory (DFT), and electrical transport. Here good agreement is found for the valence band offsets between the three techniques. However, a discrepancy between the conduction band offsets predicted by DFT and those inferred from electrical transport is found. An effective reduction in the CoTiSb bandgap is used to explain this discrepancy.

This work ultimately advances the current understanding of the tunability of Heusler compounds and lays the foundation for future Heusler based heterostructure devices.

Contents

Chapter 1

Semiconducting half-Heusler Based Compounds

1.1 Introduction

While silicon based electronics are the most prolific technology within modern society, many other technologies rely on properties not attainable by silicon alone. In particular, the combination of different III-V materials into heterostructures have enabled devices such as the laser, infrared detectors, and the high electron mobility transistor, as well as the discovery of fundamentally new physics that would not be possible with one singular material. For example, the formation of a two-dimensional electron-gas (2DEG) at the interface between GaAs and AlGaAs has enabled numerous technologies, but more importantly allowed for careful studies of low-dimensional physics ultimately leading to the discovery of the fractional quantum hall effect [1]. Additional functionality can be introduced by utilizing a different material system that offers additional properties as the fundamental building block of such heterostructures. One class of materials that demonstrates promise for many immediate and more exotic applications are Heusler compounds, a family of materials which exhibits many different electronic and magnetic properties.

1.2 Heusler Compounds

Heusler compounds are a large group of ternary intermetallic compounds that have attracted a growing interest due to their diverse properties [2]. They typically consist of two transition metals (X,Y) and one main group element (Z) and crystallize in two related, but distinct crystal structures: $L2_1$ full-Heusler with chemical formula X_2YZ and $C1_b$ half-Heusler with chemical formula XYZ. These compounds consist of four interpenetrating face-center cubic (FCC) lattices with the element Z at Wycloff position 4a (0,0,0) and element Y at Wycloff position 4b ($\frac{1}{2}$,$\frac{1}{2}$,$\frac{1}{2}$). For the full-Heusler, element X occupies both the Wycloff positions 4c ($\frac{1}{4}$,$\frac{1}{4}$,$\frac{1}{4}$) at 4d($\frac{3}{4}$,$\frac{3}{4}$,$\frac{3}{4}$), while for the half-Heusler the element X only occupies the 4c position and the 4d is vacant. The full Heusler structure can be viewed as a rocksalt structure made up of the Y and Z atoms with all of the tetrahedral sites occupied by X atoms. In contrast, the half-Heusler crystal structure can be thought of as a zinc blende lattice made up of the X and Z atoms with the octahedral sites filled with Y atoms. This is shown in Fig. 1.1.

There are over 1000 known compounds within the Heusler family [2]. This originates from the large number of elemental constituents that can form in one of the Heusler crystal structures. Figure 1.2 shows the possible elements that can comprise the Heusler compound, color coded by the site occupancy. Here it can be seen that, in general, X atoms are transition metals, Y atoms are rare earth or transition metals, and Z atoms are group III, IV, or VI elements. The large number of possible combinations of these elements give rise to the multitude of known and predicted phase stable compounds.

Perhaps unsurprisingly, the properties of the resulting compounds formed from different combinations of elements varies immensely depending on the con-

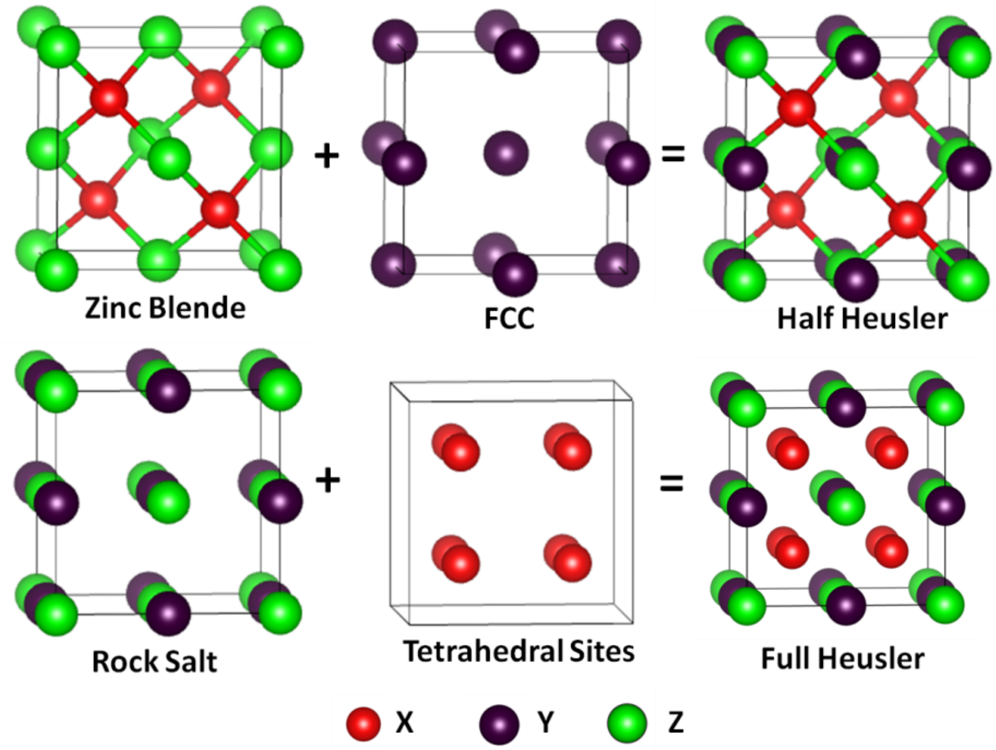

Figure 1.1. Crystal structures of half (XYZ) and full (X_2YZ) Heusler compounds. The half-Heusler crystal structure can be thought of as zinc blende structure made up of the X and Z atoms with the octahedral sites filled with Y atoms. The full Heusler structure can be viewed as a rocksalt structure made up of the Y and Z atoms with all the tetrahedral sites occupied by X atoms.

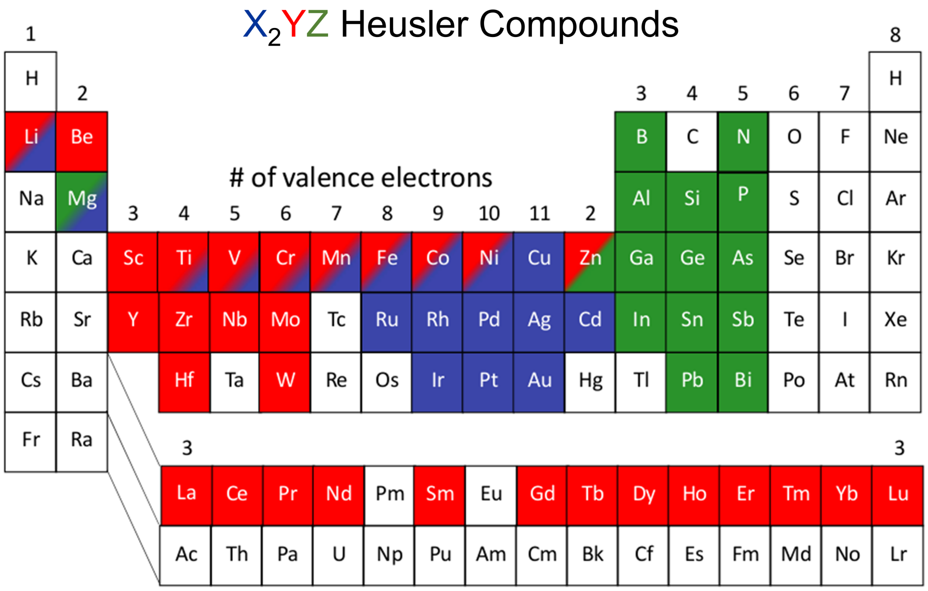

Figure 1.2. Periodic table highlighting the site occupancy by element in the Heusler crystal structure. Reprinted from [3] with permission from *Elsevier*.

stituents present. Some of the properties include half-metallic ferromagnetism[4–6], semiconducting behavior [7–9], topologically non-trivial bandstructures [10–14], and superconductivity [15, 16]. In addition, Heusler compounds have been shown to exhibit shape memory effects [17, 18], high thermoelectric figures of merit [19–21], and heavy fermion behavior [22]. All of these properties are accessible within the same crystal structure making them exciting for both future technologies as well as understanding fundamental material physics. In addition, the properties depend strongly on the total valence count per formula unit [2] (see Figure 1.3. For example, half-Heusler materials with 8 or 18 valence electrons per formula unit are predicted to exhibit semiconducting behavior where the size of the bandgap is related to the difference in the Pauling electronegativity between the X and Z atom for a given element Y. By substituting one of the sites with an element having one less or one more electron, 17 and 19 valence electron compounds are generated, respectively. Consequently, various types of insulator-to-metal transitions, accompanied by a crossover from diamagnetism

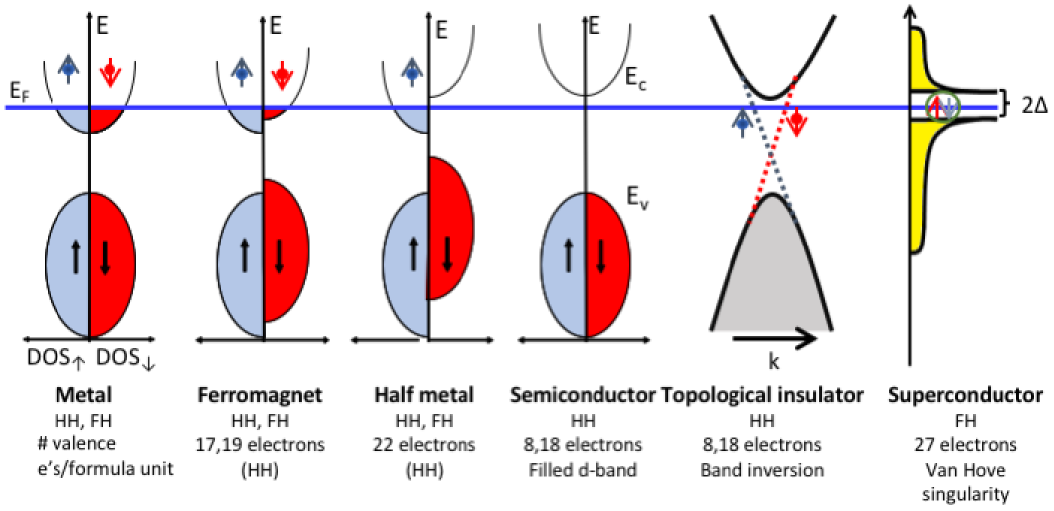

Figure 1.3. Schematic representation of the electronic and magnetic properties of Heusler compounds as a function of electron count. Adapted from [3] with permission from *Elsevier*.

to paramagnetism or ferromagnetism are observed as the electron count is varied [23].

Heusler alloys are promising materials for a variety of applications due to their properties not typically observed in mainstream compound semiconductors. These diverse properties offer an exciting platform to study novel phenomenon. Heusler compounds have already demonstrated promising results for a number of fields. High ZT values (>1 at elevated temperatures) have been reported for semiconductor-based thermoelectrics[24–26]. Compared to other high-ZT material systems, half-Heusler based thermoelectrics have a relatively high lattice contribution to the thermal conductivity, leaving room for significant improvement. Moreover, the primary constituent elements of half-Heusler thermoelectrics (e.g. NiTiSn) are relatively inexpensive, non-toxic, and abundant.

The half-metallic behavior of a number of Heusler compounds is particularly attractive in the field of spintronics, which makes use of the electron's spin-degree of freedom. Spin-based technologies are theorized to offer nonvolatile data storage, increased data processing speed and storage, and lower energy consumption [27]. However, the development of new magnetic materials, including magnetic semiconductors and half-metallic ferromagnets, is paramount to realizing the full potential of spintronics. Half-metals are particularly important in this regard because of their complete spin polarization at the Fermi level. This property makes half-metals ideal candidates for spin injection or detection in spintronic devices that will rely on high spin polarized currents. Heusler compound half-metals have demonstrated much promise by using their tunable electronic and magnetic properties. Co_2-based (i.e. Co_2XZ) Heusler materials have been intensely studied due to their high potential as electrode materials in spintronic devices, such as magnetic tunnel junctions (MTJs) [28–32], giant magnetoresistance (GMR) [33–35], and for spin injection from ferromagnetic electrodes into semiconductors [36]. For all of these device applications, a true half-metal with a Fermi level spin polarization approaching 100% is desired. However, early experiments that sought to measure spin polarization using spin polarized photoemission (SSPES) [37], point contact Andreev reflection (PCAR) [38, 39], and spin polarized tunneling [40] all resulted in measured spin polarizations significantly less than the predicted 100%. The observed lower polarization have largely been attributed to the lack of half-metallicity at surfaces and interfaces as well as other bulk depolarizing effects including disorder, defects, and sample quality.

To reduce these depolarizing effects and increase resulting device performance, a number of methods have been studied. One method explored is using alternative surface terminations (e.g. Mn terminated Co_2MnSi [41]) or interface orientations such as Co_2CrAl/GaAs(110) [42]. Another method is to tune the band structure and magnetism by substitutional alloying on one of the sites of the ternary Heusler with a fourth element. This method has produced promising results both theoretically and experimentally [43–48]. The improvement in room temperature polarization is often the result of tuning the Fermi level to the middle of the minority spin gap, which is typically less than 1 eV. By implementing this strategy, MTJs have demonstrated room temperature tunneling magnetoresistance (TMR) of greater than 100% [49–51] and temperature-dependent TMR ratios consistent with the Fermi level being at the center of the minority gap [52]. Although the room temperature TMR values are good indications of device performance and the applicability of Fermi level tuning, they are only an indirect measure of the electronic structure.

An exciting increase in research has been focused on the identification and observation of topologically non-trivial behavior after the prediction of topological insulators within the half-Heusler family[11, 53] and recent observation of topologically non-trial surface states[12]. Topological insulators could prove instrumental for spintronic devices and quantum computing. Moreover, being able to tune the Fermi level to the Dirac point through doping has already been demonstrated for Bi_2Se_3, a 3D topological insulator [54], and could prove an effective, and necessary, method to not only observe, but also integrate Heusler topological insulators into usable devices.

Beyond the diverse and tunable magnetic and electronic properties, Heusler compounds have lattice parameters and crystal structures that are compatible with conventional III-V semiconductors. In particular, the cubic Heusler crystal structure, consisting of interpenetrating FCC lattices, has similar symmetry to conventional zinc-blende and diamond crystal structures of III-V and elemental semiconductors, respectively. In addition, the lattice parameters found within the Heusler family span a large number of III-V compound lattice parameters, highlighted in Figure 1.4, enabling a number of existing III-V and oxide substrates. A continuous FCC sublattice, and good lattice matching promote epitaxial growth and enable the formation of atomically abrupt interfaces. This allows for the epitaxial growth of III-V/Heusler heterostructures and novel devices. Molecular beam epitaxy (MBE) is well suited for this task due to the high-quality thin films it produces. Additionally, it allows for atomic level control of surfaces and interfaces, critical for the fabrication of devices where interfaces can have large effects on performance. MBE has already been used to demonstrate the successful growth of high-quality magnetic films on III-Vs including NiMnSb on InGaAs[55], Ni_2MnAl on GaAs[56], and Co_2MnSi on GaAs[57]. Beyond the magnetic Heuslers, high quality 18 valence electron half-Heuslers, which display both semiconducting and topologically insulating behavior, have been demon-

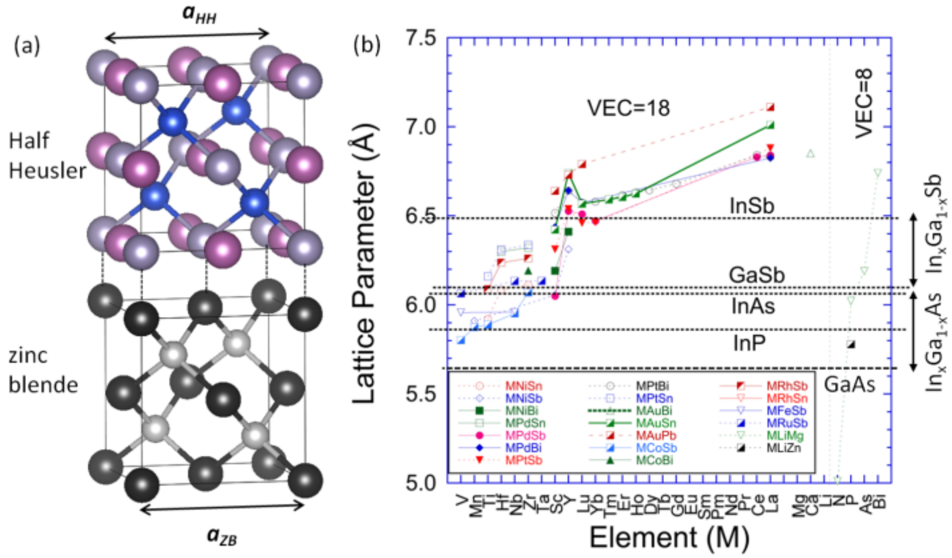

Figure 1.4. (a) Schematic diagram of the half-Heusler (001) compound grown epitaxial on a III-V (001) zinc blende layer. (b) Lattice parameters of various 8 and 18 valence electron per formula unit half-Heusler compounds plotted for a number of different elemental constituents. Also included are relevant III-V materials and their associated lattice parameter. Reprinted from [60] with permission from J. Kawasaki.

strated on InAlAs[58] and InAlSb[59] buffer layers, respectively.

1.2.1 Semiconducting Half-Heusler Compounds

As previously mentioned, half-Heuslers with 8 or 18 valence electrons per formula unit frequently show bandgaps. In these compounds, the bandgap originates from filled s, p, and d (only in the case of the 18) electron shells. The predicted bandgaps range in size from 0 to 4 eV [2] and have been suggested to originate from a covalent like bonding formed between the X and Z elemental sublattices [61] and more ionic bonding with the Y sublattice. For example, for CoTiSb, Co and Sb would form a zinc-blende structure $[CoSb]^{4-}$ stuffed with a Ti^{4+} sublattice [2]. Here the $[CoSb]^{4-}$ sublattice is isoelectronic and isostructural with zinc blende GaSb.

Most studies to date have focused on the thermoelectric properties, where simultaneous low electrical resistivity and low thermal conductivity are desirable.

To this end, the effects of isovalent and aliovalent substitutional alloying has been investigated to try and maximize these thermoelectric properties [24, 62–67]. Unfortunately, many of the properties that make a material a good thermoelectric resemble a poor metal rather than a semiconductor. Thus the defects that may improve thermoelectric performance may be a detriment for other semiconductor applications. Previous studies on half-Heusler based semiconductors have found only weak temperature dependence on resitivity, high carrier densities (typically n> 10^{20} cm^{-3}), and low carrier mobilites (<100 cm^2/V s) [63, 67–71]. These poor charge transport properties have been largely attributed to defects and deviations from intended stoichiometry [72–74].

Among the semiconducting half-Heusler compounds, CoTiSb and NiTiSn, as well as related alloys, have received the most attention within the literature due to their promising thermoelectric properties. Using the generalized gradient approximation (GGA) within density functional theory (DFT), CoTiSb has been predicted to have a bandgap of approximately 0.9-1.0 eV with a lattice constant of 5.88 Å[75, 76], while NiTiSn has a reduced bandgap of 0.4-0.5 eV with a slightly larger lattice constant of 5.92 Å[72, 77]. The calculated energy band structures as well as the density of states (DOS) for NiTiSn and CoTiSb are shown in Figure 1.5. Both compounds show an indirect bandgap from the Γ point to X point with wide conduction bands and relatively low dispersion valence bands. In practice, however, the bandgaps measured of semiconducting half-Heusler compounds using electrical and thermoelectrical techniques are much smaller than those predicted by DFT with estimates as low as ~0.1 eV from electrical and optical measurements [78]. A bandgap of >0.13 eV was estimated from thermally activated behavior in MBE-prepared CoTiSb thin films [58]. Recent angle-resolved photoemission spectroscopy (ARPES) in conjunction with scanning tunneling microsopy (STM) suggest a true bandgap of >0.6 eV may be present [60]. In each of these experiments the inferred bandgap is sensitive to both the sample preparation as well as the measurement technique indicating the necessity of further study of the true bandgap in these compounds.

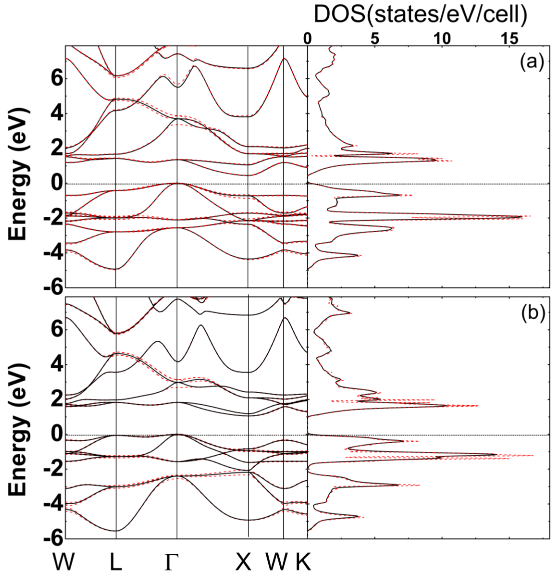

Figure 1.5. Calculated energy band structures and DOS of (a) NiTiSn and (b) CoTiSb compounds. The red-dashed and black-solid lines correspond to the calculations with and without spin-orbit coupling, respectively. The Fermi level is at 0 eV. Reprinted from [79] with permission from *AIP Publishing*.

1.3 Heterostructures

Despite the success of silicon in modern electronics, the possibility to create such a large number of new and diverse devices would not be possible without the use of heterostructures. The heterojunction, the basic building block of all heterostructures, is the interface occurring between two dissimilar, crystalline materials. In the case of traditional semiconductor electronics, the two materials are semiconducting with unequal and offset bandgaps. By understanding the band-alignments, complex device structures can be designed and grown, tailoring the shape of the energy bands to achieve properties which otherwise would be unattainable. Heterostructures are a fundamental component in the operation of many modern devices including lasers, bipolar transistors, and high electron mobility field-effect transistors (HEMTs).

The behavior of a heterojunction is dictated by the energy band alignment between the two materials. Semiconductor interfaces can be organized into three main types of heterojunctions depicted in Fig. 1.6 (a-c): type I (straddled gap), type II (staggered gap), and type III (broken gap). In the case of type I band alignment [Fig. 1.6 (a)], the bandgap of the smaller bandgap material lies completely within the larger bandgap material (e.g. AlGaAs and GaAs). For type II and III band alignments, the bandgaps are offset, with type II overlapping (e.g. InP and $In_{0.52}Al_{0.48}As$) and type III no overlap (e.g. InAs and GaSb) seen in Fig. 1.6 (b) and (c), respectively. However, when these two different materials are put in contact, their Fermi levels must align, which is accommodated by band bending near the heterojunction which is schematically shown in Fig. 1.6 (d-f) for (a-c), respectively in the case of n-type doping for each. Beyond bandgap engineering, many of the next generation of devices such as the proposed spin field-effect transistor (spin-FET) [80] and multiferroics [81], require the combination of materials with magnetic and semiconducting properties. Unfortunately, epitaxy of dissimilar materials brings about its own challenges arising from the differences in crystal structure (e.g. symmetry, surface energies, and strain) as well as chemical reactivity between the two compounds [82].

The ultimate draw of Heusler compounds is utilizing the multifunctional properties observed within the Heusler compounds to build a heterostructure with characteristics not achievable within conventional semiconductor physics. The similarities in crystal structure and vast diversity of electronic and magnetic properties within one class of materials makes Heusler based heterostructures an attractive direction for future devices. Here, not only the bandgap and band alignments but also the wide range of properties determined by Heusler composition dictate the resulting device characteristics. Because the crystal structure would be maintained, some of the challenges discussed above for the epitaxy of dissimilar materials would be lessened. While the perovskite crystal structure show a number of these properties as well, Heusler compounds offer the advantage of increased compatibility with existing III-V compounds due to their similarity in lattice constants and crystal structure as well as absence of oxygen. Despite the promise of Heusler-Heusler based heterostructures, experimental studies examining them are limited to only a few reports of sputtered NiMSn

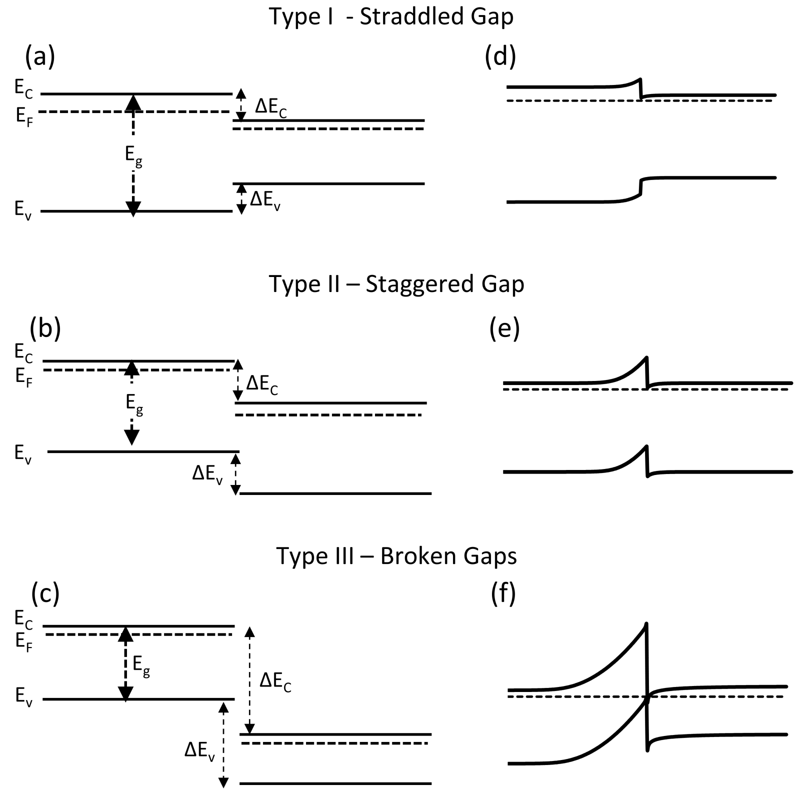

Figure 1.6. Energy band diagrams of two semiconductors taken seperately for (a) Type I - straddled gap (b) Type II - staggered gap, and (c) Type III - broken gap band alignments. (d-f) Energy band diagrams of the materials of (a-c), respectively connected.

(M=Ti,Zr,Hf) layers [83, 84].

1.4 Overview of this Work

This dissertation uses the semiconducting half-Heusler, CoTiSb, as a model system to develop a better understanding of Heusler compounds with the ultimate goal of developing Heusler-Heusler heterostructures. Here, MBE in conjunction with a number of *in-situ* and *ex-situ* characteristics techniques (described in Chapter 2) are utilized to develop this understanding. The growth and intrinsic properties of CoTiSb are presented in Chapter 3, which builds on the work of Jason Kawasaki [60]. The tunability of Heusler compound properties and Fermi level position by changing the electron count is explored for electron doping via nickel alloying (Chapter 4). The introduction of magnetism to this non-magnetic compound by means of iron alloying is explored as an alternative route to achieving a tunable half-metallic compound (Chapter 5). The interface properties of CoTiSb with III-Vs as well as another semiconducting half-Heusler, NiTiSn, are examined by measuring the valence-band offsets using X-ray photoemission spectroscopy and compared to that expected from DFT (Chapter 6). Finally, CoTiSb is incorporated into a number of Heusler/III-V and Heusler/Heusler heterostructures, including diodes and GMR multilayer devices, and the resulting properties are measured (Chapter 7).

Chapter 2

Methods: Materials Growth and Characterization

2.1 Molecular Beam Epitaxy

Molecular beam epitaxy (MBE) has been a key enabling technology for many of the most advance device applications where atomically abrupt interfaces and high crystal quality are a requirement. For heterostructures in particular, these abrupt interfaces are a key requirement for proper device operation. In its simplest form, MBE can be understood as crystallization by condensation or reaction of a vapor in ultra-high vacuum (UHV). Here, high purity elements are thermally evaporated from individual effusion cells (also known as Knudsen cells) onto a substrate within a UHV environment ($\leq 10^{-10}$ Torr). This UHV environment allows for the mean free paths of the impinging atomic or molecular species to be much larger than the chamber diameter, creating the "molecular beam" the technique is known for. The shutters above each effusion cell, either pneumatic or solenoid controlled, allow for the precise control of which elements are being deposited on the substrate at any given time. In addition, a main growth

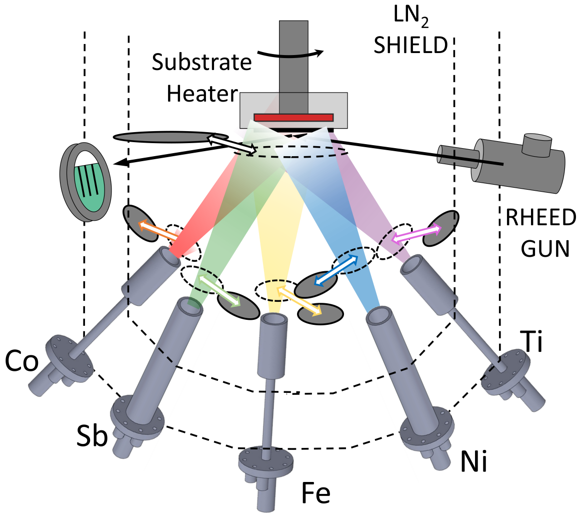

Figure 2.1. Schematic of an MBE growth chamber. Elemental sources are evaporated at a heated substrate, monitored with *in-situ* RHEED, and cooled with a LN_2 jacket.

substrate shutter can add even more control when flux transients are present.

A schematic of an MBE chamber such as that used to grow the Heusler films within this dissertation is shown in Fig. 2.1. In addition to being a UHV chamber with effusion cells, MBE chambers typically have *in-situ* monitoring capabilities of reflection high-energy electron diffraction (RHEED) which offers real time characterization of the film being grown, pyrometry and/or band-edge temperature monitoring, and flux measurement. In particular, the surface crystallinity and surface morphology can be inferred from the RHEED diffraction patterns. Within the MBE chamber, a liquid nitrogen (LN_2) cooled cryoshield is contained which serves two main purposes. First, it takes heat load due to the hot effusion cells, and secondly, serves to reduce the base pressure further. Samples are typically mounted using molten indium to metal blocks made of refractory metals (molybdenum for the present work). The blocks are then held in place by a manipulator that provides heat as well as rotation. The Heusler chamber was equipped with full 360° rotation while the III-V chamber was limited to only 120° rotation making continuous rotation impractical for the III-V layers. The consequences of this will be discussed in chapter 3.

During the MBE growth of high quality single crystals, it is critical that the compound stochiometry is accurate as deviations off stoichiometry degrade the electrical and magnetic properties of the grown film. For the MBE growth of traditional III-V compound semiconductors this is achieved using what is known as a growth window. Compounds such as GaAs are generally grown in a group V (e.g. As) rich condition, with the growth rate determined by the group III (e.g. Ga) flux [85]. Here, an elevated temperature is used to keep the impinging group V species from sticking to the substrate unless it can bond to a group III atom present. Because of the higher vapor pressure the excess group V atoms desorb from the surface. In certain conditions, a layer by layer growth mode will occur, and the growth rate can be determined by counting the RHEED intensity oscillations vs time, where one full oscillation corresponds to one monolayer of growth. This is schematically shown in 2.2. Such a growth window requires that the desired single crystal be a line compound, with a phase field where the line compound coexists with the excess element as is the case for GaAs with As.

Unfortunately, for most of the Heusler compounds such an ideal growth window does not exist. The transition metals present in Heusler compounds generally have significantly lower vapor pressures. In addition the base compounds are ternaries rather than binaries, implying up to three species fluxes (or more for alloyed Heusler compounds) must be carefully controlled rather than just two. Thus the elemental fluxes impinging on the substrate, as determined by the effusion cell temperatures, will largely determine the stoichiometry of the resulting film. This poses a significant challenge in the synthesis of Heusler compounds, but which can be overcome with careful control and calibrations as will be discussed in the subsequent section.

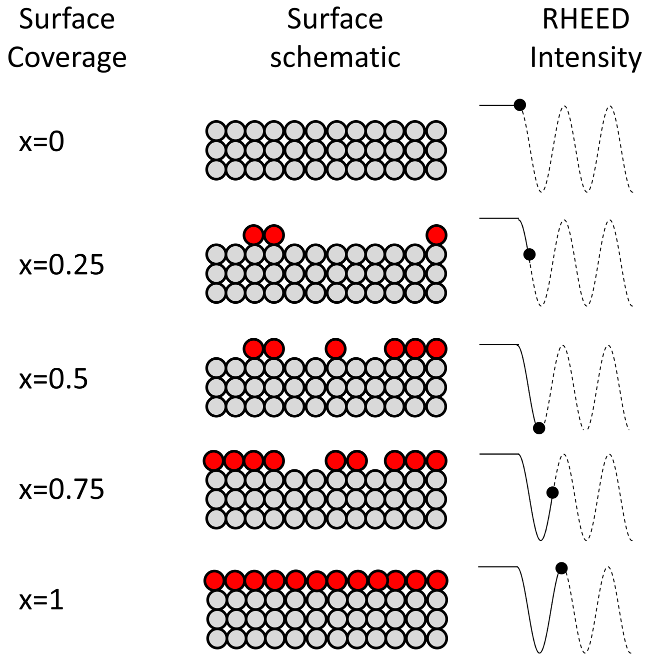

Figure 2.2. Schematic diagram of the surface morphology and resulting RHEED intensity during layer-by-layer growth mode. The intensity of a given spot or streak is maximized and minimized when a complete and half of a monolayer exists respectively.

2.1.1 Flux Control and Calibration

To calibrate the effusion cells atomic fluxes to be reproducible over many growths requires two parts: 1) careful measurement of the apparent flux and 2) determining the relationship between the apparent flux and the actual atomic flux. The apparent flux is determined using a beam flux monitor, which makes use of a ionization vacuum gauge that can be extended into the path of the atomic flux, and then removed during the actual growth. In Fig. 2.3(a) one such ionization gauges can be seen. Such a gauge consists of a filament, grid, and collector. A schematic of the control electronics circuit diagram is shown in Fig. 2.3(b). Current is passed through a biased filament which emits electrons, which are then accelerated towards the positively biased grid. The accelerated electrons collide with atoms/molecules present forming ionized species which are then measured as a current on the collector. The current measured is proportional to the pressure, or beam flux in this case. Although ionization gauge controllers are available commercially, to gain complete control over and ability to monitor the gauge, separate external electronics should be used. This allows the emission and filament current to be precisely set as well as monitored, enabling more reproducible measurements of the beam equivalent pressure (BEP) impinging on the gauge over time.

The measured BEP must then be related back to an actual atomic flux. To do so, calibration samples of varying growth rates, achieved by adjusting the effusion cell temperatures, are grown on silicon substrates. Here a low temperature (no substrate heat applied) growth is used to ensure the sticking coefficient of each element is as close to unity as possible. The areal atomic density for each of the elements present for each calibration sample is determined using Rutherford backscattering spectrometery (RBS). In the RBS experiment, a 2 MeV beam of He^{2+} ions are accelerated into the sample and the energy of the backscattered ions measured. An example spectra for an approximately 15 nm thick CoTiSb layer grown on Si is shown in Fig. 2.4(a). Here peaks in the spectra correspond to the atomic species and the area under each is proportional to the number of

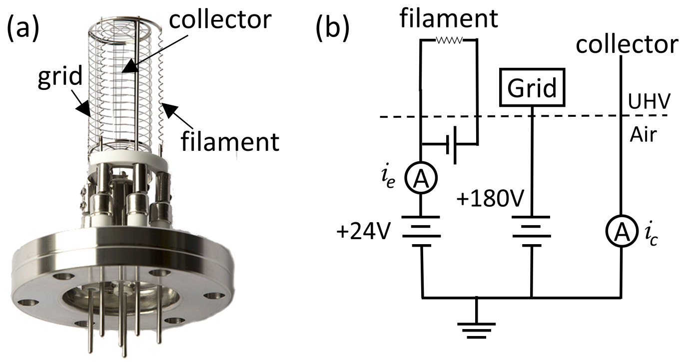

Figure 2.3. (a) Picture of an ion gauge similar to that used for flux measurements. (b) Schematic of the circuit diagram of the ionization gauge from (a) control electronics used for flux measurements. The filament current is controlled to maintain a constant emission current of ~6.5 μA. The filament and grid are biased +24 V and +180 V relative to ground respectively. The current measured by the collector is proportional to the flux incident on the gauge.

atoms present. In addition, depth information of the atoms can be determined from peak positions, where buried layers are pushed to lower energies. Overlaid is a simulated spectra, where the stoichiometry and layer thickness are used as adjustable parameters to match the raw spectra. The extracted atomic areal density can be related back to an atomic flux by dividing by the total time of deposition. Figure 2.4(b) shows a calibration curve obtained using three CoTiSb calibration samples measured with RBS at two (8° and 60°) sample tilts. Prior to each subsequent growth the effusion cell temperature is adjusted until the BEP measured matches the desired atomic flux. Using this procedure a stoichiometry better than 1.00±0.03:1.00±0.03:1.00±0.03 can be expected.

2.1.2 *In-situ* Growth and Characterization Facility

The majority of the work presented in this dissertation took place at the University of California - Santa Barbara within the Palmstøm lab interconnected UHV growth and characterization facility. The facility, shown in Fig. 2.5, contains four MBE growth chambers, two chemical beam epitaxy (CBE)

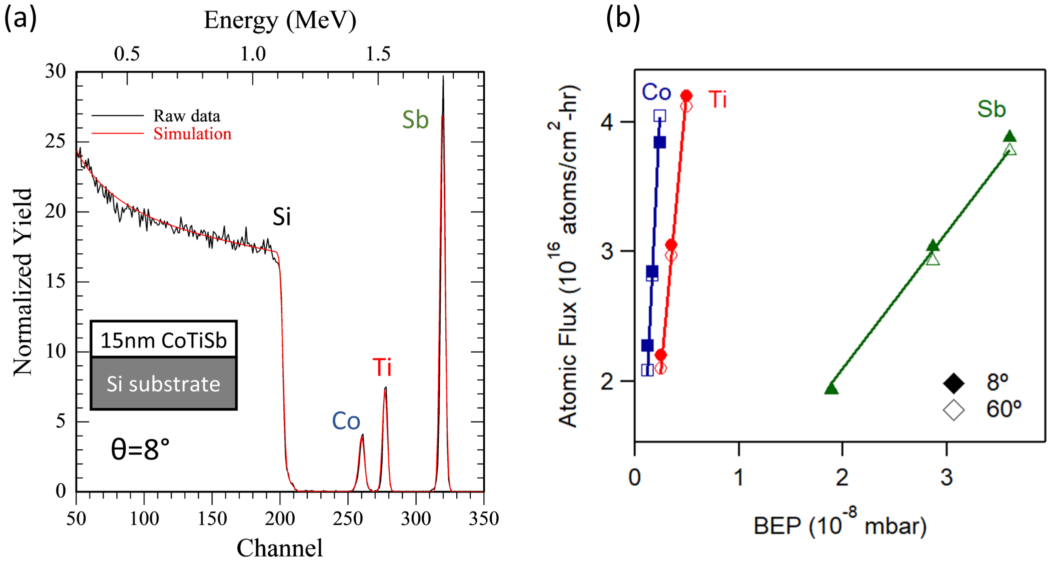

Figure 2.4. (a) RBS spectra for an approximately 15 nm thick CoTiSb film grown on a Si substrate overlaid with a simulated spectra for such a film. Here a 2 MeV beam and 8° tilt were used. (b) Atomic fluxes extracted from RBS spectra for three calibration samples grown with different growth rates plotted against BEP for Co, Ti, and Sb. Closed and open symbols correspond to 8° and 60° sample tilts respectively.

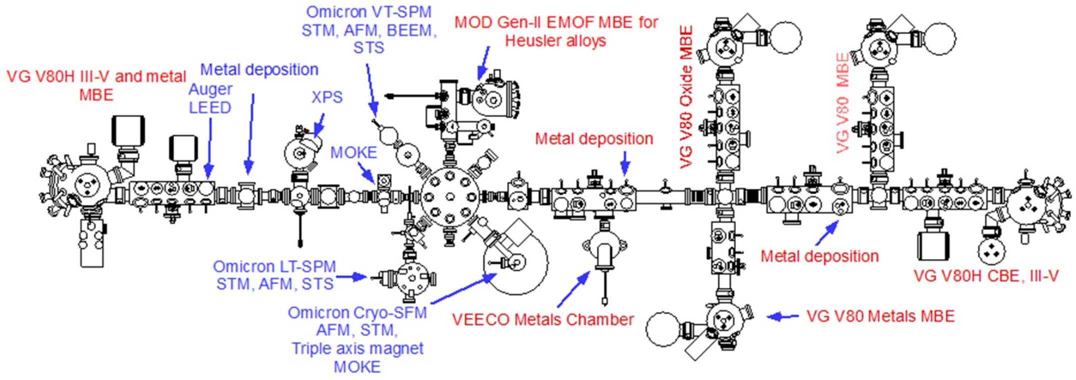

Figure 2.5. Layout of the Palmstrøm lab interconnected UHV growth and characterization facility. Growth and characterization capabilities are listed in red and blue respectively.

growth chambers, four additional growth systems, and extensive characterization tools all interconnected. Some of these tools include scanning-tunneling microscopes (STM), X-ray photoelectron spectroscopy (XPS), magneto-optic Kerr effect (MOKE), Low-energy electron diffraction (LEED), and Auger spectroscopy. This allows for the growth and subsequent characterization of films, all while maintaining a UHV environment, with a base pressure less than 5x10^{-10} Torr. This is especially important when examining surfaces and interfaces that would otherwise degrade if exposed to oxygen or other contaminants contained within the atmosphere.

For the purposes of this dissertation just two of the MBE growth chambers were utilized: one for the III-V layers, and one for the Heusler compounds. In addition, an e-beam deposition chamber containing AlO_x and MgO was used to deposit protective capping layers on the films to be removed to atmosphere as well as buffer layers for MgO substrates. Throughout this work a number of *in-situ* and *ex-situ* characterization techniques were utilized including *in-situ* characterization techniques of RHEED, photoemission spectroscopy (PES), and STM, and *ex-situ* characterization techniques of atomic force microscopy (AFM), X-ray diffraction (XRD), superconducting quantum interference device (SQUID) magnetometry, electrical transport, Seebeck, ellipsometry, and atom probe tomography (APT). The following sections provide an overview of PES, and some of the more specific cases of it in XPS and angle-resolved photoemission spectrscopy (ARPES) which are used throughout this dissertation.

2.2 Photoemission Spectroscopy

Photoemission spectroscopy (PES), which makes use of the photoelectric effect, is a useful surface-sensitive probe of chemical and electronic structure of materials. Figure 2.6 shows a schematic diagram of a PES experiment. Here a photon of energy $h\upsilon$, incident on the sample, is absorbed exciting an electron which is than emitted from the sample surface. The maximum kinetic energy of the electrons emitted is easily related back to the photon energy of the incident photon energy by the relation,

$$E_{KE}^{max} = h\upsilon - \Phi_0 \tag{2.1}$$

where E_{KE}^{max} is the kinetic energy of the photoelectrons, h is Planck's constant, υ is the frequency of the light, and Φ_0 is the work function. The energy distribution of the photoemitted electrons, rather than just the maximum kinetic energy, can be used to determine the electronic density of states (DOS) and chemical bonding. Here the binding energy of the original electron within the crystal, E_B, can be estimated as

$$E_B = h\upsilon - \Phi_0 - E_{KE} \tag{2.2}$$

which is sketched in Fig. 2.6. Here it is important to note that photoemsssion only probes occupied states up to the Fermi level. To study unoccupied states other techniques such as inverse photoemission must be used.

The core-level binding energies and photoemission cross-sections of most elements are tabulated [86, 87], making quantitative analysis of spectra possible. Although composition cannot be determined absolutely, an estimate that is ac-

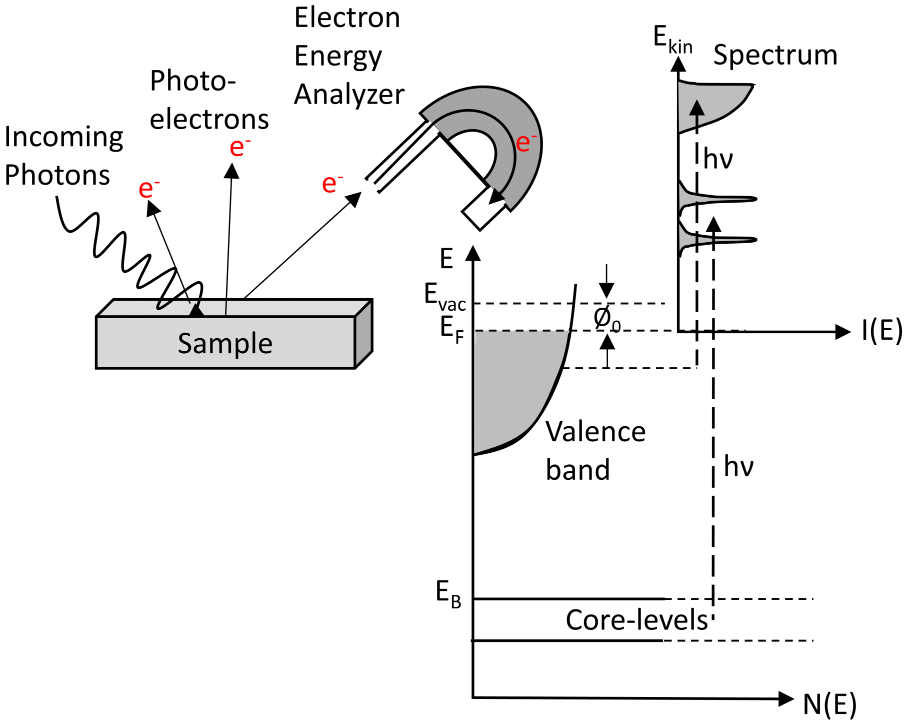

Figure 2.6. Schematic diagram of a PES experiment where a sample is irradiated with photons of energy hv, photoemitting electrons that are collected by a electron energy analyzer. The measured energy spectrum is directly related to the electronic density of states, and originates from both the valence band and core-levels.

curate to within a few percent can be made. In addition, the dependence of the binding energy position of a core-level allows for the determination of the chemical environment and valence state of the emitting atom, known as the chemical shift. This can be useful in in distinguishing between surface-like and bulk-like contributions, allowing the determination of which elements are involved in the surface reconstructions.

Many laboratory PES setups use X-ray sources such as Mg Kα ($h\upsilon$=1253.6 eV) and Al Kα ($h\upsilon$=1486.6 eV), and are then known as XPS. By using X-rays as the photon source, the sensitivity to the surface increases greatly. This can be understood by examining the "universal curve", shown in Fig. 2.7, where the inelastic mean free path of the emitted electrons is plotted against the electron kinetic energy. Here we can see electrons excited by X-rays will have kinetic energies in the range of 10-1000 eV, lying near the minimum of the curve. Consequently, only the first few monolayers of the surface will be probed by a traditional XPS measurement.

When higher resolution or alternative excitation energies are desired, alternative X-ray sources must be used. While some laser-based laboratory setups are able to provide variable wavelength sources, synchrotron facilities are able to provide the highest intensity broad-band X-rays. These high photon fluxes not only allow for much greater energy resolution, but also enable more complex experiments probing the momentum and spin texture (spin direction as a function of momentum) of the emitted electrons. In addition, synchrotron light often offers variable polarization, small photon spots, or the possibility of time-resolved measurements.

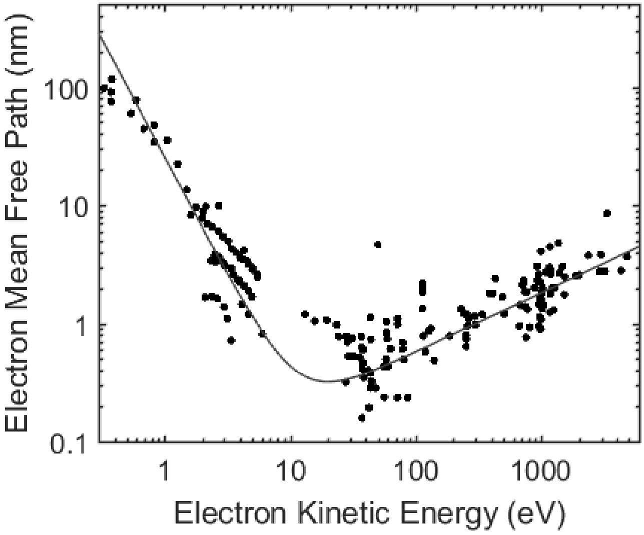

Figure 2.7. Electron inelastic mean free path for a variety of elements, giving the "universal curve". Adapted from [88] with permission from *John Wiley and Sons*.

2.2.1 Angle-Resolved Photoemission Spectroscopy

Angle-resolved photoemssion spectrocopy (ARPES) is powerful tool to visualize the electronic band structure of a material. In this experiment, not only are the energy of the photoemitted electrons measured, but also the momentum. This is achieved by using a two-dimensional detector array that simultaneously measures the binding energy and angular distribution of the emitted electrons. By sweeping photon energy or sample angle relative to the hemispherical analyzer out-of-plane or in-plane band structures can be probed respectively. The ARPES measurements performed in this disseration were performed at the i4 beamline of MAX-Lab synchrotron in Lund, Sweden.

A schematic diagram of a ARPES beamline is shown in Fig. 2.8. Here a flux of ~10^{19} photons/(sec-mm^2-mrad^2-0.1% bandwidth) are generated from an undulator located inside the synchrotron storage ring. The X-rays generated have a broad spectrum which is monochromated within the beamline by diffraction gratings and optics. The final monochromated beam is impinged on the sample with a spot size of ~100 μm. The photoemitted electrons are captured by a

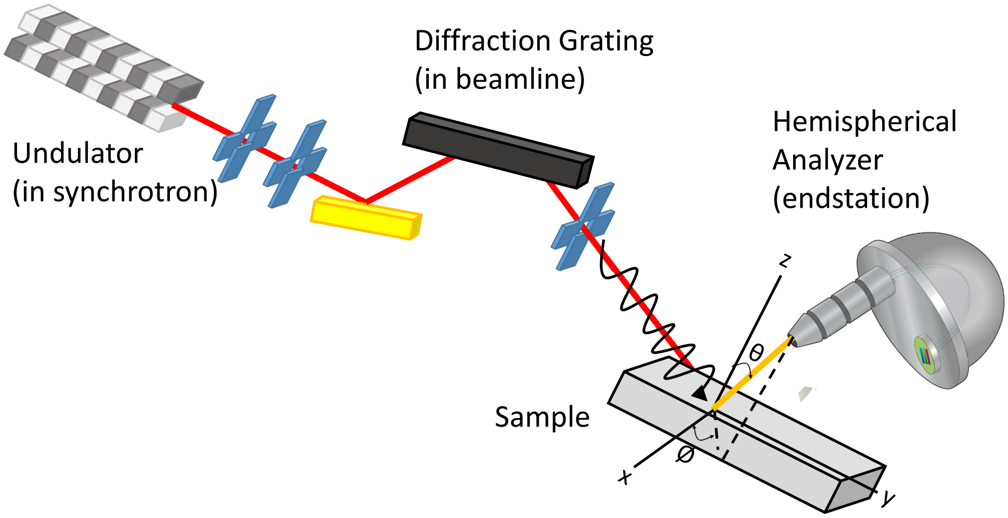

Figure 2.8. Schematic diagram of an angle-resolved photoemission spectroscopy beamline. The undulator, residing within the synchrotron storage ring, generates a broad band of X-rays. Within the beamline optics the beam is monochromated and beam shaped. The measurement of momentum and energy is performed within the endstation using a hemispherical analyzer.

hemispherical analyzer at a known angular position relative to the sample and photon energy allowing the initial electron crystal momentum to be determined.

Traditionally a simplified three-step model [89] is used when analyzing photoemission spectrum. First, an electron is optically excited from an initial state (E_i, k_i) to a final state (E_f, k_f) inside the solid. Second, this photoelectron then travels to the sample surface. Finally the photoelectron escapes into the vacuum to a free-electron like state (E_{kin}, k_{out}). Within this model, optical excitations are only allowed for specific transitions and polarizations, leading to measured photoemission intensity that depends not only on the DOS of the initial states, but also these allowed transitions. These transitions are typically referred to as matrix element effects [86]. Using this model, the final free-electron like state can be directly related back to the initial state of the electron within the crystal. Momentum within the plane of the sample is conserved across the interface leading to the relation:

$$E_{i,\parallel} = E_{f,\parallel} = E_{out,\parallel} = E_{out} sin\theta = \sqrt{\frac{2m_e E_{kin}}{\hbar 2}} sin\theta \tag{2.3}$$

where m_e is the electron mass, E_{kin} is the kinetic energy of the photoemitted electron, $\hbar$ is planks constant, and θ is the angle from normal emission [86]. However the out-of-plane momentum is not preserved. Instead, the electron must overcome a barrier, referred to as the "inner-potential", U_0. This is generally experimentally derived by fitting the periodicity of the band dispersion to the high symmetry points in the bulk brillioun zone. In this case, the initial crystal momentum of the electron can be approximated to be:

$$E_{i,\perp} = \sqrt{\frac{2m_e}{\hbar 2}(E_{kin} cos^2\theta + U_0)} \tag{2.4}$$

The inner potential approximation breaks down at lower photon energies where the final-state of the photoemitted electron is less free-electron like [86]. Experimentally, this is often simplified by measuring at normal emission ($k_x = k_y = 0$) such that $cos^2\theta$=1, and then sweeping the incident photon energy. For an (001) oriented surface of a face-centered cubic crystal this corresponds to traversing from bulk Γ to bulk X high symmetry points. Within this disertation all ARPES analysis was conducted using the Igor software with modified versions of code written by J. Osiecki for MAX-Lab beamline i4 in collaboration with J. Logan. The code can be found at [90]

ARPES measurements are typically conducted at photon energies between 10 and 150 eV. From Fig. 2.7 one can see that these measurements lie at the minima, making them extremely surface sensitive. Therefore to be able to measure thin films great care must be taken to prepare a clean well-ordered surface, free of oxidation. For the $\mathrm{Co}_{1-x}\mathrm{Ni}_x\mathrm{TiSb}$ films discussed in Chapter 4, an antimony capping scheme is developed which enables the transport of samples grown at UCSB to MAX-Lab for subsequent ARPES measurement.

2.2.2 XPS Band-Alignment Measurement

As discussed in chapter 1, heterojunctions form the fundamental building block for many modern devices. Here the abrupt change in bandgap as well as the valence and conduction band discontinuities $\Delta\mathrm{E}_v$ and $\Delta\mathrm{E}_c$ can be used to design the solid-state electronic devices. One method to determine the $\Delta\mathrm{E}_v$ between two materials utilizes XPS [91]. For heterojunctions with offsets much larger than the resolution of the electron detector, two distinct valence band edges are visible. By extrapolating these to obtain the two valence band maxima positions, one can obtain $\Delta\mathrm{E}_v$ from the difference [92]. However when the band offsets are smaller, a three step process is used to extract the valence band offset [91].

Figure 2.9 shows a schematic diagram of a heterojunction formed by two materials, A and B. Here it is assumed that the heterojunction is thin enough (~1-2 nm) that the band bending is negligible. In addition to the valence and conduction bands, an arbitrary core level in semiconductor A with binding energy E^A_{CL}, a core level in semiconductor B with binding energy E^B_{CL}, and their difference $\Delta\mathrm{E}_B(A-B) = E^A_{CL} - E^B_{CL}$ are shown. Thus by simple arithmetic it follows that

$$\Delta E_v(A-B) = \Delta E_B(A-B) + (E^B_{CL} - E^B_v) - (E^A_{CL} - E^A_v) \tag{2.5}$$

where $E^A_g \geq E^B_g$. The second two components, $(E^B_{CL} - E^B_v)$ and $(E^A_{CL} - E^A_v)$, are determined by measuring the XPS spectra of a bulk sample of each of the respective semiconductors, and accurately fitting the core-level and valence band maximum positions. Then by depositing a layer thin enough of material B on material A, such that corelevels from both materials are visible, the $\Delta E_B(A-B)$ can be determined. Because the mean free path of the escaping electrons is only ~1-2 nm, the overlayer must be approximately this thickness to collect electrons from both sides of the junction. This also assures that band bending is minimized. Here the final valence band offset precision is limited by the accuracy of the core-level and valence-band maximum fits, and is normally on the order

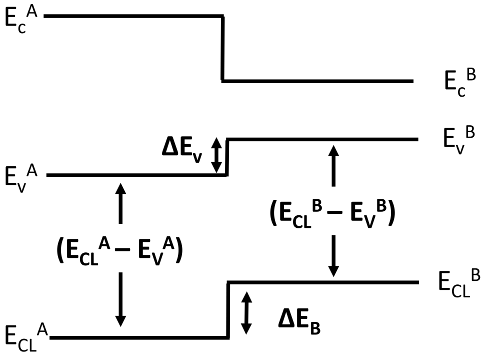

Figure 2.9. Schematic energy band diagram of a thin, abrupt heterojunction.

of 5-10 meV. This method has been successfully used to measure the valence band offsets in a number of material systems with error ≤ 0.07 eV using Al Kα radiation [93–98].

Chapter 3

Growth and optical properties of CoTiSb and CoTiSb based Heterostructures

This chapter builds upon prior work of Jason Kawasaki [60], detailing the growth of CoTiSb and related alloys. Here the III-V buffer layer growth and preparation used for all CoTiSb and related compounds are outlined as well as some of the intrinsic properties of pure CoTiSb discussed.

3.1 Growth of CoTiSb based compounds by MBE

3.1.1 III-V buffer preparation

One of the important considerations when growing a high quality film is the proper selection of substrate. Here lattice matching of the film with the substrate

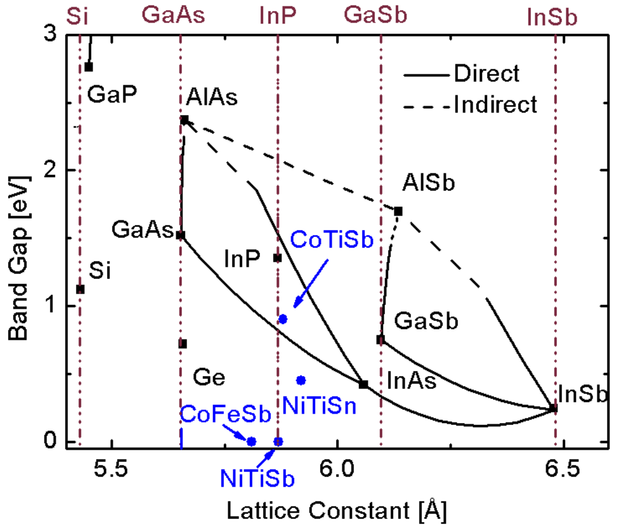

Figure 3.1. Bandgap energy versus lattice parameter plot for the semiconducting III-V compounds [101]. Also included are the half-Heusler compounds CoTiSb, NiTiSn, NiTiSb, and CoFeSb [7, 102].

is an important consideration to minimize the formation of dislocations. This can be achieved by either choosing a surface that has the same lattice constant or a coincident lattice. Beyond lattice parameter, choosing a substrate with the same crystal symmetry reduces the formation of defects such as stacking faults or anti-phase domains. For the half-Heusler CoTiSb, which has the F$\bar{4}$3m symmetry, the III-V compounds, which also have this symmetry, are a desirable choice of substrate. The MBE growth of III-V compounds is well-studied and relatively straight-forward to achieve high crystal quality layers. In addition, for the arsenic and antimony containing compounds, arsenic and antimony capping layers have been successfully demonstrated allowing the transport of III-V layers *ex situ* and, following reintroduction to ultra-high vacuum (UHV), the thermal desportion of the capping layer exposing the nearly as-grown surface for subsequent layers or analysis [99, 100].

Within the III-V compounds, InP(001) substrates are commercially available and nearly lattice matched to the semiconducting half-Heusler compounds CoTiSb and NiTiSn, shown in Fig. 3.1. In addition, the related half-Heusler compounds NiTiSb and CoFeSb are also closely lattice matched suggesting that alloying CoTiSb with either nickel on the cobalt site or iron on the titanium site should not introduce much strain. While growth directly on InP(001) substrates would be desirable, attempts to grow CoTiSb directly on chemical beam eptiaxy (CBE) prepared InP at growth temperatures of $T_{substrate}$ ~275°C - $T_{substrate}$ ~120°C resulted in dim, spotty RHEED with evidence of polycrystalline rings for the lowest growth temperatures attempted. Therefore different III-V buffer layers, $In_{0.52}Al_{0.48}As$ and $In_{0.53}Al_{0.47}As$ (referred to as InAlAs and InGaAs respectively), were used which have previously been shown to produced high quality CoTiSb [58].

InP (001) wafers were used for growth of both InAlAs and InGaAs. InP wafers were indium bonded to molybdenum blocks and loaded into the UHV system. Wafers were outgassed to ~300°C measured as 515°C by a thermocouple near the outgassing heater until the system pressure returned to base pressure. The wafers then were loaded into a VG V80H III-V MBE system where they were slowly heated under a large As_4 overpressure to desorb the native oxide. Because InP (001) wafers show no clear transition when the oxide fully desorbs, the wafer temperature was carefully monitored using both IR pyrometry and band edge temperature monitoring. Upon reaching ~510°C, the wafer was quickly heated to ~530°C to observe the 2x to 4x transition of InP indicating a metal rich surface. At the first indications of the transition, the sample was rapidly cooled to 480°C and the InAlAs or InGaAs layer begun once the temperature stabilized.

Fluxes for In, Al, and Ga were calibrated using growth rate RHEED intensity oscillations of InAs, AlAs, and GaAs respectively. The atomic flux was adjusted by changing the effusion cell temperature to match the desired growth rate and atomic flux ratio between In and Al or In and Ga. The desired ratio was verified by performing lattice matching calibrations, where the In flux was held constant and three fully relaxed layers (~500 nm thick) of varying Al or Ga content were grown. The lattice parameter extracted for each of the layers was then used to determine the In:Al or In:Ga ratio for each layer.

400 nm thick InAlAs and InGaAs buffer layers were grown at approximately 0.5 monolayers per second with a group V:III ratio of ∼25. Buffer layers were grown in the temperature range of 480°C to 500°C as determined by a pyrometer calibrated to the InP 2x to 4x transition. After buffer layer growth, samples were annealed under As_4 overpressure at growth temperature to form a well ordered arsenic terminated surface. InAlAs and InGaAs layers showed a (2x4)/c(2x8) and (nx3) surface terminations respectively shown in Fig. 3.2(a-b). For the doped InAlAs and InGaAs layers, Si and Be were used as n- and p-type dopants respectively. To minimize substrate preparation variations, 2 inch wafers were used which could then be arsenic capped and used for multiple subsequent CoTiSb growths. For buffer layers intended to be arsenic capped, following growth, the sample was cooled to $\leq$ 200°C whereupon the heat to the sample was turned off and sample was rotated to face the cryoshield to cool it further. Following $\geq$ 10 hours of radiative cooling, the sample was rotated back to growth position, and 45 minutes of As_4 was deposited to form the protective cap for subsequent *ex-situ* transfer. After the 2 inch wafer was unloaded from vacuum, it could then be cleaved into six to eight pieces for CoTiSb growth. While the intention of using the arsenic capped 2 inch wafers was to minimize variations of the buffer layers between different Heusler growths, a variation in the buffer lattice parameter was observed. This is due to the geometry of the MBE chamber where the effusion cells are each at an angle towards the substrate and thus small variations in the flux are expected across a wafer. Traditionally this is mitigated by continuously rotating the sample during growth. However, as previously mentioned the III-V chamber only allows for ∼120° of rotation. Thus compositional variations across the 2 inch wafer were unavoidable. All buffer layers grown for X-ray photoemission studies of the band alignment as well as growth of any heterostructure containing NiTiSn were transferred *in situ* through transfer chambers with base pressures $\leq 5 \text{ x } 10^{-10}$ Torr.

Prior to Heusler growth, the cleaved arsenic capped buffer layers were remounted on molybedunum blocks and reloaded into the UHV system near the metals MBE reactor. Samples were outgassed to a maximum of 200°C prior to

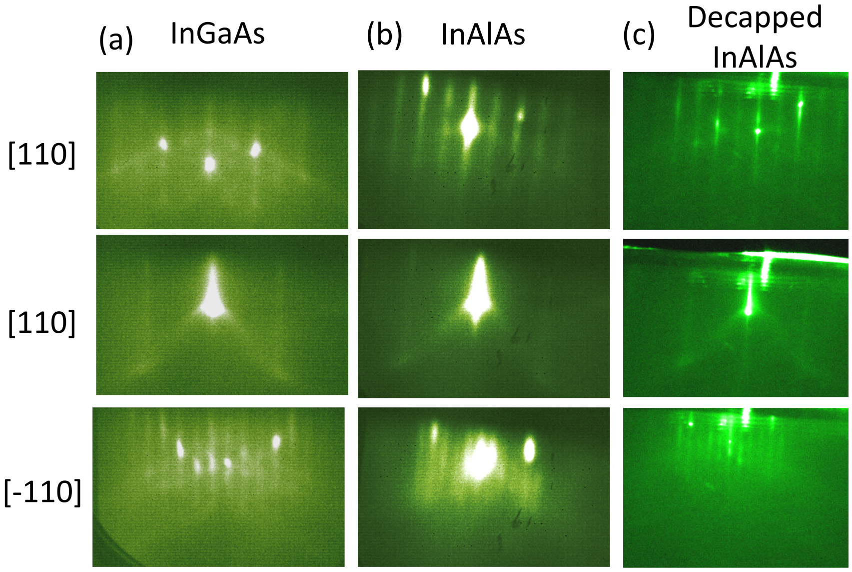

Figure 3.2. RHEED patterns for 400 nm thick (a) InGaAs, (b) InAlAs, and (c) arsenic decapped InAlAs.

loading into the MBE growth chamber to preserve the arsenic cap. Once in the MBE chamber the sample was slowly heated to thermally desorb the arsenic cap while monitoring the surface with RHEED. Due to the thermal lag between the block and the thermocouple mounted behind the substrate heater, the final desorption step (thermocouple reading ≥400°C) was done at a maximum of 2°C/min. As the cap desorbed a pressure spike could be observed in the chamber pressure reading. The underlying buffer layer RHEED pattern, shown in Fig. 3.2(c), becoming bright and streaky signified successful cap removal. The sample was left at the arsenic desportion temperature for 10 minutes to allow any residual arsenic on the surface to desorb. Successful cap removal should leave a smooth surface with minimal surface roughening. An atomic force microscope image of an arsenic decapped InGaAs surface is shown in Fig. 3.3(a) where half unit cell steps of 2.9 Å are visible (Fig. 3.3(b)). For most molybedenum blocks used in this dissertation, the arsenic cap was found to desorb between 420°C and 430°C as measured by the thermocouple which corresponds to 350°C as determined by the arsenic desorption temperature on GaAs [99].

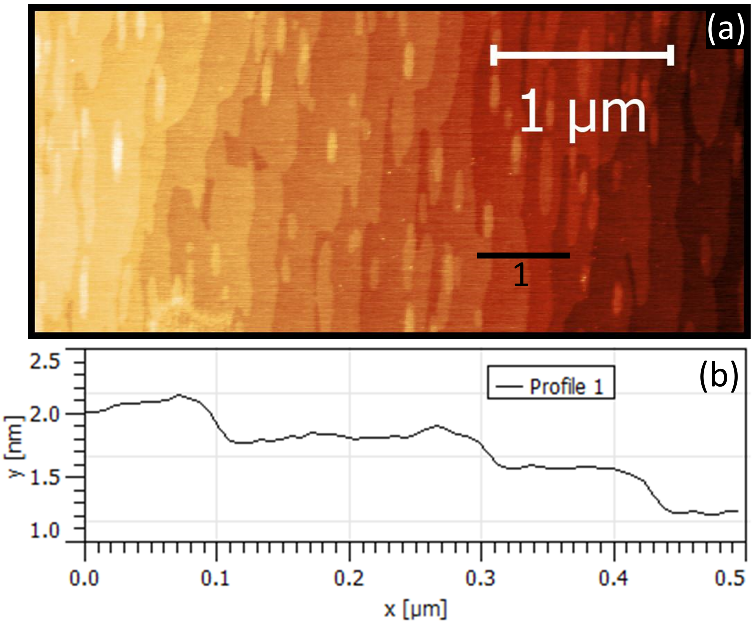

Figure 3.3. (a) Atomic force microscope image of a 400 nm thick arsenic decapped InGaAs surface showing smooth stepped surface. (b) Line cut from (a) showing 2.9 Å steps corresponding to half a unit cell of InGaAs.

3.1.2 MBE Growth of CoTiSb

As described previously, MBE growth of CoTiSb utilizes elemental sources calibrated using a flux ionization gauge and Rutheford backscattering spectrometry. Prior to growth the effusion cell temperatures were adjusted until the flux gauge reading matched the desired flux. CoTiSb was grown by simultaneous deposition from the elemental cobalt, titanium, and antimony effusion cell sources. Although growing with an antimony overpressure has been demonstrated for PtLuSb half-Heusler thin films [57], only limited experiments have suggested this growth window may also exist for CoTiSb. Therefore unless otherwise specified, stoichiometric 1:1:1 fluxes were used for growth of CoTiSb. Flux stoichiometries are calibrated to within 3% through RBS calibrations, deviations of over 2-3% are often visible in RHEED diffraction patterns. To minimize interfacial reactions of the transition metals with the buffer layer, a low temperature seed layer of CoTiSb was first grown at 200°C - 300°C [58]. Because surface diffusion is significantly higher than bulk diffusion, this lower temperature layer allowed complete coverage of the buffer layer prior to heating of the sample for higher temperature growth. A 3-4 nm seed layer was found to be sufficient to achieve complete coverage, therefore minimizing reactions. During the nucleation phase of growth a spotty RHEED pattern could be observed which became streaky over the first few nanometers of growth. After 5 nm of growth a bright streaky (2x1) surface reconstruction can be observed, shown in Figs. 3.4(a-c). During growth RHEED intensity oscillations of the specular spot can be observed as shown in Fig. 3.4(d) indicating a layer by layer growth mode. Each oscillation corresponds to one atomic bilayer of growth, and the period of 68 seconds gives a growth rate of 15 nm/hr in good agreement with the growth rate expected from RBS calibrations. Fig. 3.4(e) shows an XRD pattern for a $2\theta - \omega$ scan centered on the (002) reflection. Here the CoTiSb, InAlAs buffer layer, and substrate InP (002) peaks can be seen nearly overlaid indicating a good lattice match. In addition, finite thickness fringes can be observed centered around the CoTiSb peak giving a film thickness in good agreement with that expected from RBS calibrations and RHEED intensity oscillations.

Prior to removal from UHV, all films were capped with a protective capping layer to prevent oxidation. For most samples intended for structural, surface, magnetic, and magnetotransport characterization a 5-10 nm AlO_x cap was *in-situ* deposited using an electron beam evaporation of Al_2O_3 source at room temperature. For samples intended for vertical transport a 5 nm thick titanium layer was deposited at ~50-100°C from the effusion cell within the metals MBE. The titanium at the surface forms a conducting TiO_x layer when exposed to air allowing for good electrical contact to the devices. For samples intended to tranport *ex situ* to be reloaded into UHV, a ~100 nm thick Sb capping layer was deposited at 200°C in the metals MBE. For atom probe tomography samples a 5 nm thick nickel layer was deposited at room temperature.

Previous work by Kawasaki et al. [58] demonstrated MBE prepared CoTiSb films on InAlAs buffer layers show semiconducting behavior with favorable trans-

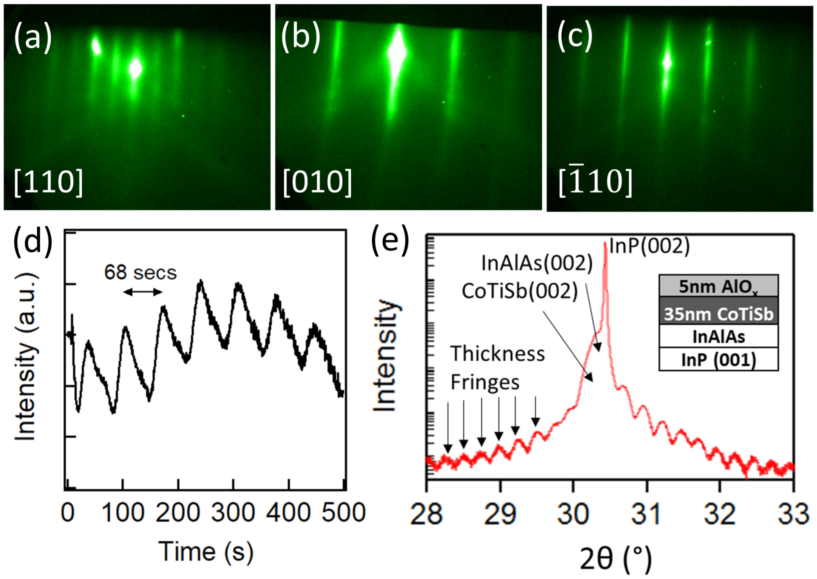

Figure 3.4. (a-c) RHEED diffraction patterns for CoTiSb after growth along the (a) [110], (b) [010], and (c) [-110] crystallographic azimuths. (d) RHEED intensity oscillations of the specular spot during growth. (e) XRD diffraction pattern of the (002) reflection.

port properties when compared to other half-Heusler compounds summarized in Fig. 3.5. Temperature dependent resistivity shows thermally activated behavior with an activation energy ≥13 meV. Electron dominated transport was observed with a carrier density that smoothly decreased with decreasing temperature. A transition in the magnetoresistance (MR), defined as

$$MR = \frac{R_{xx}(B) - R_{xx}(0)}{R_{xx}(0)} \tag{3.1}$$

from positive nearly quadratic at higher temperatures to negative with a zero-field peak at low temperatures was observed. This zero-field peak seen at low temperatures is consistent with localization [103] suggesting at low temperatures the transport is governed by a hopping mechanism rather than activation across the bandgap. Comparing MBE prepared CoTiSb room temperature transport properties, namely the mobility and carrier density, against other reported values in the literature one can see that CoTiSb has relatively high mobilities and simultaneously low carrier densities when compared to other half-Heuslers with a finite bandgap shown in Fig. 3.5(e). These favorable transport properties position MBE prepared CoTiSb as an attractive avenue to explore the intrinsic properties of CoTiSb and related alloys.

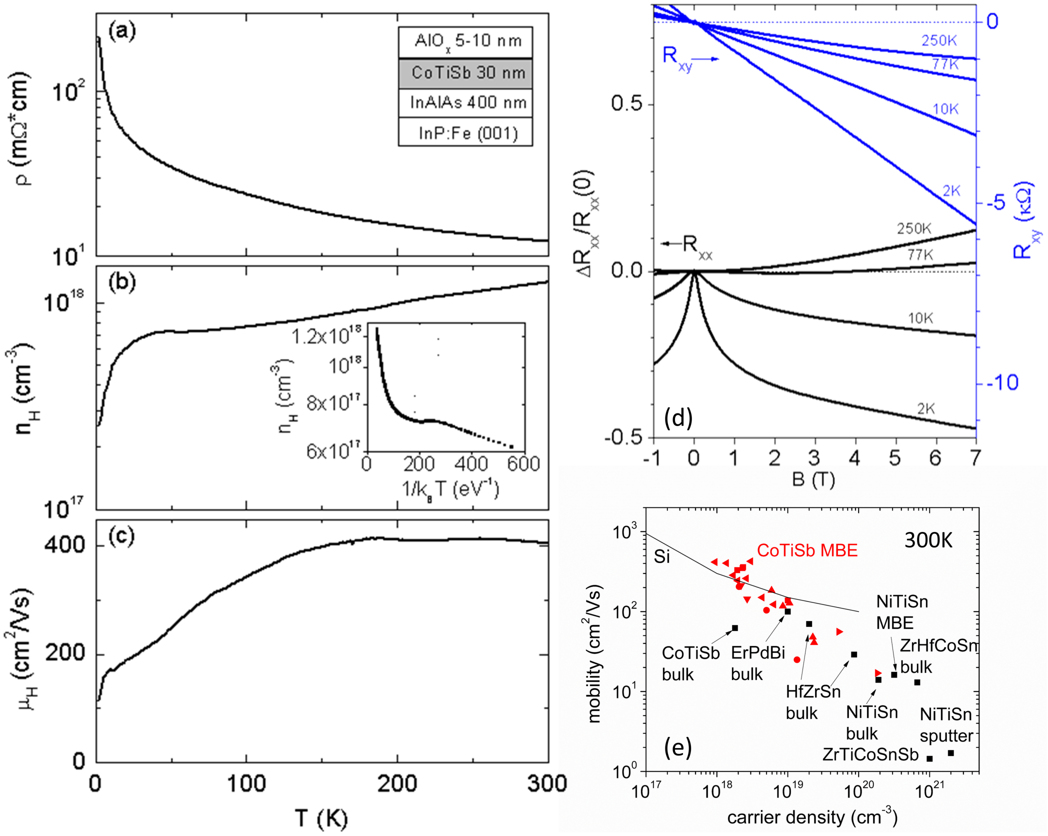

Figure 3.5. Electrical transport properties of a 30 nm thick MBE grown CoTiSb on InAlAs buffer layers. (a) Resistivity versus temperature at zero applied field. (b) Extracted 3D carrier density as a function of temperature extracted from R_{xy} at B = ±1 T. The inset shows the density replotted in logarithmic scale versus $1/k_BT$. (c) Calculated mobility assuming a single carrier model. (d) B-field dependence of the magnetoresistance, $\Delta R_{xx}/R_{xx}(0)$, and Hall resistance, $R_{xy}(k\Omega)$, for a selection of temperatures. (e) Room temperature mobility and carrier density of MBE grown CoTiSb (filled-red squares) compared to other half-Heusler compounds in literature. Adapted from [58] with permission from *AIP Publishing LLC*.

3.2 Optical properties of CoTiSb based compounds

The indirect bandgap predicted by generalized gradient approximation (GGA) DFT calculations is ∼1 eV [76], although most experimental observations have indicated the experimentally measured effective bandgap may be smaller due to defects and in-gap states. In an effort to determine the bandgap energy of CoTiSb the optical properties have been characterized using fourier transform infrared spectroscopy (FTIR)[1] and spectroscopic ellipsometry. Ellipsometric measurements were performed in air using a Woollam M2000DI Variable Angle Spectroscopic Ellipsometer from 0.73 eV to 6.49 eV at 3 incident angles, 55°, 65°, and 75°. Fitting was performed using the CompletEASE software using a multi-layer simulation. The ϵ spectra were constructed by the B-spline formulation [104]. In this formulation, a spline function is a series of polynomial segments, which is constructed in a manner to maintain continuity up to a certain degree of differentiation. B-splines are a basis set for polynomial splines. This set of basis functions can describe optical structures in the ϵ_2 spectrum, and the ϵ_1 spectrum is calculated at the same time through the Kramers-Kronig transform. An example of the spectroscopic ellipsometry data Ψ and Δ, and their best fit curves for a CoTiSb film on MgO are shown in Fig. 3.6 as solid and dashed lines, respectively. While the highest CoTiSb film qualities were obtained on InAlAs/InP(001) layers, these layers add complexity to the extraction of CoTiSb specific optical properties. Therefore, for optical measurements CoTiSb layers were grown both on MgO buffered MgO(001) and InAlAs/InP(001). Transmittance measurements were also performed at normal-incidence configuration, whose results were combined with ellipsometric data in the modeling procedures for the CoTiSb/MgO heterostructure to improve the accuracy of analysis.

In Fig. 3.7 the transmission of a CoTiSb film grown on an MgO (001) sub-

---

[1] Courtesy of Prasad Iyer

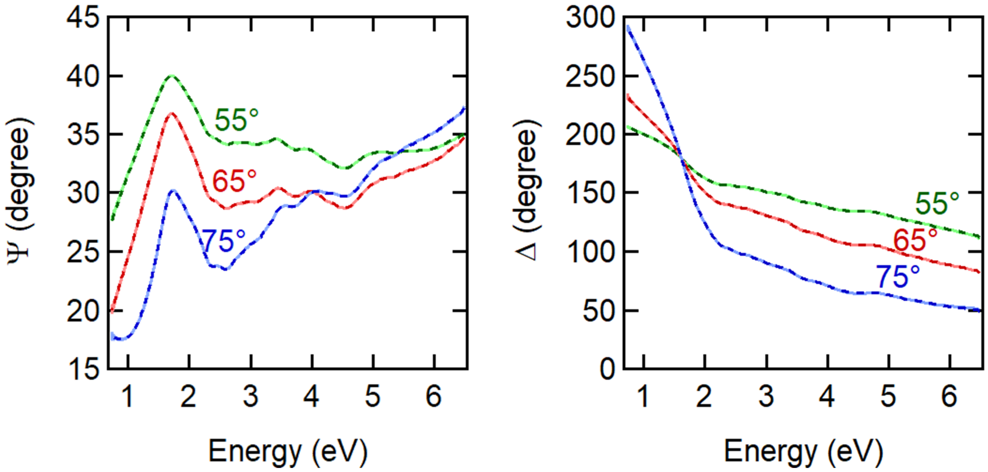

Figure 3.6. Data (solid light colored lines) and the best-fit curves (dashed dark colored lines) for Ψ and Δ of CoTiSb on MgO (001). Data were taken at incident angles of 55°, 65°, and 75°.

strate as well as the bare substrate is shown. A subtraction of the two curves gives the absorption due to the CoTiSb layer. Here we can see absorption that slowly increases from 0.15 eV to 0.75 eV. No clear band-edge feature is visible within these wavelengths. The observed absorption is likely due to in-gap states, consistent with the background intensity seen in angle-resolved photoemission spectroscopy measurements in the bandgap region [60]. The near zero transmission observed below 0.15 eV is due to the phonon excitation in the MgO substrate.

The calculated band structure, courtesy of Abhishek Sharan at the University of Delaware, using DFT within the PBEsol approximation [105]for CoTiSb is presented in Fig. 3.8(a). Figure 3.8(b) shows the calculated real ϵ_r and imaginary ϵ_i components of the complex dielectric functions for CoTiSb from DFT. Here a number of above-bandgap optical structures associated with interband critical points (CPs) [106] can be observed, which have been labeled A, B, C, and D. The largest feature, A, arises from the direct gap at Γ-point of the 1st brillouin zone. In Fig. 3.9(a) the ellipsometrically determined real ϵ_r and imaginary

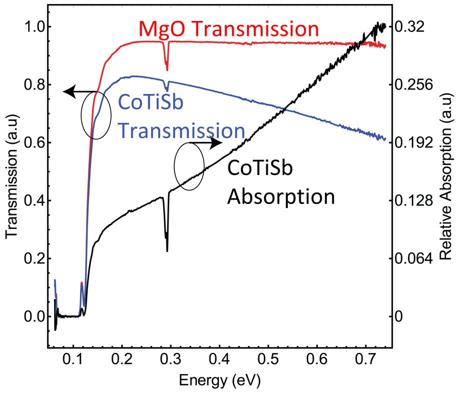

Figure 3.7. Fourier transform infrared spectrscopy (FTIR) of a CoTiSb thin film grown on MgO (001) substrate showing the transmission and absorption in the infrared region. The MgO substrate without the CoTiSb layer is also shown and was subtracted out to obtain the absorption spectra. FTIR measurements courtesy of Prasad Iyer at UCSB

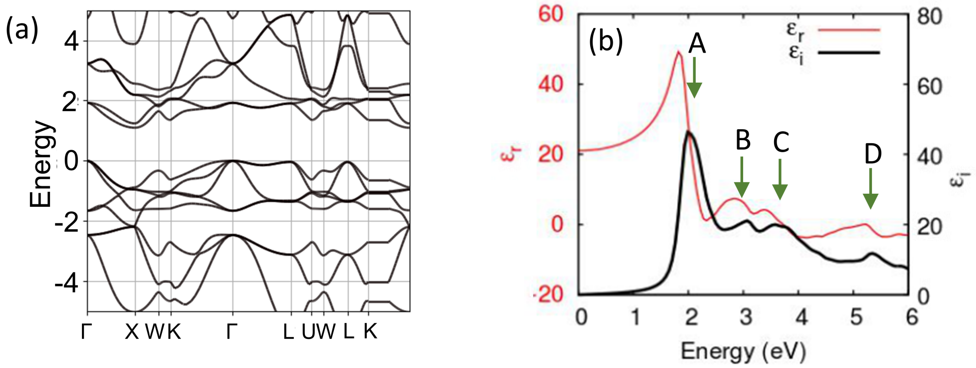

Figure 3.8. DFT within the PBEsol approximation calculated (a) bandstructure and (b) real ϵ_r and imaginary ϵ_i components of the permittivity for CoTiSb. Calculations courtesy of Abhishek Sharan at the University of Delaware.

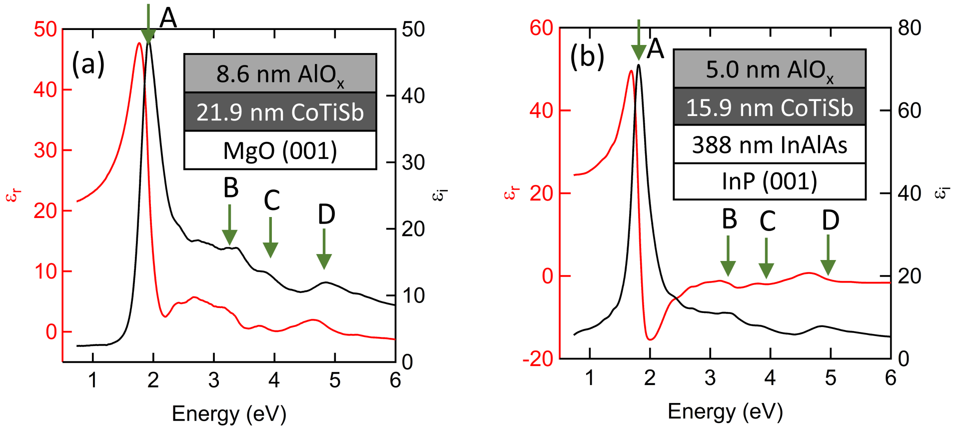

Figure 3.9. Spectroscopic ellipsometrically determined real ϵ_r and imaginary ϵ_i components of the dielectric function for a CoTiSb layer grown on a (a) MgO (001) substrate and (b) InAlAs buffer layer on InP (001) substrate.

ϵ_i components of the dielectric function for a CoTiSb layer grown on an MgO (001) substrate are shown. The fit layer thicknesses for AlO$_x$ and CoTiSb are 8.6 nm and 21.9 nm, respectively with a roughness of 1.3 nm. These film thicknesses are in good agreement with that expected from crystal quartz monitoring and RBS calibrations, respectively. The dominant feature (labeled A) of the spectra is a strong absorption peak at 1.80 eV, in agreement with previous experimental and theoretical (using GGA approximation) reports on bulk CoTiSb [76] which has been attributed to the direct gap at Γ. Notably, the absorption peak observed in experiment is at a slightly lower energy than that calculated using the PBEsol approximation suggesting the PBEsol approximation may overestimate the direct bandgap of CoTiSb. For energies below 1.8 eV, the optical absorption quickly drops to near zero, although a clear offset can be observed consistent with in-gap states being present. Notably, no additional band features can be observed corresponding to a 1 eV indirect bandgap. Additional features (labeled B, C, and D) can be observed in the spectra which correspond well to those expected from DFT, although again at slightly different energies.

To extract the dielectric function from a CoTiSb layer on an InAlAs/InP(001) heterojunction, shown in Fig. 3.9(b), 3 separate measurements were performed. One with just an InP (001) substrate with a 5 nm AlO$_x$ cap, one with a AlO$_x$

capped 400 nm thick InAlAs layer on InP (001), and finally the entire heterostructure including a 15 nm thick CoTiSb layer. Then by modeling each of the layers with a B-spline function as described previously, the contribution from CoTiSb could be extracted. Layer thicknesses for AlO_x, CoTiSb, and InAlAs from the fit are 5.0 nm, 15.9 nm, and 388 nm, respectively with a surface roughness of 0.9 nm. These layer thicknesses are in good agreement with those expected. In the ellipsometrically deterimined dielectric function, the features are similar to that measured on MgO, again with the same structures visible (labeled A, B, C, and D) as those observed in CoTiSb on MgO, and those expected from DFT. While the optical properties from CoTiSb grown on InAlAs would be expected to be sharper, the challenges introduced by the fitting procedure likely make the spectra from CoTiSb/MgO more reliable.

Chapter 4

Electronic Structure of electron doped $Co_{1-x}Ni_xTiSb$

As discussed in chapter 1, one of the attractive properties of Heusler compounds is that they can be alloyed in a similar manner to compound semiconductors leading to controllable tuning of these electronic and magnetic properties. Using this technique, promising values of ZT have already been shown for half-Heusler based thermoelectrics [24] as well as Fermi level tuning in full-Heusler magnetic tunnel junctions where room temperature tunneling magnetoresistance of greater than 100% has been reported [49–51]. Previously, the electronic structure of CoTiSb was investigated using angle-resolved photoemission spectroscopy (ARPES) and scanning tunnelling spectroscopy (STS), where good agreement was found with the density functional theory (DFT) calculated and the experimentally determined band structure [60]. However systematic experimental studies of how the electronic structure evolves as a function of alloying are lacking.

In these studies, we use the semiconducting half-Heusler, CoTiSb, as a model system to investigate the tunability of electronic properties through alloying. CoTiSb has 18 valence electrons per formula unit, making it a semiconductor with approximately a ∼1-1.5 eV bandgap [61, 107]. In contrast, NiTiSb, which has one more valence electron per formula unit, displays metallic, paramagnetic behaviour with the Fermi level well into the conduction band. By substitutionally alloying nickel on the cobalt site, the electronic band structure should be tunable. Previous efforts have used bulk crystals with density functional calculations to understand this semiconductor to metal transition [108–110]. High defect densities were observed which required the introduction of an impurity band to understand the resistivity data. In addition, no experimental method to directly probe the density of states was performed. Therefore further study to understand the effects are needed. In this experiment, we use high quality MBE prepared epitaxial thin films with electrical and ARPES measurements to examine the evolution of the electronic structure as a function of nickel alloying.

For this study, $Co_{1-x}Ni_xTiSb$ samples were grown in the Heusler VG V80 MBE system on nearly lattice-matched $In_{0.52}Al_{0.48}As$ (referred to as InAlAs) buffers epitaxial grown on InP (001) substrates using the buffer preparation procedures outlined in chapter 3. For electrical transport measurements an unintentionally doped 400 nm thick InAlAs buffer layer grown on semi insulating InP:Fe (001) substrates was used. For ARPES and STM measurements, the InAlAs layer was n-type doped with approximately 10^{18} Si atoms/cm^3 and was grown on sulfur doped InP (001) yielding an n-type, conductive buffer structure. InAlAs layers were grown in a conventional III-V MBE system. Samples were then arsenic capped and transferred through air into the dedicated Heusler MBE system for subsequent growth of $Co_{1-x}Ni_xTiSb$. After the samples were reintroduced to UHV, the arsenic cap was desorbed to reveal the arsenic-terminated (2x4)/c(2x8) InAlAs surface. $Co_{1-x}Ni_xTiSb$ was grown by simultaneous evaporation of cobalt, nickel, titanium, and antimony using stoichiometric fluxes. with a total flux of 9x10^{16} atoms/cm^2 hr, giving an approximate growth rate of 2.5 Å/min. 24 nm thick and $Co_{1-x}Ni_xTiSb$ samples were grown for structural and transport measurements. 15-20 nm thick $Co_{1-x}Ni_xTiSb$ samples were grown for ARPES measurements. Samples were grown at temperatures in the range 250-380°C . For samples with $x \geq 0.5$ nickel alloying, a thin 1 nm CoTiSb interlayer was used to minimize film reactions with the underlying III-V buffer layer, as nickel has been previously shown to be reactive with GaAs [111, 112].

Growth was monitored *in situ* using reflection high energy electron diffraction (RHEED). Films were nucleated using a thin, low temperature (250°C), seed layer, to minimize interfacial reactions. After seeding, the films were annealed and growth resumed at temperatures up to 380°C . For growth temperatures above 380°C additional spots could be observed forming on the RHEED streaks indicative of roughening, additional phase formation, or interfacial reactions. The crystal structure and electrical properties were analyzed *ex situ* using X-ray diffraction (XRD), electrical transport, and Seebeck measurements. For electrical transport and Seebeck measurement samples, an approximately 5-10 nm e-beam deposited AlO_x cap was used as a protective layer to prevent oxidation of the film. The electrical resistivity of the $\mathrm{Co}_{1-x}\mathrm{Ni}_x\mathrm{TiSb}$ series was measured between 20 and 300 K using a standard dc technique in a van der Pauw geometry by indium bonding gold wires to the samples. Seebeck coefficients of the series were measured at room temperature using indium soldered electrical contacts and thermal paste for the thermal probes. All measured $\mathrm{Co}_{1-x}\mathrm{Ni}_x\mathrm{TiSb}$ films were 24 nm thick.

ARPES measurements of $\mathrm{Co}_{1-x}\mathrm{Ni}_x\mathrm{TiSb}$ films were performed at beamline I4 of MAX III, part of MAX-LAB in Lund, Sweden using an Specs PHOIBOS 100 hemispherical electron analyzer. Base pressure of the analysis chamber was approximately 1 x 10^{-10} torr. All ARPES data was taken at <100 K to reduce the effects of thermal broadening. Binding energies are referenced to the Fermi level as determined by fitting the spectra Fermi edge, in good agreement with the measured position with respect to a tantalum foil in contact with the sample. Samples were transported *ex situ* using a thin protective antimony capping layer that was thermally desorbed once returned to UHV. Successful cap removal at MAX-Lab was confirmed by low-energy electron diffraction (LEED) and measurements of shallow core levels in photoemission. XPS spectra were fitted using a convolution of asymmetric Gaussian and Lorentzian line shapes with a linear background using the CasaXPS 2.3.16 program. The energy splitting between antimony $4d^{5/2}$ and antimony $4d^{3/2}$ was constrained to 1.24 eV for all fits.

4.1 Surface, Structural, and Electrical Characterization

During growth, a (2x1) surface reconstruction is observed in RHEED for $x \leq 0.5$ shown in Fig. 4.1(a-f), similar to that observed in pure CoTiSb. For higher levels of nickel alloying, other reconstructions including a (2x2) and disordered (3x2) (Fig. 4.1g-i) are observed. These variations from the (2x1) are likely a result of the difference in the number of dangling bonds at the surface due to the additional electron per nickel atom. A transition from a (2x1) to (3x3) surface reconstruction was observed for NiMnSb and was attributed to a transition from Mn/Sb terminated surface to a Ni terminated surface [55]. This suggests that as Ni content is increased within the alloyed series the surface termination may transition. The implications of this will be further discussed later in the chapter.

Figure 4.2(a) shows an XRD 2θ-ω scan for 24 nm thick $Co_{1-x}Ni_xTiSb$ films grown on InAlAs/InP(001) for x=0.025, x=0.1, and x=0.5. The sharp peaks at ω=30.44°and 63.34°correspond to the InP (002) and (004) substrate reflections, respectively, and the $Co_{0.5}Ni_{0.5}TiSb$ and InAlAs (002) and (004) peaks are nearly over-laid on the InP peaks indicating the close lattice match. Other than the $(00l)$ peaks and thickness fringes, no additional peaks in the XRD scans are observed. Figure 4.2b shows a scan centered around the (004) reflection. Here, finite thickness fringes can be clearly resolved corresponding to a thickness of 23.3, 24.8, and 23.6 nm for x=0.025, 0.1, and 0.5 respectively, in good agreement with the film thickness expected from the RBS. These fringes indicate a high quality interface between the $Co_{1-x}Ni_xTiSb$ films and InAlAs. The additional large peak observed in each scan corresponds to the InAlAs buffer layer. Small compositional deviations from the lattice matched $In_{0.52}Al_{0.48}As$ led to the

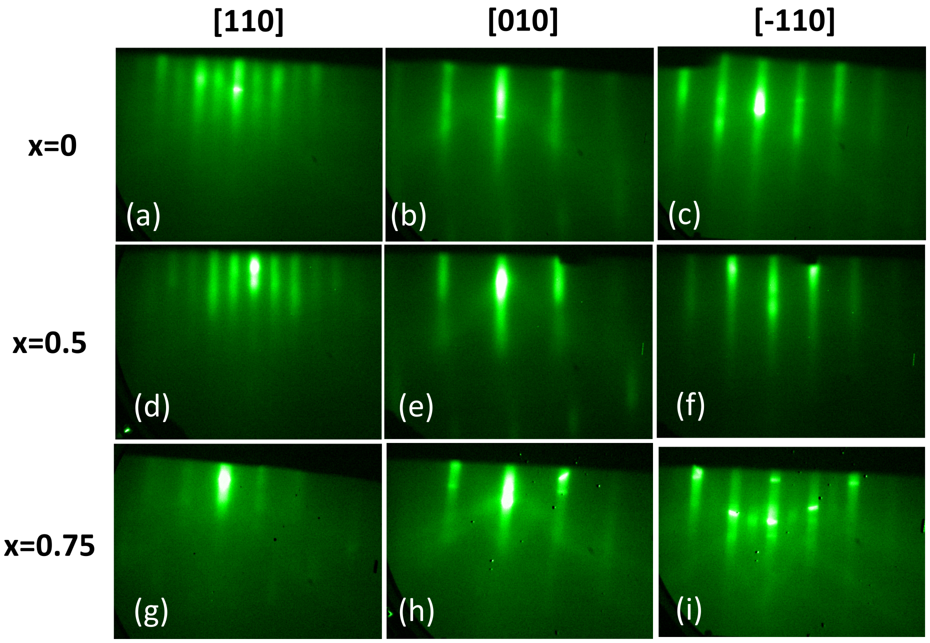

Figure 4.1. Reflection high energy electron diffraction (RHEED) patterns of $Co_{1-x}Ni_xTiSb$ for x=0.1,0.5, and 0.75 along the [110], [010], and [-110] azimuths. A clear (2x1) surface reconstruction in observed for x=0.1 and 0.5, while a disordered (3x2) can be seen in x=0.75.

small variations in the buffer lattice parameter. These XRD patterns combined with the RHEED images, indicate an epitaxial cube-on-cube growth with no detectable secondary phases or orientations.

The additional electrons introduced by nickel alloying is expected to have a strong influence on the electronic properties. Figure 4.3(a) shows the temperature dependent resistivity for $Co_{1-x}Ni_xTiSb$. It can be seen that for low nickel alloying, the film exhibits semiconducting-like transport and thermally activated behavior. As the nickel alloying increases, the magnitude of the resistivity drops, as well as its temperature dependence changes until the nickel composition is greater than x=0.25, where metallic transport emerges.

The thermoelectric properties of the solid solutions were investigated. The measured Seebeck coefficient for a number of compositions is shown in Fig. 4.3(b). Here a negative Seebeck coefficient can be observed for all levels of nickel alloying, consistent with the expectation of nickel being an electron donor. Fur-

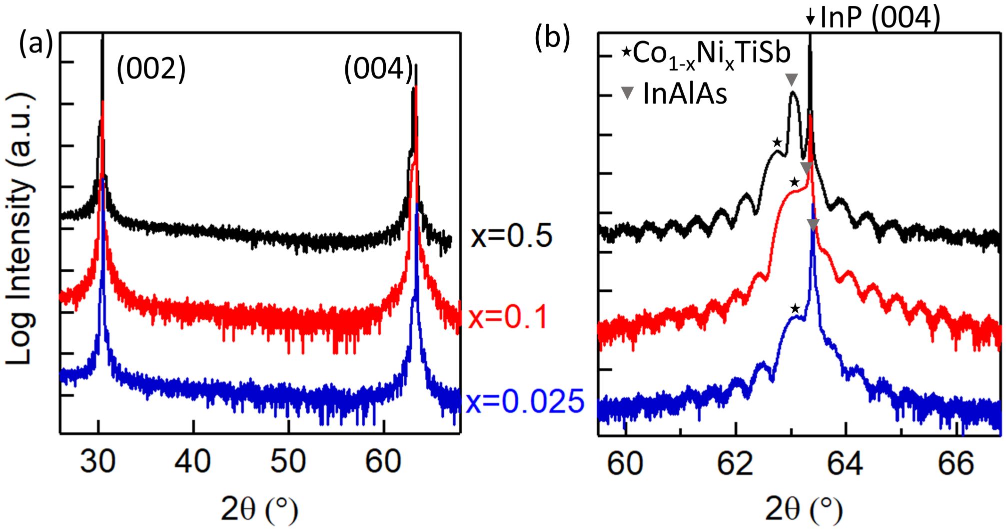

Figure 4.2. XRD 2θ - ω scans for $Co_{1-x}Ni_xTiSb$ films grown on InAlAs/InP(001) for x=0.025, 0.1, and 0.5. (a) Survey scan along (00l) direction. (b) Scan of the (004) reflection.

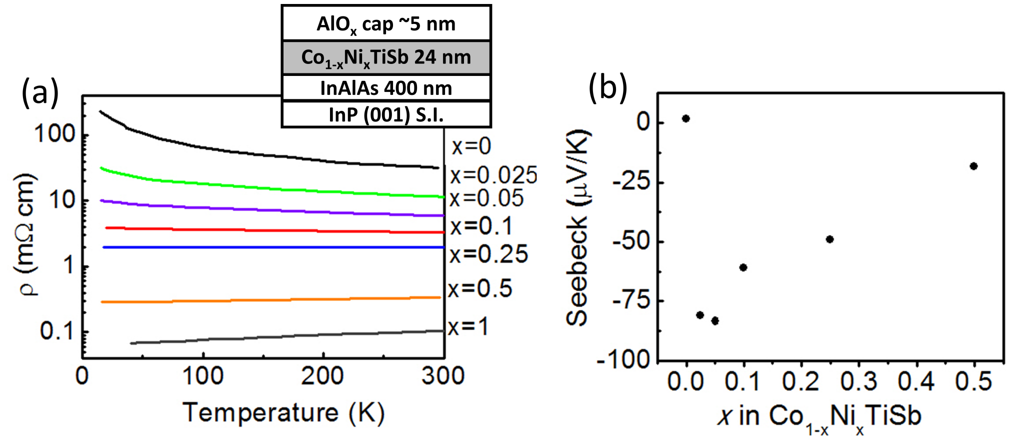

Figure 4.3. (a) Temperature dependent resistivity measurements for 24 nm $Co_{1-x}Ni_xTiSb$ films on InAlAs/InP (001). The sample structure can be seen in the inset. (b) Room temperature measured Seebeck coefficient for $Co_{1-x}Ni_xTiSb$ films. All films were capped with an e-beamed AlO_x layer to prevent oxidation.

thermore, the magnitude of the Seebeck coefficient is largest for small amounts of nickel doping, consistent with previous results reported for vanadium alloying on the titanium site [76]. This peak in the Seebeck coefficient for low nickel doping can be attributed to the large density of states at the Fermi level as it crosses into the conduction band.

4.2 Electronic Structure Investigations

For a better understanding of the evolution of the electronic structure, ARPES measurements were performed on the substitutional alloyed series. To be able to transport samples *ex situ* for ARPES measurements, a thin (∼100 nm) antimony capping layer was used to protect the film surface. Upon reintroduction to UHV, this capping layer was thermally desorbed. Using LEED, a (3x1) surface reconstruction was observed upon initial antimony desorption (Fig. 4.4a) for a sample temperature of 350°C , as measured by a pyrometer. This reconstruction was not previously observed in CoTiSb, but was confirmed to be an antimony rich reconstruction by ultraviolet photoemission spectroscopy (UPS) core levels. Upon further annealing, the observed reconstruction transformed to a mixed (2x1) and c(2x4) (Fig. 4.4b,c). Both the (2x1) and c(2x4) surface reconstructions have been suggested to be an Sb terminated but with less Sb coverage than the (1x4) surface reconstruction [60]. To examine the surface following thermal desorption of the antimony cap, scanning tunneling microscopy (STM) was performed on a decapped $Co_{0.25}Ni_{0.75}TiSb$ samples displayed in Fig. 4.4(d). Here a well ordered surface with large steps can be observed. Additionally, both the c(2x4) seen in LEED as well as a (2x2) surface reconstruction could be resolved (Fig. 4.4d inset). The recovery of the atomically smooth and well-ordered surface upon antimony desorption suggests the capping layer provides the intended protection of the sample surface, but is fully removable upon reintroduction to UHV.

To determine the effects of nickel doping on the band structure, both in-plane

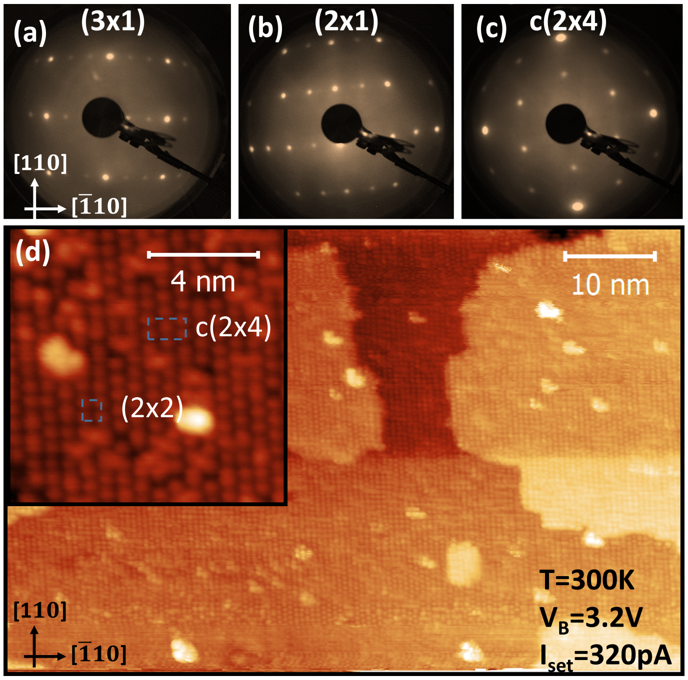

Figure 4.4. (a) (3x1) surface reconstructed LEED image upon initial Sb desorption with a sample temperature of 350°C . (b) (2x1) and (c) c(2x4) LEED images achieved upon further annealing with sample temperature ≥380°C . (d) Empty states STM of decapped $\mathrm{Co_{0.25}Ni_{0.75}TiSb}$. The inset shows a zoomed in region of the scan where both c(2x4) and (2x2) surface reconstructions can be resolved. The surface unit cells are enclosed in the dashed boxes.

and out-of-plane ARPES measurements were performed. First, normal emission ($k_{||}$=0) scans were done as a function of photon energy from 14 to 150 eV. Here, the periodicity of the band structure was matched to the free-electron model to determine the inner potential, U_0=12.0 eV. The measured band structure at normal emission along the Γ - Δ - X direction for a selection of $Co_{1-x}Ni_xTiSb$ films is plotted in Fig. 4.5. For pure CoTiSb, shown in Fig. 4.5(a), the measured band structure is in good agreement with previous reports [60]. A non-dispersing, low-energy surface state at a binding energy of ~0.5eV can be observed. In addition, the slowly dispersing bulk valence bands are clearly visible. These bands are in good agreement with those calculated by density functional theory (DFT). Notably, no evidence of the bulk conduction band can be seen at either X point, consistent with the Fermi level within the gap. Figure 4.5(b) shows the band structure for an x=0.25 film. The majority of features remain unchanged from the pure CoTiSb sample with one notable departure; namely, a clear state at the second X point ($k_\perp$=5.3 $\mathring{A}^{-1}$) near the Fermi level. Although the state at the first X point ($k_\perp$=3.2 $\mathring{A}^{-1}$) is much less obvious, clear intensity can be observed in the individual EDCs. This is because the intensity at these photon energies was significantly reduced. For the higher nickel content films, x=0.5 and x=0.75 (Fig. 4.5(c) and 4.5(d)), the intensity at the bulk X point at the Fermi level increases. In addition, the state can be seen moving to lower binding energies consistent with the conduction band moving down.

A waterfall plot of the measured energy dispersion curves (EDCs) at normal emission for x=0.0 and x=0.5 films are plotted in Fig. 4.6(a) and (b) respectively. Again for x=0.0 the band structure is in good agreement with previous reports [60]. The non-dispersing, low-energy surface state at a binding energy of ~0.5 eV can be clearly resolved. In addition, the slowly dispersing bulk valence bands are clearly visible and have been overlaid with a red line. Again these bands are in good agreement with those calculated DFT with no evidence of the bulk conduction band around 36 eV which corresponds to the X point, consistent with the Fermi level within the gap. For the x=0.5 film again the majority of features remain unchanged from the CoTiSb sample with one notable departure; namely,

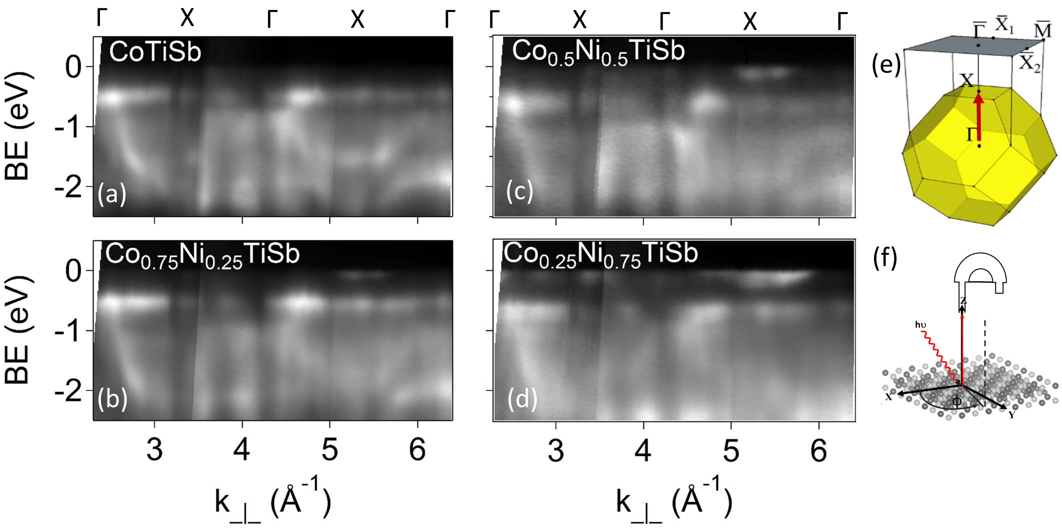

Figure 4.5. Normal emission measurements for $Co_{1-x}Ni_xTiSb$ (001) films. Photoemission intensity as a function of $k_\perp$ assuming free-electron-like final states for (a) x=0.0, (b) x=0.25, (c) x=0.5, and (d) x=0.75. (e) Schematic of the bulk and surface projected Brillouin zones. The normal emission scans probe along the Γ - X direction. (f) Schematic of the normal emission experimental setup.

a clear state at the bulk X point (36 eV) near the Fermi level indicating the Fermi level has crossed into the conduction band. To examine what composition the Fermi level crosses into the conduction band, EDCs were acquired at 36 eV for x=0.0, 0.1, 0.25, 0.5, and 0.75 films, shown in Fig. 4.6(c). For the x=0.0 and 0.1 films only small amount of background intensity can be observed at the Fermi level which can be attributed to non-dispersing in-gap states. In contrast, for x≥0.25 films, a distinct state can be observed at the Fermi energy, which increases for increasing nickel concentration indicating that the Fermi level crosses into the conduction band between x=0.1 and x=0.25. This is consistent with the electrical resistivity data where a semiconductor to metal transition is observed for x>0.1.

EDCs for the bulk Γ point are shown in Fig. 4.6(d). Here only small shifts in the valence band and surface state location to lower binding energies could be seen as the nickel alloying increases. This indicates that at these levels of nickel incorporation the bandgap is decreasing significantly rather than the conduction band moving through a simple rigid band shift. This is consistent with an en-

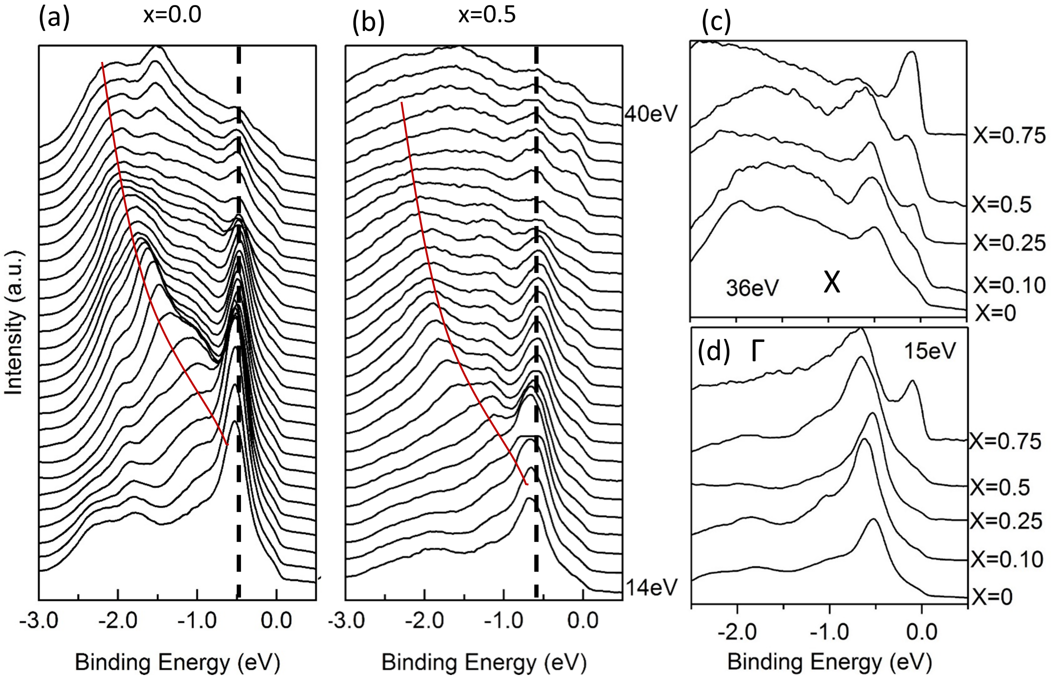

Figure 4.6. Series of valence-band photoemission spectra normal to the (001) surface plane from 14 eV to 39 eV which corresponds to the Γ - Δ - X direction for (a) CoTiSb and (b) $Co_{0.5}Ni_{0.5}TiSb$ films. The dispersive state corresponding to the valence band has been highlighted by the red line. The non-dispersive state near 0.5 eV binding energy corresponds to a surface state seen in all films measured. Valence band spectra at the bulk (c) X (36 eV) and (d) Γ (15 eV) points respectively for five of the compositions measured.

ergy gap reduction expected for NiTiSb [7, 113]. The large level of nickel alloying required to shift the conduction band below the Fermi level suggests that the in-gap states created by antisite and off-stoichiometry defects may significantly reduce the doping efficiency of the nickel atoms. While increased growth temperatures would be expected to reduce these in-gap states, the reactivity of nickel with the underlying buffer limits the optimal growth temperature on III-V based buffer layers. Diffusion barriers such as GdAs could be a route to increase the achievable growth temperature and thus reduce the observed in-gap states.

To investigate the bulk X points more thoroughly, in-plane dispersion scans were taken at photon energies of ∼104eV for x=0.0 and x=0.25, x=0.5, and x=0.75 films corresponding to $k_{\perp}$=5.3 $\mathring{A}^{-1}$. In Fig. 4.7(a-d), constant binding energy surface intensity slices can be seen for a binding energy 80 meV below the Fermi level. Here the same surface states observed in CoTiSb at the surface Brillouin zone X point ($\bar{X}$, k_x=0.75 Å^{-1}) are present with the same periodicity. Although some intensity can be observed at normal emission (k_x,k_y = 0) in the Fermi slice, there is no discernible intensity in the in-plane dispersion at the Fermi level for the x=0.0 or x=0.1 films shown in Fig. 4.7(a) and 4.7(b). This suggests that the Fermi level of the x=0.1 sample is still within the bandgap, although likely near the conduction band. In contrast, a very clear state can be distinguished at normal emission in the Fermi surface of the x=0.25, x=0.5, and x=0.75 samples seen in Fig. 4.7(c-e). This state does not repeat with the surface unit cell, thus is unlikely to be a surface state. By examining the in-plane dispersion at $k_x = 0$ for these higher nickel content films, an upward faced parabola shape can be observed just below the Fermi level, indicative of an electron pocket associated with the conduction band. As the nickel content is increased, the electron pocket can be seen shifting to lower binding energy, consistent with the conduction band moving down.

Beyond the appearance of the conduction band, for the highest nickel content films, a transition in the surface state shape could be observed. For the x=0.75 film, linearly dispersing states are visible crossing the Fermi level at the

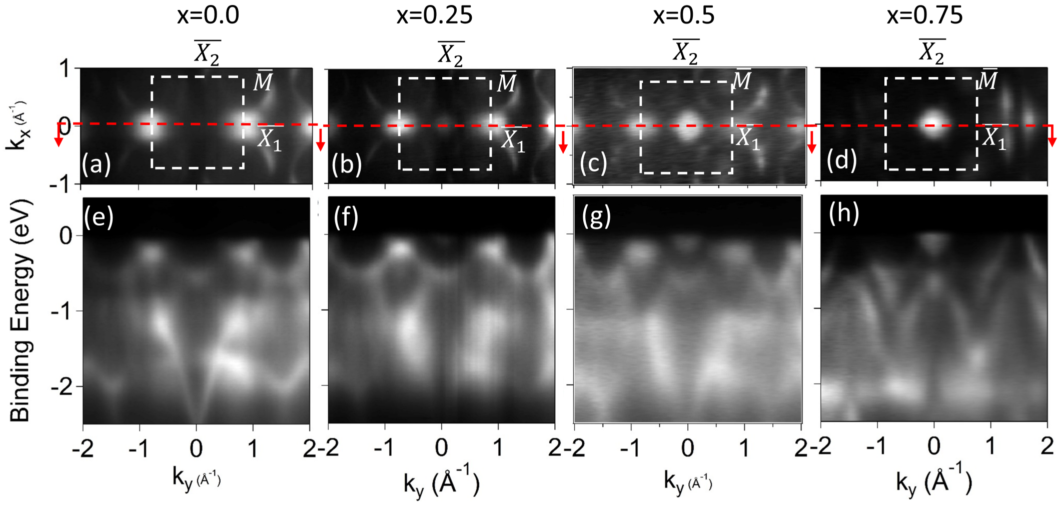

Figure 4.7. In-plane dispersion at ∼104 eV photon energy which is near the bulk X point for the $Co_{1-x}Ni_xTiSb$ films. (a-d) The observed constant binding energy surface at 80 meV below the Fermi level for x=0.0, 0.25, 0.5, and 0.75 films. (e-h) In-plane constant photon energy dispersion maps along the $\bar{\Gamma}$ $\bar{X}_1$ direction.

second surface brillouin zone $\bar{\Gamma}$ point. This dramatic change in surface state may be related to the change in surface reconstruction. For CoTiSb films it was suggested that antimony dimers form the observed (2x1) surface reconstruction [60]. For the highest Ni content film a transition in surface reconstruction to a (3x2) was observed. One possible explanation is an increased presence of Ni in the reconstruction as was seen in NiMnSb thicker films [55]. If nickel dimers were present, multiple components may be present in the core levels for the different bonding states similar to that seen in GaAs and GaSb for As and Sb dimers [114, 115]. However only one doublet split component was visible in the Ni 3p core level. In contrast, multiple components were visible in the Sb 4d core level in all of the films measured.

To determine if antimony surface bonding was still present in the higher nickel content films, angle dependent, angle-integrated X-ray photoemission spectroscopy was performed on the antimony 4d core level of a x=0.88 film. Figure 4.8 shows XPS spectra of the antimony 4d core level at an incident photon energy of 90 eV at normal emission (less surface sensitive) and with the sample rotated 60° (more surface sensitive). Three doublet components are observed,

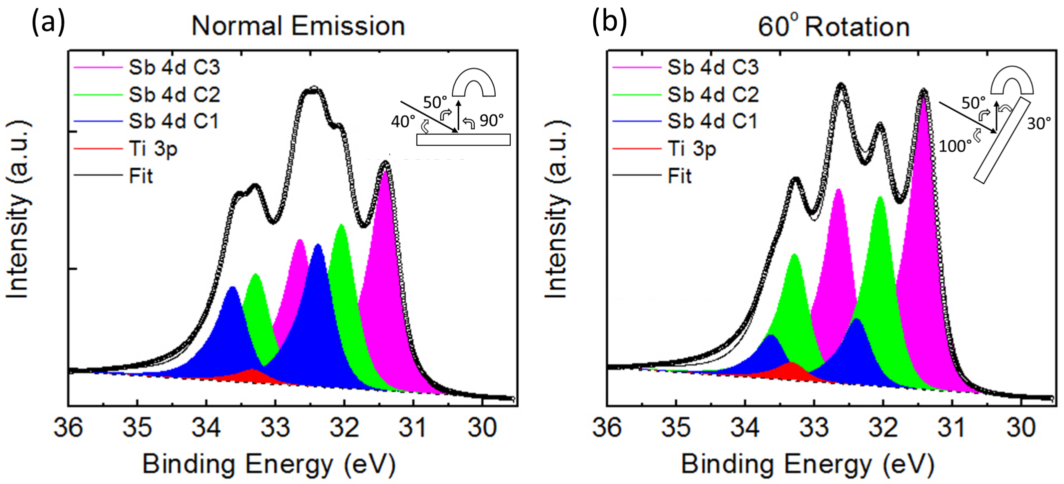

Figure 4.8. XPS measurements of the antimony 4d core level as a function of incident angle. At (a) normal emission; three components are observed. The more surface sensitive (b) rotated 60° scan shows an increase in peak areas of C2 and C3 as compared to C1, indicating C1 is likely bulk and C2 and C3 are surface related.

a bulk as well as two surface components. The two surface components are observed at lower binding energies (ΔBE_{C2}=-0.33±0.03 eV, ΔBE_{C3}=-0.97±0.03 eV). The peak ratios of the two surface components remain nearly constant at 1.4 and 1.5 for normal emission and 60° rotated respectively, while the total bulk ratio (A_{C2+C3}/A_{bulk}) is 2.7 and 6.7 for the normal incidence and 60°rotated spectra respectively. Because the rotated sample geometry has a much shallower angle from the sample to the detector it is more surface sensitive. The larger ratio for the less surface sensitive geometry confirms C1 originates from the bulk and C2 and C3 arise from the bonding at the surface. This is consistent with previous reports of PtLuSb where a bulk and two surface components were observed [116] which was attributed to the dimerization of antimony and broken antimony dimers, similar to that seen in GaSb (001) [114]. Therefore, although a reconstruction and surface state change was visible in the higher nickel content films, a transition from antimony to nickel dimers does not appear to explain it. A thorough theoretical treatment may be necessary to understand the origin of the change in surface state and reconstruction.

Beyond nickel content, the Fermi level position also showed a surface reconstruction dependence. Three different reconstructions were observed in LEED upon antimony desorption from the surface: (3x1), (2x1), and c(2x4) shown in Fig. 4.4(a), 4.4(b), and 4.4(c) respectively. In Fig. 4.9, the photoelectron spectra measured for a x=0.25 film (3x1) and c(2x4) surfaces for photon energies between 14 and 39 eV corresponding to the Γ - Δ - X. Again similar features can be seen in the EDCs of both reconstructions, a slowly dispersing bulk valence band and a nondispersing surface state denoted SS. Here a clear shift to lower binding energies is visible for both the valence bands and surface state. Individual EDCs for the two reconstructions overlaid at 21, 23, and 24 eV are shown in Fig. 4.9(c), 4.9(d), and 4.9(e) respectively. Three notable changes are visible in the spectra. First, a shift of over 0.1 eV is visible between the two reconstructions. Second, an enhancement of the surface resonance for the higher annealed c(2x4) reconstruction is visible. Third, the intensity at the Fermi level for the c(2x4) reconstruction is reduced.

The shift in binding energy can be estimated by fitting Gaussians to the position of the surface state and the valence band in each of the EDCs. The binding energy position of each of the valence band and surface state fits are summarize in Table 4.2. A shift of 0.10 eV and 0.17 eV is observed for the bulk valence band and surface state respectively. The difference in the shift between the surface state and the valence band is likely due to the band bending present. The c(2x4) would have more band bending, thus the bulk valence band would have electrons escaping from different binding energies depending on their distance from the surface when they are initially excited. This would give a reduced shift if (3x1) surface reconstruction has less band bending. This is schematically shown in Fig. 4.10. Thus, it can be estimated that the Fermi level position shifts by $\sim$170 meV to lower binding energies for the annealed c(2x4) surface reconstruction. The change in the Fermi level position could be due to different pinning positions for the two reconstructions or, alternatively, due to change in a surface dipole layer associated with the surface reconstructions. The band bending proposed would also explain the decrease in intensity observed at the Fermi level for the c(2x4) surface some of the conduction band states near

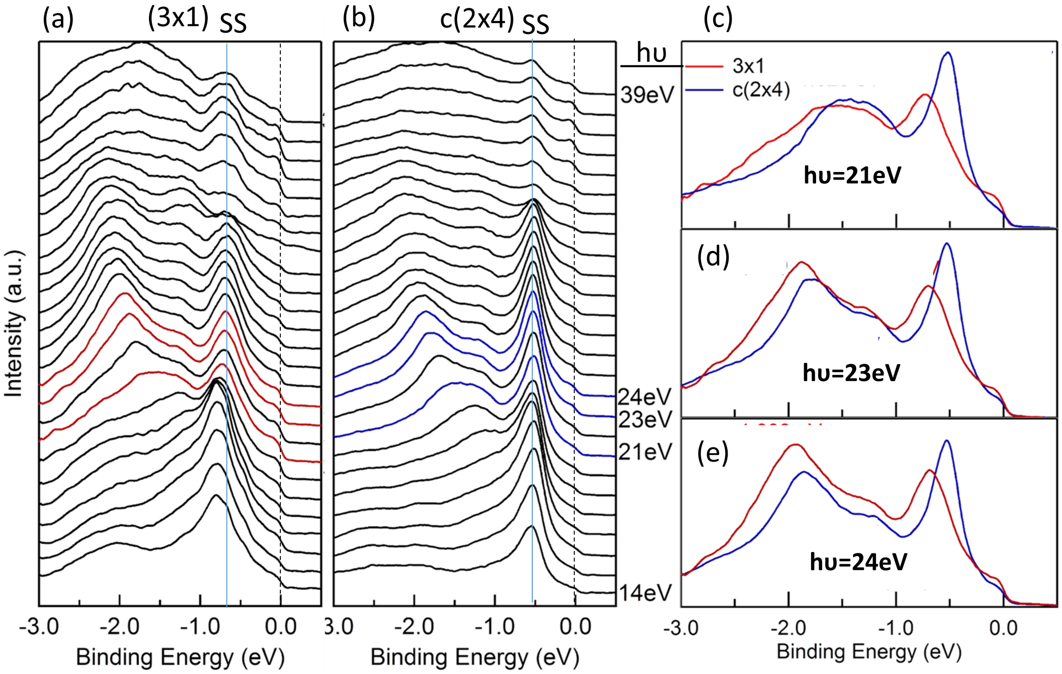

Figure 4.9. Energy dispersion curves as a function of incident photon energy from 14 to 39 eV for $\mathrm{Co_{0.75}Ni_{0.25}TiSb}$ (001), which probes along the Γ - Δ - X direction of the bulk Brillouin zone for (a) the antimony rich (3x1) and (b) further annealed c(2x4) surface reconstructions. (c-e) EDCs measured in normal emission on the two surface reconstructions of $\mathrm{Co_{0.25}Ni_{0.75}TiSb}$ for 21, 23, and 24 eV highlighting the shift in the bands by 0.17 eV to lower binding energy for the higher temperature annealed surface reconstruction, c(2x4).

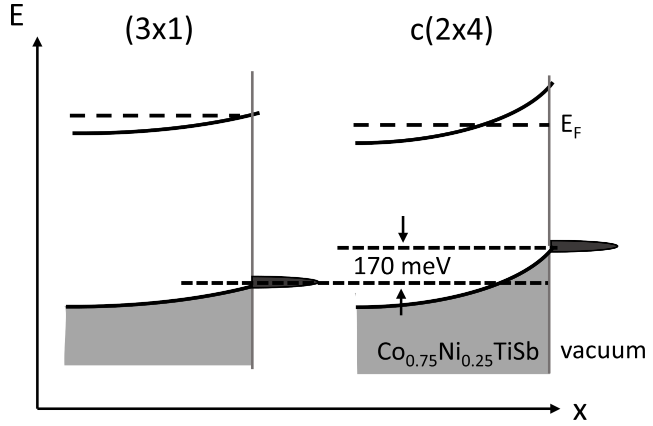

Figure 4.10. Schematic representation of the inferred band bending for the (3x1) and c(2x4) surface reconstructions for the x=0.25 sample. The Fermi level is within the conduction band.

Photon Energy	c(2x4)		(3x1)	
	VB (eV)	SS (eV)	VB (eV)	SS (eV)
21 eV	-1.42	-0.53	-1.52	-0.74
23 eV	-1.78	-0.54	-1.87	-0.70
24 eV	-1.85	-0.54	-1.94	-0.69

Table 4.1. Fitted valence band (VB) and surface state (SS) positions for a selection of photon energies for the c(2x4) and (3x1) surface reconstructions for a x=0.25 film.

the surface would be above the Fermi level. Thus only electrons further from the surface could be photoemitted, lowering the observed intensity.

4.3 Summary

In summary, epitaxial thin films of $Co_{1-x}Ni_xTiSb$ have been grown on InAlAs/InP(001) for 0.0≤x≤1.0. The films are high crystal quality as determined by RHEED and XRD with abrupt smooth interfaces and surfaces. Temperature dependent resistivity and ARPES measurements suggest a semiconductor to metal transition for x>0.1. Surface state, valence band, and conduction band positions depend on both nickel content as well as surface reconstruction. The bandgap energy decreases with increasing nickel content, consistent with expectations from DFT. A change in the Fermi level position at the surface can be observed which depends on surface reconstruction. Finally, a dramatic shift in the surface state band structure can be observed for the highest nickel content films. Future studies should examine the origin of this change.

Chapter 5

Growth, electrical, structural, and magnetic properties of half-Heusler CoTi$_{1-x}$Fe$_x$Sb

One of the original and most sought after properties within the Heusler compounds is 100% spin polarization at the Fermi level, namely half-metallic behavior. The original prediction by deGroot et al. [117] of half-metallicity within the Heusler compound family in NiMnSb prompted the search for other Heusler half-metals. Since the original prediction, many more Heusler compounds have been predicted to be half-metallic, but only few have shown real experimental promise. Many efforts to improve the half-metallic behavior have attempted to tune the Fermi level to the middle of the minority gap through alloying to maximize the magneto tunneling effect [49–51]. In this chapter, an alternative technique is examined to achieve a half-metal; the magnetism is introduced to the semiconductor CoTiSb by alloying with Fe.

By substitutionally alloying Fe into the Ti site, a net gain of four valence electrons per formula unit (f.u.) is obtained, and CoTiSb undergoes a transition from a non-magnetic semiconductor to a ferromagnet [75]. A dilute magnetic semiconductor with a high Curie temperature was reported for low levels of Fe alloying in bulk single crystals [118], which could be useful for spintronic applications such as MTJs or spin injection into nonmagnetic materials. However, for many device applications thin films are a necessary requirement. Previous work by Sun et al. [71] reported the growth and properties of Fe alloyed CoTiSb epitaxial thin films prepared by the magnetron sputtering method. For the intrinsic CoTiSb thin films, carrier concentrations of $\sim 10^{21}$ cm^{-3} and mobilities of ~ 2 cm^2/V s at room temperature were reported, which was attributed to Ti-deficiency. In addition, because the Fe was introduced by adding Fe flakes to the CoTiSb sputter target, the composition and stoichiometry of the film could not be closely controlled. In the present study, epitaxial thin films of Fe alloyed CoTiSb are grown by molecular beam epitaxy (MBE), which allows for the precise control of stoichiometry. The growth, structural, magnetic, and transport properties of the resulting films and their dependence on Fe content are discussed and compared to calculations based on density functional theory (DFT).

For this study, CoTi$_{1-x}$Fe$_x$Sb samples were grown in the Heusler VG V80 MBE system on nearly lattice-matched unintentionally doped In$_{0.52}$Al$_{0.48}$As (referred to as InAlAs) buffer layers epitaxially grown on semi-insulating InP:Fe (001) substrates as described in chapter 3. The InAlAs layers were 400 nm thick, grown in a separate conventional III-V MBE system and then arsenic capped and transferred through air into a dedicated metals MBE system for growth of the CoTi$_{1-x}$Fe$_x$Sb layers. After the samples were reintroduced to ultra-high vacuum (UHV), the arsenic cap was desorbed to reveal the As-terminated (2x4)/c(2x8) InAlAs surface. CoTi$_{1-x}$Fe$_x$Sb thin films were grown by simultaneous evaporation of Co, Ti, Fe, and Sb using stoichiometric fluxes with a total flux of 9x10^{16} atoms/cm^2 hr, giving an approximate growth rate of 2.5 Å/min. 9x10^{16} atoms/cm^2 were deposited for each film which corresponds to approximately 15 nm for pure CoTiSb. All fluxes were calibrated *ex situ* by measuring the elemental atomic areal density of calibration sample layers grown on Si substrates using Rutherford backscattering spectrometry (RBS). Samples were grown at temperatures in the range 200-380°C as measured by a thermocouple that is calibrated to the arsenic desorption temperature of arsenic capped GaAs [99]. The surface was monitored *in situ* during growth using reflection high-energy electron diffraction (RHEED). Following growth, samples were cooled down before UHV transfer to an e-beam evaporator for room temperature deposition of a ∼10 nm amorphous AlO_x protective capping layer.

The crystal structure and magnetic properties were analyzed *ex situ* using X-ray diffraction (XRD), superconducting quantum interference device (SQUID) magnetometry, and ferromagnetic resonance (FMR). SQUID magnetometry field sweeps were conducted at 5K following a 5000 Oe-field cooldown with separate sweeps with the applied field along the [110], [100], and [001] (out-of-plane) crystallographic directions. Magnetic moment vs temperature data were collected with a 100 Oe field applied from 5 to 400 K. The FMR spectra were collected on a conventional x-band (=9.8GHz) Jeol-FA300 spectrometer. The measurements were performed in 110 - 350 K temperature range using a Jeol LN_2 flow cryostat. Electrical characterization was performed between 2 and 300 K in a He-4 cryostat using a standard dc technique in a L-shaped Hall bar geometry of length 1 mm (longitudinal voltage leads were spaced 200 μm apart and 150 μm wide) aligned along the [110] and [-110] directions. Hall bars were fabricated using contact lithography and Ar ion milling with e-beam deposited Ti/Au contacts. R vs H measurements were performed with a constant applied current while measuring V_{xx} and V_{xy} so as to determine R_{xx} and R_{xy} components simultaneously during the out-of-plane magnetic field sweep from 100 kOe to 100 kOe and back to 100 kOe.

The magnetization and density of states were calculated by Abhishek Sharan at the University of Deleware using DFT [119, 120] with the revised Perdew-Burke-Ernzerhof functional for solids for exchange and correlation (PBEsol) [105] as implemented in VASP code [121, 122]. The interactions between the valence electrons and the ionic cores are treated using projector-augmented wave potentials [123, 124]. The random alloy structures, for varying Fe concentration, were generated using special quasi-random structures (SQS) [125] based on a 90-atom supercell that were determined with the Alloy Theoretic Automated Toolkit (ATAT) code [126]. SQS has been successful in describing the electronic and thermodynamic properties of various disordered systems [127–129]. The calculations are performed using an energy cutoff of 350 eV for plane-wave basis set expansion and a grid of Γ-centered 6x6x6 k-points in reciprocal space for integrations over the Brillouin zone.

5.1 Surface, structural, and electronic characterization

During growth, a (2x1) surface reconstruction was inferred from bright, streaky RHEED patterns for $x \leq 0.5$ (Fig. 5.1), similar to that observed in intrinsic CoTiSb [58, 130]. For the pure CoFeSb film, the RHEED pattern consisted of faint streaks as well as bulk diffraction spots indicating roughening of the surface and lower film quality. To minimize interfacial reactions and phase segregation, a lower growth temperature was necessary as the Fe content was increased. This is similar to low-temperature MBE required to achieve (Ga,Mn)As thin films [131]. However, polycrystalline rings were observed in RHEED below 200°C growth temperature. Therefore, for the highest Fe content film, an optimal growth temperature of 200° C was used to maintain single crystal growth of CoFeSb.

Figure 5.2 shows XRD 2θ-ω scans for CoTi$_{1-x}$Fe$_x$Sb films for x=0.0, 0.2, 0.3, 0.5, and 1.0 grown on InAlAs/InP (001). The sharp peaks at 2θ=30.44° and 63.34° correspond to the InP (002) and (004) substrate reflections, respectively. The CoTi$_{1-x}$Fe$_x$Sb and InAlAs (002) and (004) peaks are nearly overlaid on the InP peaks indicating the close lattice match. Other than the (00l) peaks and thickness fringes, no additional peaks in the XRD scans are observed. Figure 5.2(b) shows a scan centered around the (004) reflection. Here, finite thickness

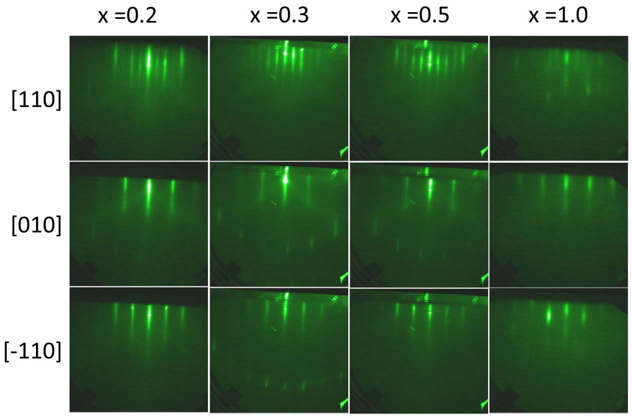

Figure 5.1. RHEED patterns of CoTi$_{1-x}$Fe$_x$Sb for x=0.2, 0.3, 0.5 and 1.0 along the [110], [010], and [-110] azimuths respectively. A clear (2x1) surface reconstruction is observed for x$\leq$0.5 similar to that seen in pure CoTiSb. Reprinted from [132] with permission from *American Physical Society.*

fringes can be clearly resolved for x$\leq$0.5 corresponding to a thickness of 15.6, 14.4, 14.3, and 13.3 nm for x=0.0, 0.2, 0.3, and 0.5 respectively, in good agreement with the film thickness expected from the RBS calibrations. These fringes indicate a smooth, abrupt interface between the CoTi$_{1-x}$Fe$_x$Sb and InAlAs for up to x=0.5. While no thickness fringes could be observed in x=1.0 film centered around the (004) peak, fringes centered about the (002) peak could be resolved. The additional large peak observed in each scan corresponds to the InAlAs buffer layer. Small deviations from the intended composition of In$_{0.52}$Al$_{0.48}$As led to variations of the lattice parameter. The broad peak to the left for x$\leq$0.5 and to the right for x=1.0 of InP are from the CoTi$_{1-x}$Fe$_x$Sb films. A small increase in the out-of-plane lattice parameter from 5.88 Å for pure CoTiSb is observed as Fe content is first increased with a dramatic decrease for the pure CoFeSb (5.81 Å). The lattice parameter of CoFeSb agrees with the theoretically predicted value of 5.81 Å [102]. The observed lattice parameter bowing can partially be attributed to slightly different strain conditions due to variation in the buffer lattice parameter. These XRD patterns combined with the RHEED images, indicate an epitaxial cube-on-cube growth with no detectable secondary phases or orientations and are suggestive of abrupt interfaces and high crystalline quality for the films with lower iron content.

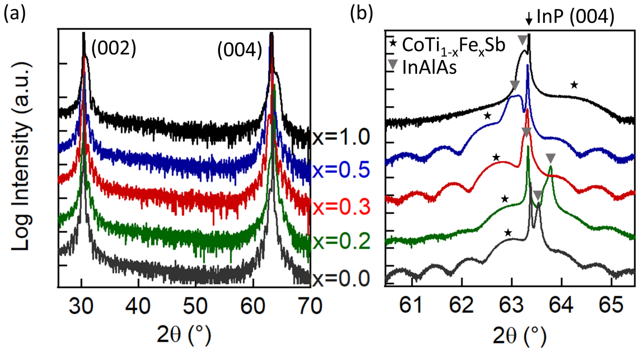

Figure 5.2. XRD 2θ-ω scans for the $\text{CoTi}_{1-x}\text{Fe}_x\text{Sb}$ films for x=0.2, 0.3, 0.5 and 1.0 grown on InAlAs/InP(001). (a) Survey scan along $(00l)$ direction. (b) Close up of the (004) reflection. Reprinted from [132] with permission from *American Physical Society.*

The effect of Fe on the CoTiSb electronic structure was probed by performing *in-situ* XPS on intrinsic CoTiSb, $\text{CoTi}_{0.2}\text{Fe}_{0.2}\text{Sb}$, and $\text{CoTi}_{0.5}\text{Fe}_{0.5}\text{Sb}$ and compared to DFT calculated density of states (DOS)[1]. The calculated DOS for $\text{CoTi}_{1-x}\text{Fe}_x\text{Sb}$ for x = 0.0, 0.2 and 0.5 is shown in Fig. 5.3(a). As expected, we find pure CoTiSb to be a semiconductor, and $\text{CoTi}_{1-x}\text{Fe}_x\text{Sb}$ with x=0.2 and 0.5 to be metallic. The shape of the DOS in the valence band for x = 0.2 and 0.5 follows that of the pure CoTiSb, since these are composed mostly of Co and Sb orbitals. The bands above the Fermi level changes for x=0.5 compared to pure CoTiSb, which is expected since the conduction band (up to ~3 eV) has major contributions from the Fe and/or Ti atoms. The normalized valence band spectra excited by Al Kα radiation are shown in Fig. 5.3(b). For the CoTiSb spectrum, good agreement is observed with the DOS and resembles previously reported spectra at similar excitation energies [48, 71, 75, 130]. For the x=0.2 and x=0.5 films, the spectra show similar structure to that of CoTiSb with only a few small binding energy shifts, consistent with the calculated DOS. Here good agreement between the calculated DOS and the measured valence band spectrum is observed, suggesting no additional, non-half-Heusler (h-H) phase is present.

---

[1] Calculations courtesy of Abhishek Sharan and Anderson Janotti, University of Deleware

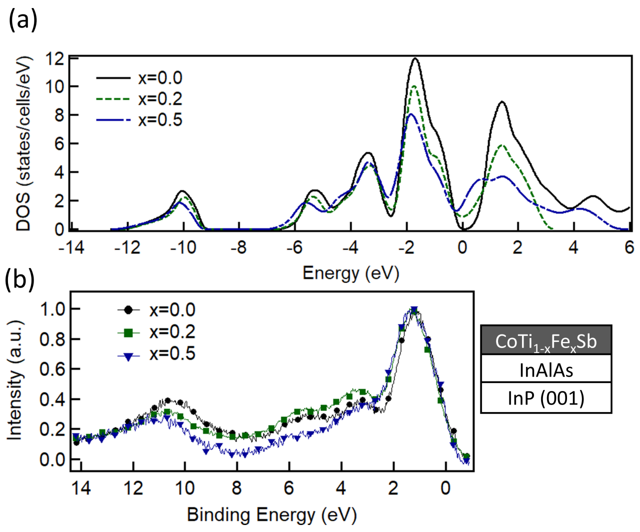

Figure 5.3. (a) Calculated total density of states plot for $\mathrm{CoTi}_{1-x}\mathrm{Fe}_x\mathrm{Sb}$ for x = 0.0, 0.2 and 0.5 courtesy of A. Sharan and A. Janotti. (b) Normalized valence band XPS spectra collected for $\mathrm{CoTi}_{1-x}\mathrm{Fe}_x\mathrm{Sb}$ with x=0.0, 0.2, and 0.5 excited by Al Kα radiation. Reprinted from [132] with permission from *American Physical Society.*

5.2 Magnetic properties

The magnetic properties of the alloy series were studied using ex-situ SQUID magnetometry and FMR. From SQUID magnetometry, ferromagnetic order was observed for $\mathrm{CoTi}_{1-x}\mathrm{Fe}_x\mathrm{Sb}$ films with $x \geq 0.05$ within the detection limit of the measurement. In-plane hysteresis loops with the applied field oriented along the [110] direction taken at 5K are shown in Fig. 5.4(a). The saturation magnetization of the films increases with increasing Fe content, which was used to calculate the net contribution of an iron atom to the total magnetic moment per f.u. in units of Bohr magneton (μ_B). Additionally, a decrease in the coercive field from 500 to 10 Oe for compositions from x=0.1 to x=1.0 can be observed. The magnetic moment per f.u. is plotted in Fig. 5.4(b). A linear dependence of 3.9 μ_B/Fe atom is observed up to x=0.5, close to the Slater-Pauling expected 4 μ_B/Fe atom-f.u [118]. However, including pure CoFeSb in the fit, which displays 3.2 μ_B/f.u., gives an overall linear fit of 3.3 μ_B/Fe atom f.u. This deviation from the well-behaved linear fit observed at low iron concentration may be caused by poor crystal quality for the CoFeSb sample. The error bars are from dif-

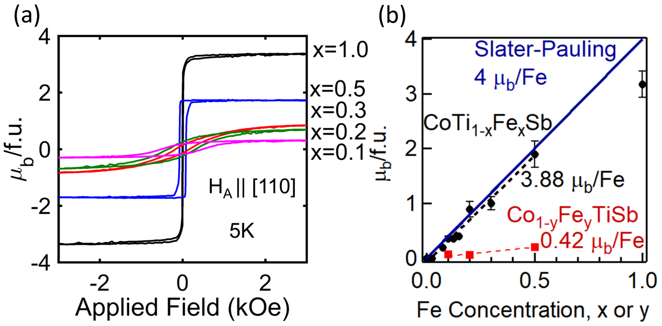

Figure 5.4. (a) SQUID magnetic hysteresis curves of 15 nm thick $\mathrm{CoTi}_{1-x}\mathrm{Fe}_x\mathrm{Sb}$ films for x=0.1, 0.2, 0.3, 0.5, and 1.0 at 5 K with the magnetic field applied along the [110] sample direction. (b) Magnetic moment per f.u. dependence on Fe concentration. Solid black circles and red squares are data points for $\mathrm{CoTi}_{1-x}\mathrm{Fe}_x\mathrm{Sb}$ and $\mathrm{Co}_{1-y}\mathrm{Fe}_y\mathrm{TiSb}$ films respectively. Solid blue, dashed black, and dashed red lines correspond to the Slater-Pauling predicted 4 μ_B/Fe atom, linear fit to the $\mathrm{CoTi}_{1-x}\mathrm{Fe}_x\mathrm{Sb}$ data, and linear fit to the $\mathrm{Co}_{1-y}\mathrm{Fe}_y\mathrm{TiSb}$ data respectively. Reprinted from [132] with permission from *American Physical Society.*

ferences in saturation magnetization measured for the distinct crystallographic directions. These differences arise due to the finite sample size effects on the SQUID pickup coils [133].

Previously, Kroth et al. studied bulk $\mathrm{CoTi}_{1-x}\mathrm{Fe}_x\mathrm{Sb}$ crystals with x=0.05 and 0.1 and obtained m=3.5 μ_B/Fe atom-f.u and m=3.7 μ_B/Fe atom, respectively[118] consistent with the results reported here. Sun et. al. investigated Fe doped CoTiSb films on MgO (001) up to 37% doping ratio and obtained m=3 μ_B/f.u for 20 nm thick films. The deviations from the expected value of 4 μ_B/Fe atom have been attributed to disorder on the site occupancy of the Fe atom. It was suggested that Fe atoms occupying alternative Wyckoff positions are expected to contribute significantly less magnetic moment [118]. Thus the discrepancies on the measured bulk spin moment per Fe atom may be correlated with the difficulty in preparing well-ordered and stoichiometric films. For example, FeTiSb would be expected to have -1 μ_B/f.u. from the simplified m = N_V-18 Slater-Pauling curve. Thus Fe occupying other sites would be expected to contribute less magnetic moment. To verify this, the substitutional series $\mathrm{Co}_{1-y}\mathrm{Fe}_y\mathrm{TiSb}$ was grown with the intent of replacing Co with Fe, and the magnetic properties measured. The saturation magnetic moments for films with

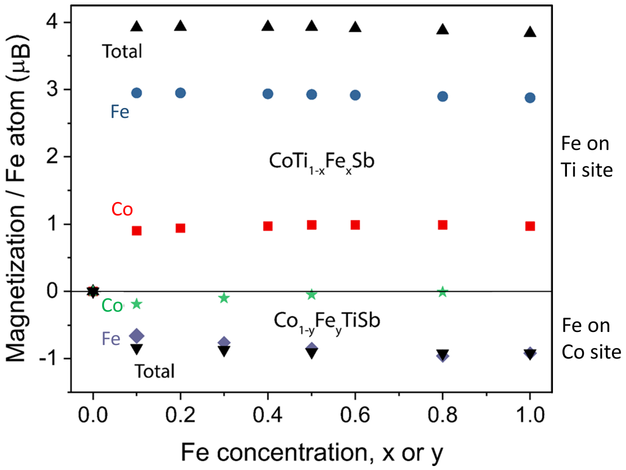

Figure 5.5. Calculated contributions to the total magnetization per Fe atom as a function of Fe concentration in $\mathrm{CoTi}_{1-x}\mathrm{Fe}_x\mathrm{Sb}$ and $\mathrm{Co}_{1-y}\mathrm{Fe}_y\mathrm{TiSb}$ alloys courtesy of A. Sharan and A. Janotti.. Note that the contribution from all the Co (or Fe) atoms are added up and divided by the number of Fe atoms in the supercell, with the largest contributions from the Co atoms sitting next to an Fe. The contributions from Ti and Sb atoms are negligible, i.e., less than 0.05 μ_B in magnitude, for all Fe concentrations. Reprinted from [132] with permission from *American Physical Society.*

y=0.1, y=0.2, and y=0.5 are plotted in Fig. 5.4(b). Again, a linear dependence with Fe content is found; however, a drastically reduced net magnetic moment of 0.42 μ_B/Fe atom is observed. This discrepancy is likely due to disorder within the films.

To understand the effects of Fe alloying and disorder, the total magnetization of $\mathrm{CoTi}_{1-x}\mathrm{Fe}_x\mathrm{Sb}$ and $\mathrm{Co}_{1-y}\mathrm{Fe}_y\mathrm{TiSb}$ atomically resolved moments were calculated using DFT for $\mathrm{CoTi}_{1-x}\mathrm{Fe}_x\mathrm{Sb}$ and $\mathrm{Co}_{1-y}\mathrm{Fe}_y\mathrm{TiSb}$, as well as several structures with mixed alloying or antisite swap defects. When Fe atoms substitute on the Ti sites in CoTiSb, the total magnetization of the alloy increases by 3.92 μ_B per Fe atom, as shown in Fig 5.5, though the magnetization in pure CoFeSb drops to 3.84 μ_B. The observed magnetic moment of about 4 μ_B per Fe atom in the $\mathrm{CoTi}_{1-x}\mathrm{Fe}_x\mathrm{Sb}$ alloys arises from strong d-d coupling between Co and Fe d orbitals and spin splitting, with ∼3 μ_B centered on Fe atoms and ∼1 μ_B centered on Co atoms, for all Fe concentrations.

Alternatively, when Fe is substituted on the Co sites in $\mathrm{Co}_{1-y}\mathrm{Fe}_y\mathrm{TiSb}$, there is an expected reduction in the overall net magnetization due to the Fe atom and it has the opposite sign to that for Fe on Ti sites, $\mathrm{CoTi}_{1-x}\mathrm{Fe}_x\mathrm{Sb}$. From DFT calculations summarized in Fig 5.5, the total magnetization per Fe atoms jumps to -0.84 μ_B for x=0.1 and then saturates to -0.90 μ_B for higher Fe concentrations. The projected density of states on Co, Fe and Ti d orbitals are shown in Fig 5.6(b) for the $\mathrm{Co}_{0.5}\mathrm{Fe}_{0.5}\mathrm{TiSb}$ alloy. In this case, as well as lower Fe compositions, most of the magnetization is concentrated on the Fe atoms with negligible contributions from the neighboring Co or Ti atoms. This is consistent with the previous results [102]. Note that the magnetic moment observed in this case has the opposite sign of that calculated in the case of $\mathrm{CoTi}_{1-x}\mathrm{Fe}_x\mathrm{Sb}$. To check if this sign reversal is preserved in the case of mixed site alloying we calculate magnetization in $\mathrm{Co}_{1-y}\mathrm{Ti}_{1-x}\mathrm{Fe}_{x+y}\mathrm{Sb}$ (x=y) for different Fe concentrations, in which half of the Fe atoms were substituted on the Co site and another half on Ti site. In this case, we observe net magnetic moment of 1.5 μ_B/Fe atom, consistent with the Slater-Pauling rule. The magnetic moments from Fe on Co (Fe_{Co}) and Fe on Ti (Fe_{Ti}) sites partially compensate each other, in agreement with the sign reversal observed for the two ordered alloy systems. Finally, we also calculated the moment for the alloy series with complete Co_{Ti} disorder $(\mathrm{Co}_{1-y}\mathrm{Fe}_y)(\mathrm{Ti}_{1-x}\mathrm{Co}_x)\mathrm{Sb}$ (x=y), where Fe atoms substitute on the Co site and the displaced Co occupies the induced vacancies in the Ti site. Interestingly, the calculated magnetic moment in this case is $\sim$2.38 μ_B/Fe atom, which deviates significantly from the magnetic moment expected from Slater Pauling rule of 4.0 μ_B/Fe atom. This disorder induced deviation from Slater-Pauling is consistent with that predicted in NiMnSb, where even a few percent disorder reduced the net magnetization [134]. The magnetic moment calculated for different stoichiometry/disorders arising from Fe atoms occupying different sites are summarized in Table 5.2.

Therefore, the observed magnetic moment of 0.42 μ_B/Fe atom for the substitutional series $\mathrm{Co}_{1-y}\mathrm{Fe}_y\mathrm{TiSb}$ can be explained as arising from disorder in occupation of Fe atoms, i.e., having a mix of Fe_{Co} and Fe_{Ti} sites. Due to the sign ambiguity in experimentally measured magnetic moments, two values are possi-

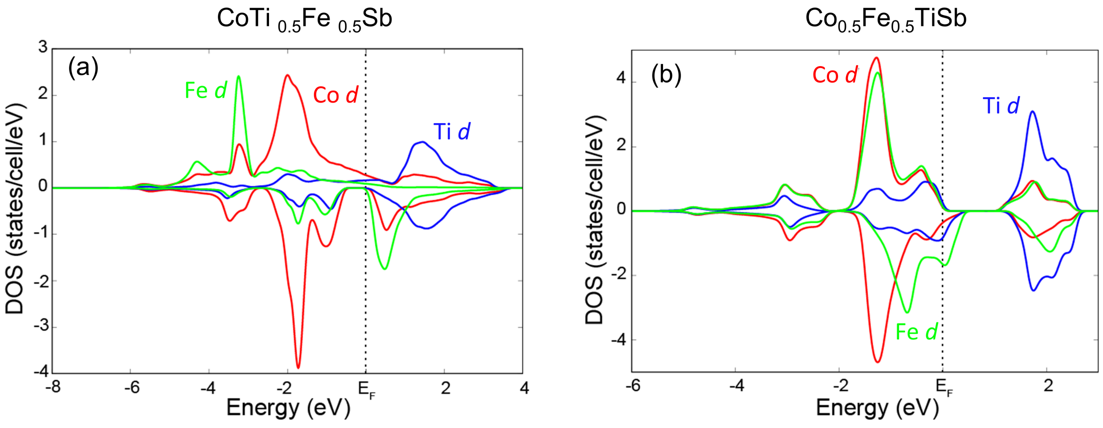

Figure 5.6. Projected Density of States for (a) $\mathrm{CoTi_{0.5}Fe_{0.5}Sb}$ and (b) $\mathrm{Co_{0.5}Fe_{0.5}TiSb}$ on Co, Fe and Ti d orbitals courtesy of A. Sharan and A. Janotti. Reprinted from [132] with permission from *American Physical Society*.

Stoichiometry	No. of Valence Electrons	Slater-Pauling (in μ_B / Fe)	Calculated Magnetic moment (in μ_B / Fe)
$\mathrm{CoTi}_{1-x}\mathrm{Fe}_x\mathrm{Sb}$	18+4x	4.0	3.92
$\mathrm{Co}_{1-y}\mathrm{Fe}_y\mathrm{TiSb}$	18-y	-1.0	-0.90
$\mathrm{Co}_{1-y}\mathrm{Ti}_{1-x}\mathrm{Fe}_{x+y}\mathrm{Sb}$ (x=y)	18+4x-y	1.5	1.48
$(\mathrm{Co}_{1-y}\mathrm{Fe}_y)(\mathrm{Ti}_{1-x}\mathrm{Co}_x)\mathrm{Sb}$ (x=y)	18+4y	4.0	2.38

Table 5.1. Comparison between calculated magnetic moment from density functional theory and expected magnetic moment from Slater Pauling rule (in μ_B/Fe) for different stoichiometries/disorders of Fe substitution in CoTiSb.

ble for the site ordering ratio in this system. For a positive magnetic moment of 0.42 μ_B/Fe, we predict a ratio of $\mathrm{Fe}_{Co}/\mathrm{Fe}_{Ti} \approx 2.6$, while a negative magnetic moment would give a ratio of $\mathrm{Fe}_{Co}/\mathrm{Fe}_{Ti} \approx 9$. For the $\mathrm{CoTi}_{1-x}\mathrm{Fe}_x\mathrm{Sb}$ films, a higher magnetic moment is indicative of better ordering within the film of Fe occupying the Ti site. Thus the observed trend of 3.9 μ_B/Fe atom for lower Fe content films suggests that the MBE prepared thin films are well ordered with the majority of Fe atoms occupying the Ti site.

In addition to site disorder calculations, spin resolved density of states was calculated for select concentrations of the ordered alloys. The projected density of states on Co, Ti and Fe d orbitals are shown in Fig 5.6(a) for the $\mathrm{CoTi_{0.5}Fe_{0.5}Sb}$ alloy. The spin down density of states is zero with non-zero spin up density of states at Fermi level, suggesting the alloy to be half-metallic. In fact, we found that alloys with up to x=0.5 are half-metallic.

To better understand the magnetic switching behavior and anisotropy in the $\mathrm{CoTi}_{1-x}\mathrm{Fe}_x\mathrm{Sb}$ system, a detailed SQUID analysis was performed. Figure 5.7 shows hysteresis loops for the x=0.3 and x=0.5 samples with the applied field along the [110], [100], and [001] crystallographic directions. The [110] and [100] correspond to the field in the plane of the film, while the [001] is out of plane. For the x=0.3 film (Fig. 7a), remanence can be observed in all three directions with the largest coercive field (H_c=600 Oe) observed in the [001] direction. Additionally, there is no clear easy axis. This suggests that the magnetic moments on the Fe atoms are only weakly coupled. In contrast, for the x=0.5 film (Fig. 5.7b) only the in plane ([110] and [100]) directions show clear remanence with an easy axis along the [110] direction. The small remanence observed in the [001] direction can be attributed to small misalignment of the sample in the SQUID sample tube and reflects a small in-plane component contributing to the signal. The difference in crystallographic dependence between the two samples indicates a competition between the magnetic anisotropy terms for the different composition films. XRD reciprocal space maps reveal the films do not possess a significant tetragonal distortion, and magnetocrystalline anisotropy would not be expected to contribute to perpendicular anisotropy in cubic Heusler crystals. Surface or interface anisotropy typically depends on the interface chemical bonding (e.g. CoFeB/MgO) [135] but may also depend on interfacial strain. Changing lattice constants as a function of Fe content, with resulting changes in strain condition, could explain the perpendicular spin reorientation transition [136], however such changes in strain condition were small. Films with high magnetic moment per volume have a correspondingly large shape anisotropy, which tends to confine magnetization into the plane of the film. As the moment per volume of a thin film decreases, shape anisotropy decreases, allowing any surface anisotropy present to dominate. We speculate that for x=0.3, shape anisotropy

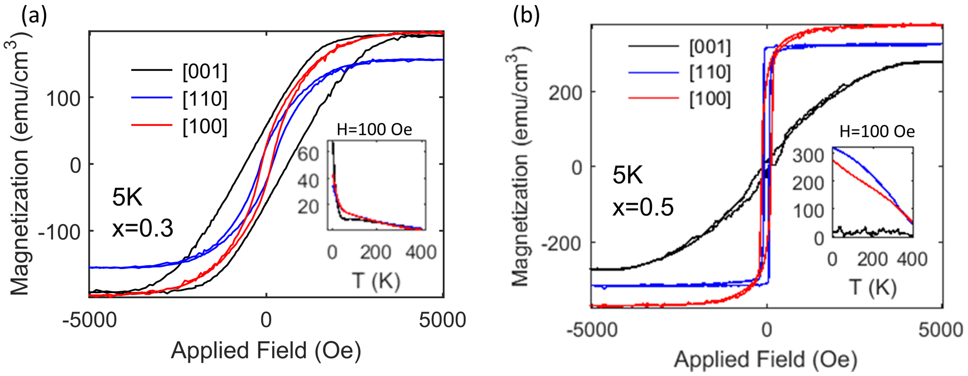

Figure 5.7. Magnetization hysteresis loops for (a) $\mathrm{CoTi_{0.7}Fe_{0.3}Sb}$ and (b) $\mathrm{CoTi_{0.5}Fe_{0.5}Sb}$ with the applied magnetic field along different crystallographic directions at 5K. [110] and [100] are in-plane directions while [001] is out-of-plane. The insets show the temperature dependence of the magnetic moment between 5 and 400 K with 100 Oe applied field. Adapted from [132] with permission from *American Physical Society.*

is sufficiently low that interface anisotropy dominates, but is large enough for x=0.5 to confine the magnetization in the film plane. For lower Fe content films, the strength of magnetic interactions are too small to produce strong magnetic ordering and anisotropy.

The temperature dependence of the magnetic moment can be seen in the insets of Fig. 5.7. For the film with x=0.3, a sharp decrease in the magnetic moment is observed upon warming, with a dramatic change in slope around 50 K, whereupon a more gradual decrease is observed. The large change in slope is suggestive of a magnetic phase transition. The nature of this possible phase transition will be discussed in section 5.4. In contrast, the x=0.5 sample shows a Curie-Weiss like temperature dependence, with a gradual decrease in the magnetic moment for increasing temperature and a Curie temperature beyond 400 K. While the highest temperature measurable in the SQUID magnetometer used was 400K, the Curie point for the films can be estimated to be between 400 and 500K. The lower Curie point observed here compared to x=0.1 bulk crystals (¿700K) [75] is likely related to the thin film nature of the layers.

The magnetic anisotropy and microscopic nature of the films were investigated further by means of FMR. FMR spectra were measured in two different

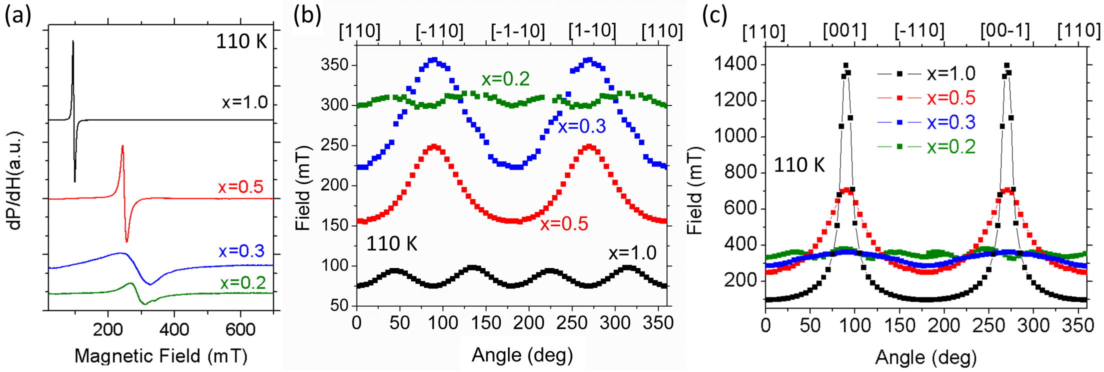

Figure 5.8. (a) In-plane FMR spectra for the $CoTi_{1-x}Fe_xSb$ alloy series for x=0.2, 0.3, 0.5, and 1.0. Angular dependence of FMR field observed at 110K for $CoTi_{1-x}Fe_xSb$ films for (b) in-plane measurement geometry in Cartesian coordinates and (c) out-of-plane in Cartesian coordinates. FMR courtesy of Leyla Colakerol. Adapted from [132] with permission from *American Physical Society.*

rotation planes. The in-plane FMR spectra for the $CoTi_{1-x}Fe_xSb$ alloy series is shown in Fig. 5.8(a), for which the resonance field can be determined as the field where dP/dH=0 line cuts the dP/dH vs H curve. Consistent with the magnetization measurements, we observe a strong enhancement in the intensity of the FMR spectra as the Fe content increases. In addition, a shift of the resonance positions to lower fields, and decrease of the peak-to-peak line width is observed with increasing Fe concentrations. The decrease of average resonance field with increasing Fe concentration indicates the enhancement of internal field and inter-particle (exchange) interactions due to closer possible distances between magnetic ions. The broadening of the linewidth with decreasing Fe content is due to the presence of the non-homogeneous local magnetic field, which modifies the resonance field as well as the line shape of the signal. The non-homogeneous local magnetic moment can be understood to arise from non-uniform distribution of Fe atoms within the films and will be discussed in section 5.5 for a x=0.3 film.

In Fig. 5.8(b), the angular dependence of the in-plane resonance fields at 110 K for $CoTi_{1-x}Fe_xSb$ films is presented. The value of resonance field oscillates as a function of the angle of the applied magnetic field. Since the resonance field is proportional to the effective magnetic field, the maximum (minimum) value is found when the field is parallel to the hard (easy) axis. The angular dependence of the resonant frequency immediately shows that the easy axis is along the [110] direction, consistent with SQUID hysteresis loops. For the samples with x<0.15 (not shown), the FMR signal is very weak and there is almost no shift in resonance field with angle, confirming the absence of in-plane anisotropy as measured in SQUID. $\mathrm{CoTi}_{1-x}\mathrm{Fe}_x\mathrm{Sb}$ film with x=0.2 is dominated by a four-fold symmetry, arising from the cubic anisotropy contribution from the cubic bulk $C1_b$ structure of CoTiSb film. The increase in Fe concentration to x=0.3 induces a strong planar two-fold uniaxial anisotropy field and again a very small fourfold in-plane anisotropy field. The origin of this behavior is consistent with two different magnetic environments for Fe. While the cubic anisotropy is associated with the ferromagnetic interactions of Fe atoms in Fe-rich regions, strong uniaxial anisotropy is due to the symmetry of the substrate. This is similar to Fe grown on GaAs where uniaxial anisotropy was observed in thin Fe films [137]. The easy axis aligning along the [110] direction, has been suggested to originate from the arsenic-bond direction on the GaAs(001) surface [138]. For the $\mathrm{CoTi}_{0.5}\mathrm{Fe}_{0.5}\mathrm{Sb}$ film, the FMR signal is pronounced and an in-plane uniaxial magnetic anisotropy is observed, associated with the dipolar interactions of Fe atoms. For pure CoFeSb, cubic anisotropy is observed with the in-plane easy axes parallel to the [110] and [-110] directions. The four-fold symmetry contribution can be attributed to the bulk cubic symmetry associated with the h-H crystal structure, which for the highest magnetic moment film appears to dominate.

Figure 5.8(c) depicts the dependence of resonance field on angle with the out-of-plane configuration at 110 K. For higher Fe content films, the value of resonance field is minimum when the applied field is along the film plane and reaches maximum when along the film normal. As the Fe concentration increases, the resonance field is increased slightly at angles around film plane, while reduced significantly at low angle near the film normal. The perpendicular magnetic anisotropy can be associated with the epitaxial relationship between the film and the substrate in addition to the shape anisotropy. The large resonance field observed in the x=0.5 and x=1.0 samples along the [001] and [00-1] directions corresponds to a hard axis being out-of-plane, consistent with SQUID measurements.

5.3 Magnetotransport

The addition of Fe is expected to have a strong effect on the electronic properties. Hence, transport measurements were performed to determine the electrical properties of the series. Figure 5.9 shows the longitudinal sheet resistance for the $\mathrm{CoTi}_{1-x}\mathrm{Fe}_x\mathrm{Sb}$ thin films dependence on Fe concentration and temperature. Figure 5.9(a) highlights that both the room temperature and low temperature sheet resistance decrease with increasing Fe content, consistent with the increased electron concentration expected. From Fig 5.9(b), it can be seen that for the lower Fe alloying, the film exhibits semiconducting-like or hopping transport and thermally activated behavior. From the 1/T dependence near room temperature, activation energies of 9 meV, 7 meV, 4 meV, and 3 meV are extracted for x=0.0, 0.2, 0.3, and 0.5, respectively. As the Fe concentration increases, the temperature dependence becomes weaker until the Fe composition is greater than x=0.5, where metallic transport was observed. A high residual resistivity and thermally activated transport has been observed within other predicted half-metallic f-H compounds [139, 140] and may originate from disorder within a half-metallic system. The observed temperature dependence is consistent with previous reports of sputtered films, where thermally activated behavior was observed for films up to 37 atomic % of Fe [71].

Longitudinal magnetoresistance (MR)-H curves for the x=0.3 and x=0.5 films are shown in Fig. 5.10 for temperatures between 5 K and 300 K, where the magnetic field is perpendicular to the film plane. MR is defined as

$$MR = \frac{R_{xxH} - R_{xx0}}{R_{xx0}} \tag{5.1}$$

where R_{xxH} and R_{xx0} refer to the resistance measured with and without an ap-

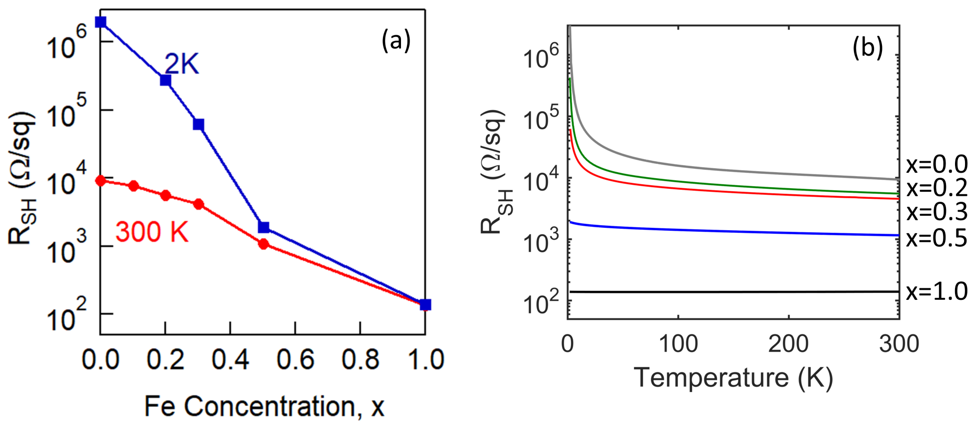

Figure 5.9. Longitudinal sheet resistance (R_{SH}) measurements for ~15 nm thick $CoTi_{1-x}Fe_xSb$ films x=0.0, 0.2, 0.3, 0.5, and 1. (a) The 2 K and 300 K R_{SH} as a function of Fe concentration and (b) R_{SH} as function of temperature. Adapted from [132] with permission from *American Physical Society.*

plied magnetic field, respectively. For the x=0.3 film (Fig. 5.10a), a negative MR, with a magnitude which monotonically increases with decreasing temperature for all field strengths, is observed. The temperature dependence of the MR at 100 kOe is displayed in the inset. Here it can be seen that the rate of increase in the MR magnitude drastically changes around 40 K. This is consistent with the temperature dependence of the magnetization shown in Fig. 5.7(a). In addition, a relatively large MR of 18.5% is observed at 100 kOe at 5 K which does not saturate within 140 kOe. This field strength is much beyond the saturation field seen in SQUID, indicating the large MR cannot be ascribed to only the magnetization of the film. This large MR can be attributed to the suppression of spin disorder within the system, which is consistent with the enhancement of spin-dependent scattering at lower temperatures. In contrast, the MR of the x=0.5 film displays a much weaker temperature dependence. Although a negative MR is observed at higher fields, a positive MR can be observed at low field. The peak in the MR corresponds to the saturation magnetization observed in SQUID and can be attributed to anisotropic MR. The magnitude and field position of the peak decrease with increasing temperature until it disappears by 300 K.

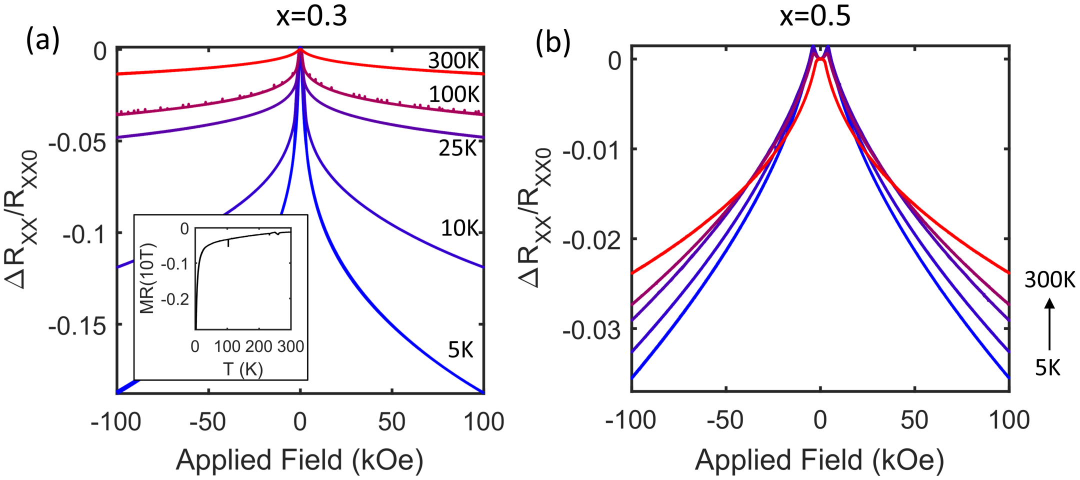

Figure 5.10. Temperature dependence of the longitudinal MR curves for (a) $\mathrm{CoTi_{0.7}Fe_{0.3}Sb}$ and (b) $\mathrm{CoTi_{0.5}Fe_{0.5}Sb}$ with the applied magnetic field out of plane for 5, 10, 25, 100, and 300 K. The MR is defined as $(R_{xxH} - R_{xx0})/(R_{xx0})$ where R_{xxH} and R_{xx0} are the longitudinal resistances measured at external magnetic field and zero magnetic field respectively. The inset of (a) shows the MR as a function of temperature at 100 kOe. Reprinted from [132] with permission from *American Physical Society*.

A large anomalous Hall effect (AHE), shown in Fig 5.11(a-b), was observed in both the x=0.3 and x=0.5 films. The Hall resistance, R_H, in magnetic materials can be expressed as,

$$R_H = (\frac{R_0}{d})B + (\frac{R_s}{d})M \tag{5.2}$$

where R_0 is the ordinary Hall coefficient, d is the sample thickness, R_s the anomalous Hall coefficient, and M the magnetization of the samples. Although the contribution of the ordinary Hall effect was small in comparison to the AHE, electron dominated transport could be observed in both samples consistent with Fe being an electron donor when occupying the Ti site. Magnetic remanence was observed at low temperature for the x=0.3 film in both the MR and AHE and is highlighted in the lower inset of Fig. 5.11(a). The magnitude of the remnant field decreases with increasing temperature and disappears by 80 K as shown in the upper inset of Fig. 5.10(a). This is consistent with the out-of-plane magnetic moment observed in SQUID magnetometry for the x=0.3 film. No remanence was observed for the x=0.5 film, confirming that the magnetic moment has no out-of-plane component.

The anomalous Hall conductivity, which is given by

$$\sigma_{AH} = \frac{\rho_{AH}}{\rho_{xx}^2 + \rho_{AH}^2} \approx \frac{\rho_{AH}}{\rho_{xx}^2} \tag{5.3}$$

where ρ_{AH} and ρ_{xx} the anomalous Hall and longitudinal resistivity respectively, exhibits a non-monotonic dependence on temperature shown in Fig.5.11(c,d). A minimum around 100 K is observed for both samples indicating a competition of skew scattering, side jump, and intrinsic mechanism (Berry curvatures) at these lower temperatures [141]. This is similar to that observed in magnetron sputtered 21 atomic % Fe alloyed CoTiSb thin films, which required the expanded scaling first introduced by Tian et al. to describe the dependence of anomalous Hall resistivity on longitudinal resistivity [142]. In the expanded scaling, the anomalous Hall resistivity is expressed as

$$\rho_{AH} = a'\rho_{xx0} + a"\rho_{xxT} + b\rho_{xxT}^2 \tag{5.4}$$

where ρ_{xx0} is the residual resistivity, ρ_{xxT} is the phonon induced resistivity, a, a, and b are related to impurity induced skew scattering, phonon induced skew scattering, and Berry curvatures, respectively. Here the residual resistivity was taken to be the resistance at 2 K. The anomalous Hall resistivity vs longitudinal resistivity curves are shown in the insets of Fig. 5.11(c.d). The contribution of skew scattering (a, a) is comparable to the intrinsic contribution ($b\rho_{xxT}$) for both the x=0.3 and x=0.5 films providing further support that the expanded scaling is necessary for CoTi$_{1-x}$Fe$_x$Sb at other concentrations of Fe. Beyond the magnitude of the coefficient increasing for the higher content film, a proportionally lower contribution of the impurity induced skew scattering can be observed for the x=0.3 film.

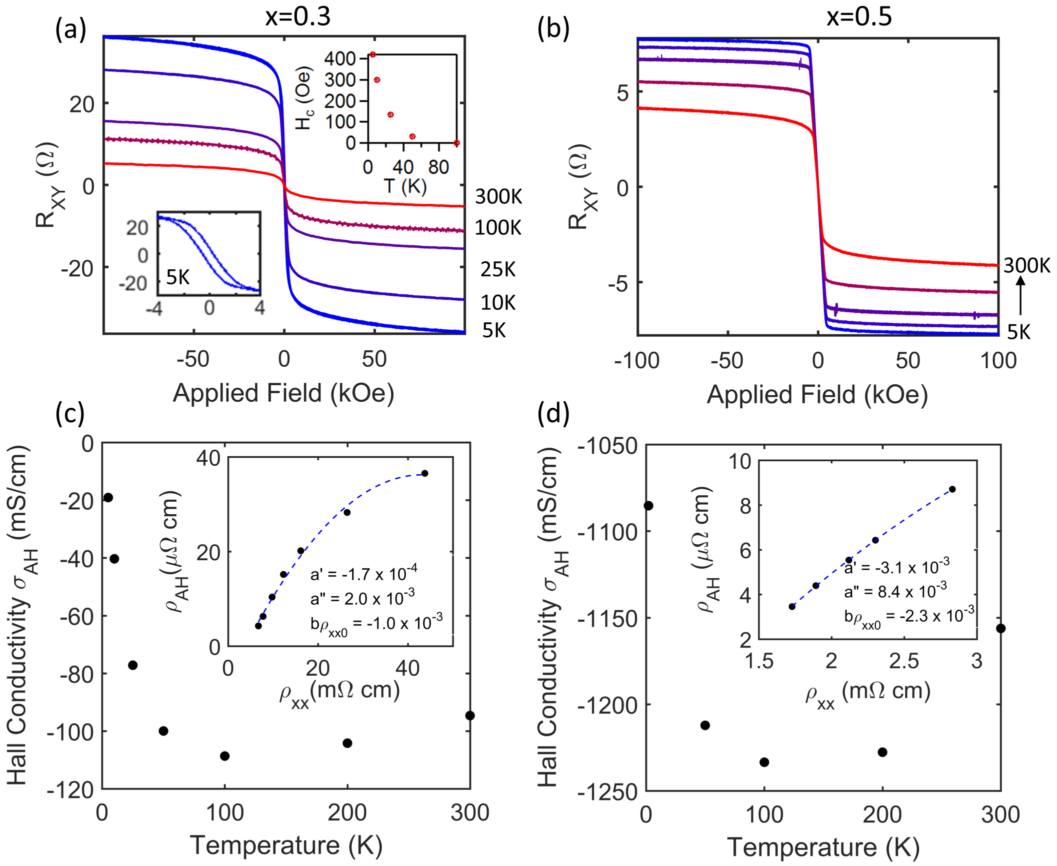

Figure 5.11. Anomalous Hall effect curves for 15 nm thick (a) $CoTi_{0.7}Fe_{0.3}Sb$ and (b) $CoTi_{0.5}Fe_{0.5}Sb$ with the applied magnetic field out of plane for 5, 10, 25, 100, and 300 K. The insets of (a) show the observed coercive field at 5K and the temperature dependence. Hall conductivity vs temperature curves for (c) $CoTi_{0.7}Fe_{0.3}Sb$ and (d) $CoTi_{0.5}Fe_{0.5}Sb$. The insets of (c) and (d) show the anomalous Hall resistivity vs longitudinal resistance curves fitted by the expanded scaling expression. Reprinted from [132] with permission from *American Physical Society*.

5.4 Evidence of Superparamagnetism

The dramatic change in the magnetic moment as well as the MR of the $CoTi_{0.7}Fe_{0.3}Sb$ around 70 K is suggestive of a phase transition. To investigate this further, additional magnetization vs temperature (M-T) curves for the x=0.2, 0.3, and 0.5 samples were obtained and are shown in Fig 12(a). For this measurement, a constant magnetic field of 300 Oe was applied along the [110] sample direction and the magnetization was measured as a function of temperature during warm-up for samples that were zero-field-cooled (ZFC) and 20 kOe field-cooled (FC), respectively. The x=0.2 and x=0.3 M-T curves in the ZFC condition exhibit a blocking phenomenon with a peak in magnetization at around 70-100K. In contrast, the x=0.5 sample shows no peak in the ZFC curve, which is consistent with normal ferromagnetic behavior. The low temperature splitting between the ZFC and FC curves seen for the x=0.2 and x=0.3 samples could originate from a ferromagnet to superparamagnet transition, which can be observed in inhomogeneous magnetic systems in which ferromagnetic clusters are distributed in a nonmagnetic matrix [143]. The blocking phenomenon observed is attributed to the freezing of the magnetization of the ferromagnetic clusters at low temperature due to their magnetic anisotropy. In Fe_2MnAl, a ZFC and FC splitting in M-T curves was attributed to antiferromagnetic pinning of ferromagnetic parts [140]. However, no evidence of an antiferromagnetic phase was observed in any of the MvT measurements.

Above the blocking temperature, a superparamagnetic material should display paramagnetic-like behavior, but with an important identifying signature. Hysteresis curves that have been corrected for the temperature dependence of the spontaneous magnetization should approximately superimpose when plotted against H/T [143]. The $CoTi_{0.7}Fe_{0.3}Sb$ sample was tested for superparamagnetism by collecting hysteresis curves at temperatures between 150 K and 400 K. Figure 5.12(b) shows the measured magnetization curves plotted as $M_s(T)/j_s = f(j_sH/T)$, where $j_s = M_s(T)/M_s(0)$ for 150 K, 300 K, 350 K, and 400 K. The inset shows the fit to the saturation magnetization which gives

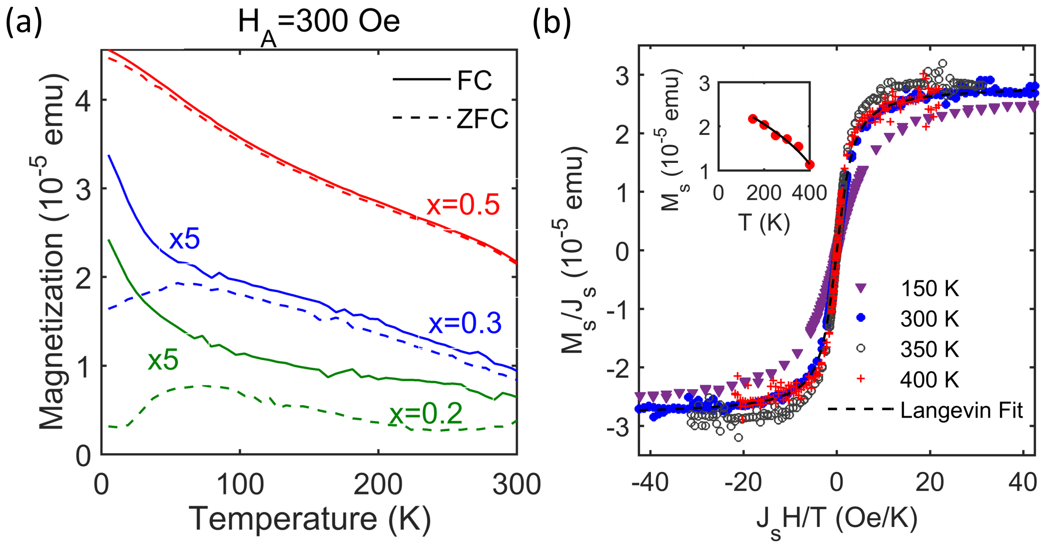

Figure 5.12. (a)Temperature dependence of the magnetization for the x=0.2, 0.3, and 0.5 samples applied field H_A=300 Oe. Curves were taken while warming up in the ZFC and FC conditions with 0 and 20 kOe applied field respectively during cool down. (b) Normalized magnetization as a function of j_sH/T at temperatures of 150, 300, 350, and 400 K for the x=0.3 sample. The dashed line is a fit of the 300 K data to the Langevin function. The inset shows the temperature dependence of the saturation magnetization and resulting fit used to determine $j_s(T)$. Reprinted from [132] with permission from *American Physical Society*.

a spontaneous magnetization Ms(0)=2.6x10^{-5} emu and a Curie temperature T_c=480 K for this sample. The normalized M vs H/T curves nearly overlay for the 300 K, 350 K, and 400 K temperatures suggesting that the transition range from the blocked to the superparamagnetic state is from ∼100 K to 300 K. During this transition the magnetic susceptibility gradually changes the slope for temperature independent (blocked state) through $1/k_BT$ (anistropic state with easy axes aligned with the external field) to $1/(3k_BT)$ (completely isotropic superparamagnetic state with magnetization described by the Langevin function). The magnetic moment of the 300 K data is fit by $M = M_sL(x)$, where $L(x)$ is the Langevin function, with $x = \mu H/k_BT$. Here it is assumed that the system is comprised of noninteracting and monodisperse particles. The simple Langevin fit results in a particle magnetic moment of $\mu \approx$6700 μ_B which corresponds to approximately 1700 Fe atoms contributing 3.9 μ_B/Fe atom.

While the M-T and M-H data are suggestive of superparamagnetism, there are no indications of non-h-H phases in the RHEED, XRD, or XPS spectra. Additionally, the magnetic moment nearly follows the expected 4 μ_B/Fe atom from Slater-Pauling for Fe occupying the Ti site in the h-H structure suggesting that Fe-Fe clusters, which would contribute closer to 2.2 μ_B/Fe atom, are not present. Thus, it can be inferred that the observed superparamagnetic behavior can be attributed to non-homogeneous distribution of the Fe atoms, leading to Fe rich h-H phase (e.g. $CoTi_{1-x-\delta}Fe_{x+\delta}Sb$), within an Fe poor semiconducting matrix ($CoTi_{1-x+\delta}Fe_{x-\delta}Sb$). This demixing was predicted for $CoTi_{1-x}Fe_xSb$ for the majority of intermediate compositions [144, 145]. While no evidence of phase separation was observed in x=0.1 bulk crystals in transmission electron microscopy [75], the expected contrast would be quite weak, even for nanoparticles of CoFeSb within a CoTiSb matrix. Moreover, x=0.1 may still be outside the region of spinodal decomposition.

5.5 Nanometer scale structural characterization

To investigate the nanometer scale distribution of Fe in the samples, atom probe tomography (APT) was performed on a x=0.3 film [146, 147]. A 130 nm thick $CoTi_{0.7}Fe_{0.3}Sb$ film was grown for the purpose of the analysis with an *in-situ* deposited Ni capping layer of ∼5 nm used to prevent oxidation. An additional 150 nm of Ni was electron-beam deposited *ex-situ* on the samples to protect the regions of interest during the APT specimen preparation. Sharp tips were prepared with a FEI Helios 600 dual beam Focused Ion Beam (FIB) instrument following standard procedure with final FIB voltage down to 2 kV to minimize Ga induced damage [148]. APT analyses were performed with a Cameca 3000X HR Local Electrode Atom Probe (LEAP) operated in voltage-pulse mode with a sample temperature of 75 K to reduce the probability of tip fracture. A pulse fraction of 25% pulse to base voltage was chosen with a detection rate set to 0.005 atoms/pulse [147]. The APT 3D reconstruction was carried out using commercial software IVASTM. The reconstruction is optimized to visualize flat atomic planes in the Z-direction with the correct corresponding distance between planes [149].

Figure 5.13(a) are 25x25x50 nm^3 3D reconstructions of the $CoTi_{0.7}Fe_{0.3}Sb$ layer showing the four different elements. The measured elemental composition by APT are 35% of Co, 31% of Sb, 24% of Ti and 10% of Fe which is in good agreement with the expected 33% of Co, 33% of Sb, 24% of Ti and 10% of Fe. The small discrepancy between the measured and expected compositions may not be materials related but could be caused by the difficulty to adjust the APT evaporation parameters in a way that all elements are correctly detected [150]. In the 3D reconstructions, Co, Sb, and Ti rich clusters could not be visually directly identified. A homogenous distribution of these elements is observed. However, Fe rich and poor regions can be directly identified on the reconstruction. A statistical analysis of the data has been carried out in order to confirm the presence of possible Fe rich phases [151, 152]. Figure 5.13(b) shows the radial distribution function (RDF) curves compared to Fe atoms. In these graphs, the ratio of the composition in shells drawn around each of the Fe atoms divided by the average composition in the sample is plotted versus the shell radius. The self-correlation curve is generated by measuring the composition of Fe (Fe-Fe) while the cross-correlation curve is generated by measuring the compositions of Co, Ti and Sb (Fe-Co, Fe-Ti and Fe-Sb). The RDF analysis of a homogeneous material would result in the self and cross-correlations curves being horizontal lines with a value of 1. This behavior is observed for the Fe-Co and Fe-Sb curves which indicates a homogenous distribution of Co and Sb around Fe atoms. However, a clear positive interaction (curve above 1) below 20 Å is found in the Fe-Fe curve showing that Fe-rich domains are present in the sample. This positive interaction corresponds to a negative interaction (curve below 1) in the Fe-Ti curve. As expected from the crystal structure of the $\mathrm{CoTi_{0.7}Fe_{0.3}Sb}$ layer, a local Fe rich domain corresponds to a local depletion in Ti, further evidence Fe and Ti occupy the same crystallographic site in the h-H crystal structure. Self-correlation and cross-correlation curves were also plotted relatively to Co, Ti and Sb centers. Positive and negative interactions were not as clearly observed as in Fig. 5.13(b) suggesting more uniform distribution across the sample for Co, Ti, and Sb.

While the APT results suggest that Fe rich regions are present, they give further evidence that Fe bonded to Fe clusters are absent. Because the cross-correlation curve with Co (Fe-Co) and Sb (Fe-Sb) are nearly flat with a value of 1, a local increase in Fe does not correspond to a local depletion of Co and Sb which would occur if clusters containing only Fe were occurring. The local increase in Fe content is accommodated by a local decrease in the Ti concentration (seen in the Fe-Ti RDF curve less than 1), maintaining the half-Heusler X:Y:Z stoichiometry of 1:1:1 for Co:Ti/Fe:Sb. The local increase in Fe content observed in the RDF curve could partially be accommodated by Fe occupying the interstitial site, but from the calculations this would lead to a drastically reduced magnetic moment from 4 μ_B/Fe atom to ∼2 μ_B/Fe atom which is not observed. Thus a significant

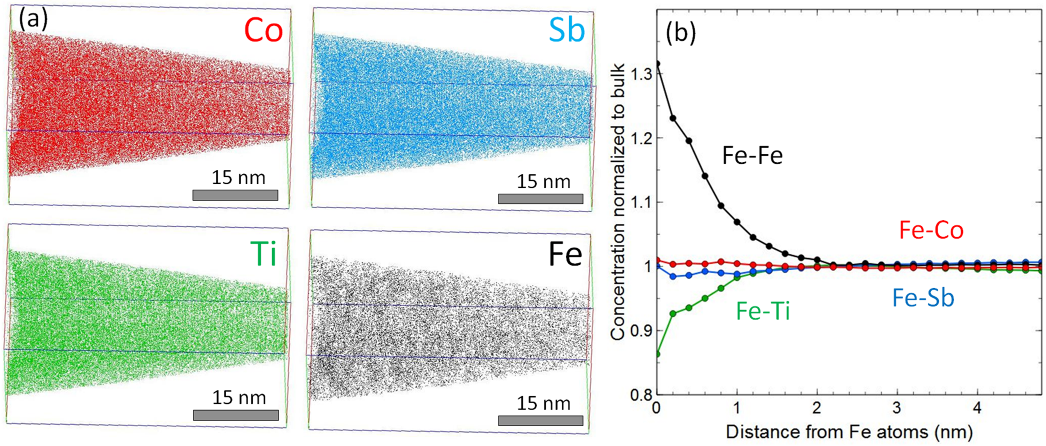

Figure 5.13. (a) Three-dimensional (3D) reconstruction of the atomic distribution from atom probe tomography performed on a x=0.3 film for Co, Ti, Fe, and Sb. The colors red, green, blue, and black correspond to Co, Ti, Sb, and Fe respectively. (b) Radial distribution function (RDF) curves for Fe-Fe, Fe-Co, Fe-Sb, and Fe-Ti. Reprinted from [132] with permission from *American Physical Society*.

number of Fe atoms occupying the interstitial site is not present.

The Fe rich domains observed in APT of a $CoTi_{0.7}Fe_{0.3}Sb$ film are consistent with the superparamagnetic behavior observed. The absence of pure nanoparticles within the film explains deviations away from traditional superparamagnetism. While APT analysis was not performed on other Fe content films, it can be expected that Fe rich regions likely exist in other composition films. The degree of Fe clustering will likely be a function of the Fe content of the film as well as the film growth/annealing temperatures. This may also partially explain the need for lower growth temperatures to achieve high quality, smooth films as determined from RHEED and XRD for higher Fe content films. Finally, the observed thermally activated behavior in the sheet resistance could be understood to originate from the non-homogenous Fe distribution that leads to a hopping-like transport instead of band transport.

5.6 Summary

In summary, epitaxial thin films of the substitutionally alloyed series $\mathrm{CoTi}_{1-x}\mathrm{Fe}_x\mathrm{Sb}$ and $\mathrm{Co}_{1-y}\mathrm{Fe}_y\mathrm{TiSb}$ were grown by MBE for concentrations $0.0 \leq x \leq 1.0$ and $0.0 \leq y \leq 0.5$. Fe concentration plays a significant role in determining the electrical and magnetic properties depending on which atomic site it substitutes. When Fe substitutes on the Ti site, the magnetic moment scales linearly with Fe content up to x=0.5 as ~ 3.9 μ_B/Fe atom with a transition from weak to strong interaction as Fe content is increased. In contrast, a drastically reduced moment of ~ 0.4 μ_B/Fe atom is observed when Fe substitutes for Co. Semiconducting-like or hopping transport can be observed for $x \leq 0.5$ with a strong anomalous Hall effect observed for the higher Fe content films that further supports the expanded scaling in the $\mathrm{CoTi}_{1-x}\mathrm{Fe}_x\mathrm{Sb}$ thin films. These tunable magnetic properties as well as simultaneous high resistance make $\mathrm{CoTi}_{1-x}\mathrm{Fe}_x\mathrm{Sb}$ thin films attractive for spintronic applications. Finally, the observed superparamagnetic behavior and APT analysis suggests Fe compositional fluctuations are present. These nano-scale compositional variations may be present in other quatenary alloyed Heusler compounds but with subtler effects. Interestingly, the compositional fluctuations, especially with higher Z elements, would likely be effective at scattering phonons, making these quatenary alloyed films a promising direction for CoTiSb based thermoelectrics.

Chapter 6

CoTiSb Band-Alignments with $In_{0.52}Al_{0.48}As$, $In_{0.53}Ga_{0.47}As$, and NiTiSn

Two of the most important interface properties in a heterostructure are the conduction and valence-band offsets [153]. These discontinuities can create barriers for carrier transport across an interface or confinement near the interface. Despite the importance of these properties, no studies to date have measured the band offsets between any half-Heusler (h-H) compound and III-V semiconductor.

In this chapter, the valence-band discontinuities in abrupt CoTiSb/$In_{0.53}Ga_{0.47}As$, CoTiSb/$In_{0.52}Al_{0.48}As$, and CoTiSb/NiTiSn heterojunctions were directly determined using X-ray photoemission spectroscopy (XPS) and then compared to the results from density functional theory (DFT) calculations. As discussed in chapter 2, the XPS method uses the energy difference of the core level (CL) to valence-band edge (VBE) as means of accurately measuring heterojunction valence-band discontinuities[93]. The valence-band offset (ΔE_v) can be observed when a thin ~1 nm overlayer of the second material is deposited on top of the first. For an incident photon energy of eV the effective photoelectron escape depth for X-rays is ∼1-2nm; thus, photoelectrons originating from both sides of the heterojunction interface can be collected.

6.1 Calculation of Band Offset

To compare with valence-band offset measurements, the band alignment of CoTiSb with GaAs, AlAs, and InAs were calculated, courtesy of Abhishek Sharan and Anderson Janotti at the University of Deleware, and then applied to predict the band alignment of CoTiSb with InGaAs and InAlAs. The binary III-V compounds, rather than the ternary alloys, were chosen to calculate the band alignment because of the complexity of simulating random alloys using finite supercells. The band alignments between the III-V alloys and the h-H material were estimated based on the calculations of the binary III-V compounds and the well-established bowing parameters. The calculations are based on DFT [119, 120, 154] with the Heyd, Scuseria, and Ernzerhof hybrid functional (HSE06) [155, 156] as implemented in the VASP code[121, 122]. The HSE06 functional is separated into short and long-range components. In the short range, it includes 25% mixing of non-local Fock exchange with 75% of semi-local exchange in the generalized gradient approximation (GGA) form of Perdew, Burke, and Ernzerhof (PBE) [157], with a screening parameter of 0.2 Å^{-1}. The correlation energy and the long-range part of the exchange are described by PBE. The interactions between the valence electrons and the ionic cores are treated using projector-augmented wave potentials [123, 124]. Energy cutoff of 350 eV has been used in the plane-wave basis set expansion. The bulk calculations are performed using 4x4x4 Monkhorst-Pack special k-points, whereas the superlattices for band alignment calculations use a 2x2x1 Monkhorst-Pack grid of special k-points in reciprocal space for integrations over the Brillouin zone. The effects of spin-orbit coupling were included in the bulk calculations.

For the band alignment calculations between CoTiSb and AlAs, GaAs, and InAs, a standard procedure was used [158]. First, separate calculations for the bulk materials were performed, where the valence-band maximum with respect to the averaged electrostatic potential was determined. Then a calculation for a superlattice to align the averaged electrostatic potentials between two of the materials was performed. A supercell consisting of 12+12 atomic layers along the [110] direction (each layer containing one atom of each species) for extracting the averaged electrostatic potential in each material was used. A test calculation using 10+10 layers for the CoTiSb/AlAs interface results in a change of less than 0.02 eV. Superlattices along the non-polar [110] direction with two equivalent interfaces were used to avoid any polar discontinuity. This procedure was carried out for all the combinations of CoTiSb and AlAs, GaAs, InAs, and NiTiSn.

6.2 XPS Measurement

Core-level spectra fitting was performed using a Gaussian-Lorentzian convolution with a linear background utilizing the CasaXPS 2.3.16 program. The VBE was fit using the intersection of the linear extrapolation of the valence-band maximum leading edge with the background. In Fig. 6.1, spectra from bulk InAlAs, InGaAs, and CoTiSb samples are shown. The Al 2p (BE=75.03 eV) and In 3d (BE=19.09 eV) CLs were used for InAlAs. The In 3d (BE=19.37) and Ga 3d (BE=21.07 eV) CLs of InGaAs were found to overlap, but could be resolved. In contrast, the Co 3p (BE=61.68 eV) and Ti 3s (BE=60.94 eV) CL binding energy positions were found to overlap too much to resolve, and thus the relative position and peak area ratio was determined from the bulk reference sample CL fitting and held fixed for the heterojunction measurements. Even though the detector resolution is 1.7 eV, the uncertainty of the CL peak position could still be fit to within 0.03 eV. The Sb 4d and As 3d CLs were not included in the calculation of the valence-band offset because both have an additional known bonding states in III-Vs[159] and h-H compounds[116] due to the surface

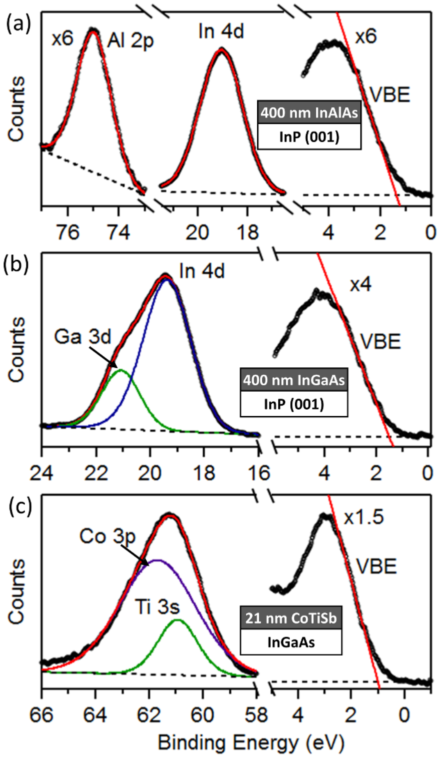

Figure 6.1. Core-levels (CLs) and valence-band edge (VBE) for (a) 400 nm-thick InAlAs, (b) 400 nm-thick InGaAs, and (c) 21 nm-thick CoTiSb. CLs were fit using a Gaussian-Lorentzian convolution with a linear background subtraction. The valance-band edge (VBE) was fit using the intersection of the linear extrapolation of the valence-band maximum leading edge with the base line. Reprinted from [130], with the permission of *AIP Publishing*.

reconstruction.

For the heterojunction spectra, ∼1 nm-thick overlayer films were deposited. The heterojunctions measured include CoTiSb/InAlAs, CoTiSb/InGaAs, and InGaAs/CoTiSb. The CLs from each of these heterojunctions are displayed in Fig. 6.2. An arsenic satellite peak (As sat) was observed overlapping with the Co 3p and Ti 3s peaks. The arsenic satellite peak position was determined relative to the As 3d CL from the bulk sample and held fixed for the heterojunction fitting. The fitted CL positions for each of the spectra are summarized in Table 6.2. Using these positions and the CL to VBE, the valence-band offset for an InAlAs/CoTiSb heterostructure can be calculated from equation:

$$\Delta E_v = \Delta E_{CL-VBM}(CoTiSb) + \Delta E_{CL} - \Delta E_{CL-VBM}(InAlAs) \tag{6.1}$$

Taking the III-V valence-band energy as the reference, a positive valence-band offset corresponds to a higher valence-band energy for CoTiSb. Values of ΔEv (CoTiSb/InAlAs) = 0.58 ± 0.08 eV, ΔEv (CoTiSb/InGaAs) = 0.30 ± 0.08 eV, and ΔEv (InGaAs/CoTiSb) = 0.29 ± 0.08 eV were obtained. The experimental uncertainty is estimated from the uncertainty in the core-level and valence-band edge fits. The results obtained for both the CoTiSb/InGaAs and the InGaAs/CoTiSb heterointerfaces give values within their experimental uncertainty, thus growth sequence does not appear to affect the valence-band discontinuity in this system. The valence-band offset inferred between InAlAs and InGaAs from these measurements is ΔEv = 0.28 eV. This is consistent with previously reported XPS measurements (0.22 eV)[160] and our measured offset of ΔEv = 0.25 eV within the experimental uncertainty. Thus, we find transitivity is satisfied for these interfaces.

Layer	Co 3p (eV)	Ti 3s (eV)	Al 3p (eV)	In 3d (eV)	Ga 3d (eV)	VBE (eV)
InAlAs			75.03	19.09		1.36 ± 0.06
InGaAs				19.37	21.07	1.55 ± 0.06
CoTiSb	61.68	60.93				1.09 ± 0.03
CoTiSb/InAlAs	61.37	60.62	75.10	19.03		
CoTiSb/InGaAs	61.51	60.76		19.03	20.76	
InGaAs/CoTiSb	61.54	60.79		19.05	20.77	

Table 6.1. Fitted core-level and valence-band edge (VBE) binding energies for InAlAs, InGaAs, and CoTiSb and their heterointerfaces.

The DFT calculated lattice parameters of CoTiSb, GaAs, InAs and AlAs are 5.79 Å, 5.67 Å, 6.11 Å, and 5.68 Å respectively. For CoTiSb, an indirect band gap of 1.45 eV, with the valence-band maximum at Γ and the conduction-band minimum at X is found. The predicted band gap in HSE06 is higher than previously reported values of 1.05 eV[20]. These reports were based on DFT within the generalized gradient approximation (GGA), which is well known to

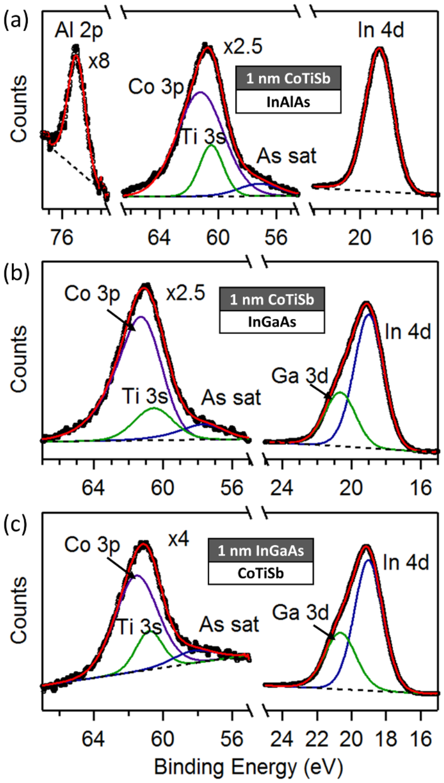

Figure 6.2. XPS spectra showing the core-levels (CLs) and their Gaussian-Lorentzian fits for (a) 1 nm-thick CoTiSb on InAlAs, (b) 1 nm-thick CoTiSb on InGaAs, and (c) 1 nm-thick InGaAs layer on CoTiSb. The sample structures of the layers measured are shown in the insets. Reprinted from [130], with the permission of *AIP Publishing*.

underestimate band gaps of semiconductors. HSE06 has been successful in predicting band gaps of many semiconductors[161, 162], and recently HSE was used to calculate the expected defects and predict the origin of the carrier type and concentrations in a number of 18 valence electron h-H compounds, finding good agreement with their predictions and what has been experimentally observed[74]. Therefore, the HSE06 predicted band gap may be closer to the true band gap of CoTiSb. The band gap separates occupied states derived from Co d (valence band) from unoccupied states derived from Ti d orbitals (conduction band). In the case of the III-Vs discussed here, GaAs and InAs are direct band gap semiconductors and AlAs is an indirect band gap semiconductor.

6.2.1 Band Alignments of CoTiSb with III-V compounds

The calculated band alignments of the four semiconductors are shown in Fig. 7.9. Type-II band alignments between CoTiSb and III-Vs are found with valence-band offsets (ΔE_v) of 0.92 eV, 0.45 eV, and 0.20 eV between CoTiSb/AlAs, CoTiSb/GaAs and CoTiSb/InAs, respectively. Using these values and bowing parameters of 0.40 eV for InGaAs [163] and 0.72 eV for InAlAs [101], applied to the conduction band [101], the band alignment of CoTiSb with InGaAs and InAlAs was calculated. Type-II band alignment was obtained in both the cases, CoTiSb/InGaAs and CoTiSb/InAlAs, as shown in Fig 7.9b, with the ΔE_v of 0.32 eV for CoTiSb/InGaAs and 0.55 eV for CoTiSb/InAlAs, respectively. The experimentally determined valence-band offsets are included in brackets showing good agreement between theory and experiment.

Conduction-band offsets can be estimated with the assistance of measured or calculated band gaps (E_g). The band gaps of InAlAs and InGaAs are well established, but large disagreement on the experimental band gap of CoTiSb remains within the literature. While the band gap values suggested from thermally activated transport (> 0.13 eV)[58] and thermoelectric transport (0.57 eV)[62] are significantly lower than that calculated by DFT, a greater than 1 eV band

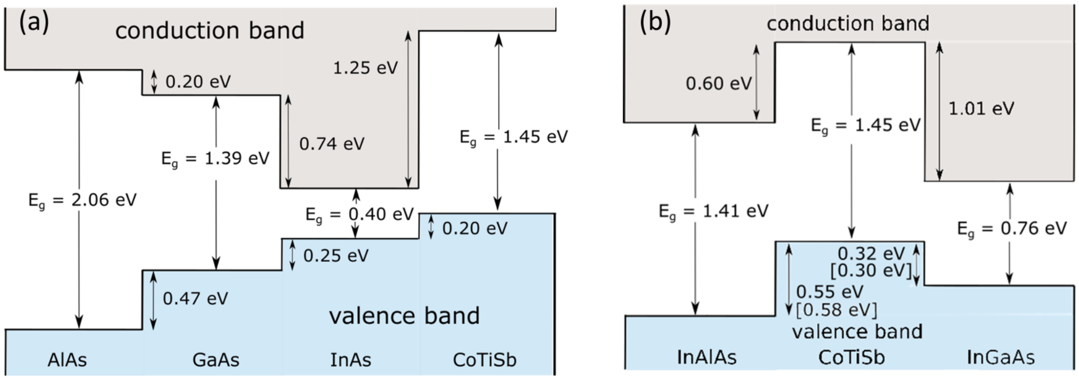

Figure 6.3. Calculated band alignments between (a) AlAs, GaAs, InAs, and CoTiSb and (b) InAlAs, CoTiSb, and InGaAs, courtesy of A. Sharan and A. Janotti at the University of Delaware. The experimentally determined offsets are included given within brackets. Reprinted from [130], with the permission of *AIP Publishing*.

gap can be estimated from spectroscopic ellipsometry and hard X-ray photoelectron spectroscopy[76]. In addition, recent scanning tunneling spectroscopy and angle-resolved photoemission spectroscopy measurements of MBE grown films suggest the band gap of CoTiSb is greater than 0.6 eV[60]. In each of these experiments the inferred band gap is sensitive to both the sample preparation as well as the measurement technique. By minimizing in-gap states formed by antisite and off-stoichiometry defects which reduce the effective band gap[164], a band gap larger than 1 eV may be expected. For a band gap greater than 0.9 eV (0.4 eV), CoTiSb is expected to have a type-II band alignment with InAlAs (InGaAs). However, if CoTiSb would have a smaller band gap, then a type-I band alignment may be possible. Studies directly probing the conduction-band offsets are necessary to accurately establish the full band alignment and will be discussed in Chapter 7.

6.2.2 Band Alignment of CoTiSb with NiTiSn

While integration of h-H compounds with existing III-V technologies will unlock a number of new and novel device structures, the great appeal of Heusler compounds will be the integration of Heusler alloys with other Heusler compounds. Therefore understanding how these compounds interact, and in particular, the properties that emerge at their interfaces will be of paramount importance. To this end, the valence-band offset between semiconducting h-H compounds CoTiSb and NiTiSn were determined by XPS and compared to that expected from DFT.

For the determination of the band offsets, two heterojunctions were formed: 1) CoTiSb/NiTiSn and 2) NiTiSn/CoTiSb. For the first heterojunction, CoTiSb on NiTiSn, a 20 nm thick NiTiSn layer was grown on an MgO substrate at 350°C following the growth procedure outlined in Kawasaki et al. [165]. Following measurement of the bulk NiTiSn spectra, a thin, 2 unit cell (1.2 nm) thick CoTiSb layer was deposited at 350°C and the spectra measured. Finally, a thick CoTiSb (25 nm) layer was overgrown, and the XPS spectra obtained. For the second heterojunction, NiTiSn on CoTiSb, a 25 nm thick CoTiSb layer on InAlAs was used for the bulk CoTiSb spectra, a 2 unit cell (1.2 nm) NiTiSn layer for the thin spectra, and 25 nm overgrown NiTiSn layer for the final NiTiSn bulk spectra. A growth temperature of 350°C was used for all growths except the seed layer of CoTiSb on InAlAs.

In Fig. 6.4(a) the XPS spectra for a 20 nm thick NiTiSn, 1.2 nm thick CoTiSb on NiTiSn, and 25 nm thick CoTiSb are shown. The Ni 3p, Co 3p, and Ti 3s were used for the determination of the valence band offsets. Also visible in the spectra are lower binding energy peaks Sn 4d, Sb 4d, and Ti 3p. Similar to CoTiSb with the III-V compounds, these p-block elements were not included in the fit because of the known additional bonding state due to the surface reconstructions in h-H compounds [116]. No additional peaks beyond those expected were observed. While a charge neutralizer (flood gun) was used, significant charging is visible in the spectra, causing a $\sim$3 eV shift in the spectra to higher binding energies for the layers grown on MgO. This same charging effect was not observed on the layers grown on InAlAs buffer layers grown on InP substrates. Consistent with previous work by A. Rice [166], where it was shown that minimal intermixing between the compounds occurs, no signal from

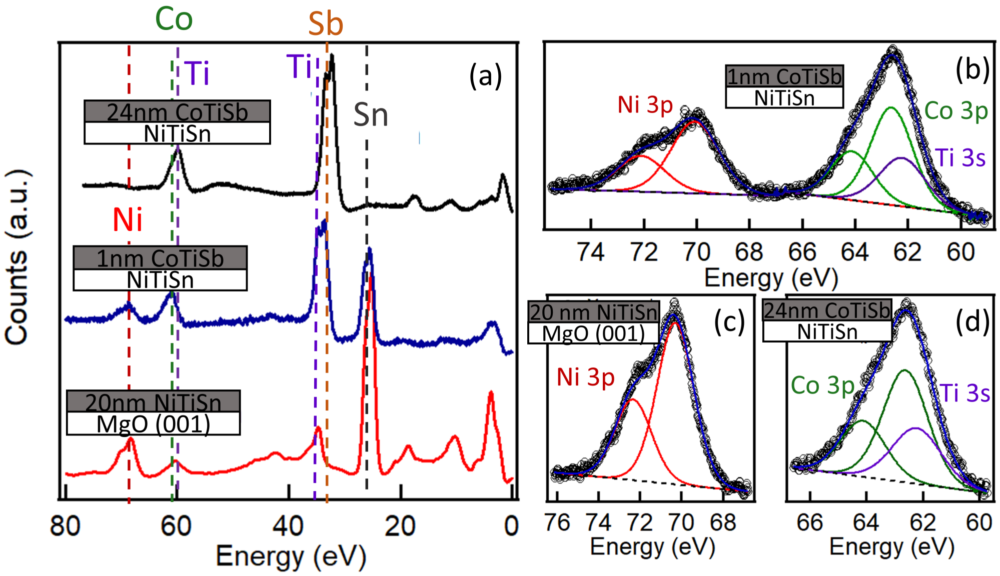

Figure 6.4. (a) XPS spectra for 20nm thick NiTiSn, 1 nm of CoTiSb on NiTiSn, and 25nm thick CoTiSb. Ni 3p, Co 3p, and Ti 3s CLs and their respective Gaussian-Lorentzian fits for the (b) 1 nm thick CoTiSb on NiTiSn, (c) 20 nm thick NiTiSn, and (d) 25 nm thick CoTiSb.

Ni or Sn is visible in the thick CoTiSb sample. For the thin CoTiSb layer fitting, because Ti is present in both compounds, the area ratio between Co 3p and Ti 3s was not held fixed. The CL fits for the thin CoTiSb, as well as the bulk CoTiSb and NiTiSn layers are shown in Fig. 6.4(b-d). The measured CLs are well fit using doublet split peak fits for the 3p peaks with the area ratio held fix at 1:2. The two component separation was determined in the bulk fitting and held fixed for the thin layer fit.

The fitted CL positions for each of the spectra are summarized in Table 6.2. The CL position of the larger, lower energy doublet peak is the value reported. Using these positions and the CL to VBE, the valence-band offset for each heterojunction can be calculated similar to that presented in Eq 6.1. Taking CoTiSb valence-band energy as the reference, a positive valence-band offset corresponds to a higher valence-band energy for NiTiSn. Values of ΔEv (CoTiSb/NiTiSn) $= 0.13 \pm 0.10$ eV and ΔEv (NiTiSn/CoTiSb) $= 0.20 \pm 0.08$ eV were obtained. The values obtained for the two heterointerfaces agree within the

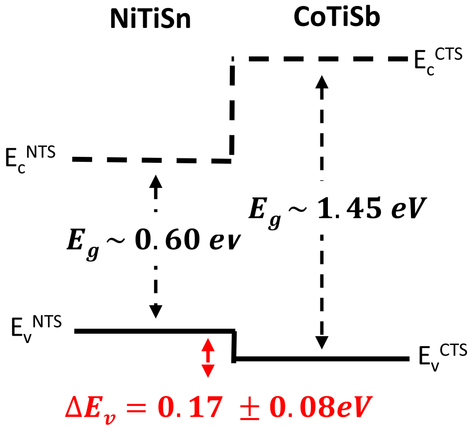

Figure 6.5. Schematic diagram of the band alignment of CoTiSb with NiTiSn with the valence-band offsets from those determined by XPS, and the band gaps estimated from DFT using the HSE approximation.

experimental error, suggesting that growth sequence does not affect the values. In addition, these are in good agreement with those calculated from DFT, where an offset of ΔEv (NiTiSn/CoTiSb) = 0.20 eV is expected[1]. The band alignment expected of CoTiSb with NiTiSn is schematically shown in Fig. 6.5. Here we can see a type I heterojunction would be expected with the conduction and valence bands of CoTiSb straddling those of NiTiSn, similar to that seen in AlAs and GaAs. Thus similar band engineering may be possible for CoTiSb and NiTiSn to form 2 dimensional transport at the interface. Devices based on this will be explored in chapter 7.

6.3 Summary

In summary, the valence-band offsets between epitaxially grown h-H CoTiSb thin films and the lattice-matched III-V compounds, InAlAs and InGaAs as well as the h-H compound, NiTiSn, have been determined using XPS. The valence-band offsets were determined to be 0.58 eV, 0.30 eV, and 0.17 eV with InAlAs,

---

[1] DFT calculations courtesy of A. Sharan and A. Janotti at the University of Delaware

Layer	Co 3p (eV)	Ti 3s (eV)	Ni 3p (eV)	VBE (eV)
CoTiSb (MgO)	63.19			3.71±0.09
NiTiSn (MgO)		62.46	70.31	3.27±0.07
CoTiSb (InP)	59.76	59.70		0.01±0.05
NiTiSn (InP)		59.14	67.04	-0.30±0.04
CoTiSb/NiTiSn	62.63	62.22	70.08	
NiTiSn/CoTiSb	59.84	59.73	67.22	

Table 6.2. Fitted core-level and valence-band edge (VBE) binding energies for CoTiSb and NiTiSn layers and their heterointerfaces. The substrate used for the layer is included in parentheses.

InGaAs, and NiTiSn, respectively. Good agreement was found with HSE06 hybrid functional calculations for band alignments. Type-II band alignments are expected for CoTiSb with both InAlAs and InGaAs, while a type-I band alignment is expected with NiTiSn. Furthermore, the growth sequence of the interface between CoTiSb and InGaAs as well as CoTiSb with NiTiSn does not appear to affect the band offsets within the experimental error. These results suggest that the theoretical approach may be applicable to other Heusler/III-V and potentially Heusler/Heusler interfaces. By using knowledge of these offsets, device structures should be able to be designed and grown that show transport properties dictated by these interfacial properties. In particular, a 2 dimensional electron gas may be present at the interface of CoTiSb and NiTiSn. These interface properties and the resulting transport properties will be explored further in Chapter 7.

Chapter 7

Electrical characterization of CoTiSb based Heterostructures

In the preceding chapters the electronic, optical, and magnetic properties of the semiconducting half-Heusler CoTiSb as well as the tunability of these properties have been explored. While a good understanding of CoTiSb, its related alloys, and other Heusler compounds are paramount to the integration of Heusler alloys into functional devices, the actual device properties must be explored. Defects and other interface effects will greatly change the observed properties compared to what theory might predict. In this chapter, the device electrical properties of a number of CoTiSb based heterostructures are examined. First, CoTiSb and III/V based diode heterostructures are grown and characterized, and the resulting electrical properties are compared to that expected from the band offsets measured previously. For this study, four heterostructures are grown, fabricated, and measured, each containing an unintentionally doped CoTiSb (intrinsically n-type) layer. The four structures include CoTiSb with 1) n-type InGaAs, 2) p-type InGaAs, 3) n-type InAlAs, and 4) p-type InAlAs.

Second, $Co_{0.7}Fe_{0.3}Sb$/CoTiSb/$CoTi_{0.7}Fe_{0.3}Sb$ giant magnetoresistance (GMR) multilayer structures are grown and the magnetic and preliminary electronic characteristics measured. These device structures are an interesting direction for a number of reasons. Currently, state of the art magnetic tunnel junctions (MTJs) generally utilize a MgO tunnel barrier sandwiched between CoFeB electrodes. However, utilizing an alternative interlayer such as CoTiSb instead of MgO may offer a few advantages. The RA product, where R is the resistance and A is the area of the device, of MgO based devices would be expected to be orders of magnitude higher than CoTiSb based device. As device sizes shrink, the resistance of the devices would lead to excessive heating and lower efficiency. Thus a lower resistance interlayer, such as CoTiSb could drastically reduce the observed resistance. Another large drawback of MgO is the reactivity of oxygen with the electrode material [167]. The high tendency of the intermetallic elements to oxidize at the interface reduces the spin-polarization of the electrode at the interface. Thus eliminating MgO from the structure may greatly enhance the observed tunneling properties. In addition, the predicted half-metallicity in $\mathrm{CoTi}_{1-x}\mathrm{Fe}_x\mathrm{Sb}$ films suggest they may be attractive choice for an electrode of a MTJ device.

Third, CoTiSb/NiTiSn heterostructures are grown and the resulting transport properties are measured. Previous work by A. Rice [168] showed anamolous transport at this interface which is explored in more depth here.

7.1 Fabrication

To minimize the challenges introduced by a complicated fabrication process, a simple mask and fabrication process was chosen for the n-n and p-n diode structures (schematically shown in Fig. 7.1). A simple wet etch process was chosen to minimize side wall leakage due to damage induced by more aggressive dry etchants. In contrast, a more developed but complicated process was necessary for the GMR structures (schematically shown in Fig. 7.2). This process was originally developed for $\mathrm{Co_2MnSi}$ MTJs and is described in detail in the dissertation of Anthony McFadden [169].

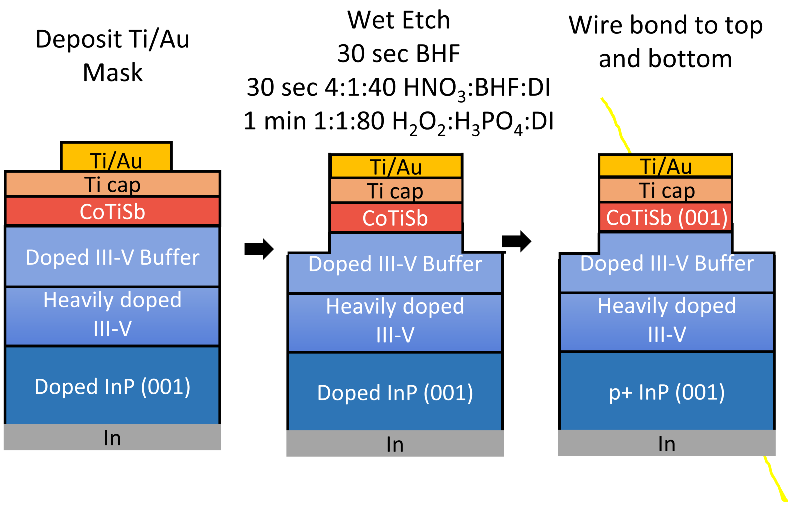

Figure 7.1. Schematic diagram of the fabrication process flow for diodes using a simple gold hard mask and wet etch process.

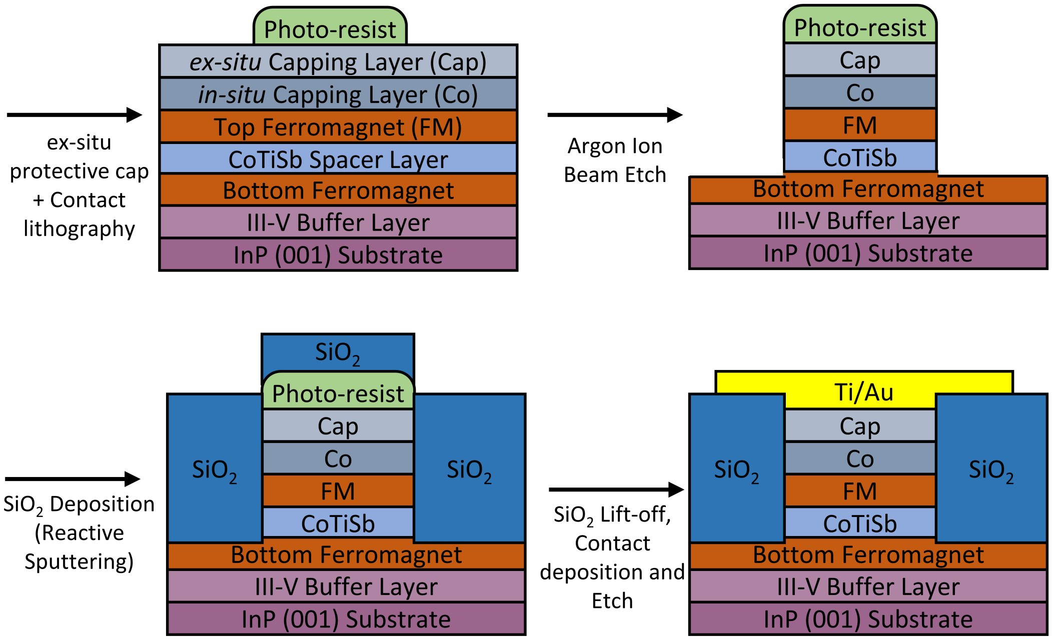

Figure 7.2. Schematic diagram of the *ex-situ* self-aligned GMR process. Adapted from [169] with permission from A. McFadden.

For the n-n and p-n structures, prior to removing from vacuum, a 5 nm thick titanium capping layer was deposited *in situ* from a standard effusion cell with the substrate at room temperature. 100 μm to 2 mm diameter mesas were patterned using standard positive photolithography with an MJB3 contact aligner. An *ex-situ* e-beam evaporated 5 nm thick titanium adhesion layer and 300-500 nm thick gold layer were used to make contact to the CoTiSb as well as define a mask for etching. The diodes were wet etched using buffered HF (BHF), 4:1:50 HNO_3:BHF:H_2O, and 1:1:80 H_2O_2:H_3PO_4: H_2O solutions for the titanium, CoTiSb, and III-V layers respectively. The III-V was etched approximately 100 nm. Etch depths were determined using dektak measurements before and after wet etching. Figure 7.3(a) shows an optical micrograph of a the final etched diode mesas. Gold wire was ball bonded to the gold layer of the mesas to make contact to the top of the diodes. Soldered indium was used to make contact to the indium on the backside of the InP(001) substrate for the ground contact. Temperature dependent vertical transport I-V measurements of the n-n and n-p structures were performed in a He-4 cryostat.

For the GMR multilayer structures, a simple stack consisting of a thin (3 nm and 5 nm thick) $Co_{0.7}Fe_{0.3}Sb$ top electrode was spaced by a 5-10 nm thick CoTiSb layer from a 20 nm thick $Co_{0.7}Fe_{0.3}Sb$ bottom electrode. A 5 nm Co layer was deposited *in situ* as a protective cap as well as an antiferromagnetic pinning layer as CoO is antiferromagnetic with a Neel temperature of $\sim$293K. For device fabrication, a self-aligned process originally developed for Co_2MnSi based MTJs [169] was used for the GMR stacks. 2.5x5μm^2 to 25x50μm^2 devices were patterned using standard positive photolithography. Ar ion milling was used to etch the mesas. Following ion-beam etching, a SiO_2 isolation layer was deposited using reactive RF magnetron sputtering from a Si target in the presence of a mixture of Ar and O_2 gas. Following lift-off of the mesa/via PR layer, Ti/Au contacts were deposited by e-beam evaporation. Figure 7.3(b) shows an optical micrograph of a finished 25x50μm^2 device. Gold wire was ball bonded to the mesas and ground contact. Temperature dependent I-V and dI/dV measurements were performed in a He-4 cryostat.

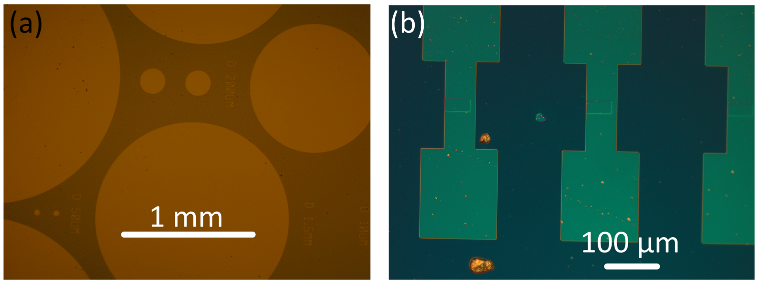

Figure 7.3. Optical micrographs of (a) etched diode mesas and (b) GMR multilayer devices.

For in-plane electrical transport measurements, the CoTiSb/NiTiSn heterostructures were patterned into a L-shaped Hall bar geometry of length 1mm (longitudinal voltage leads were spaced 200 μm apart and 150 μm wide) with the channels aligned along the [110] and [-110] directions using contact lithography and etched using Ar ion milling. Soldered indium with gold wires was used to make contact to the devices.

7.2 Diode Characterization

A number of methods to measure conduction band offsets and Schottky barrier heights using all electrical measurements exist, including (1) current-voltage, (2) activation-energy, and (3) capacitance-voltage measurements. In the current-voltage method the I-V curve of a forward biased diode is given by

$$J = A^{**}T^2 exp(-\frac{q\phi_{B0}}{kT})exp[\frac{q(\Delta\phi + V)}{kT}] \tag{7.1}$$

where J is the current density, A^{**} is the Richardson's constant, ϕ_{B0} is the barrier, and $\Delta\phi$ is the image-force lowering. The forward biased J-V characteristics are represented by:

$$J = J_0 exp(\frac{qV}{nkT}) \tag{7.2}$$

where J_0 is the saturation current density and n is the ideality factor. By fitting the linear region of the log of forward bias current, the barrier height can be estimated. This estimate depends on A^{**} and T, the first of which is not well established for CoTiSb and may vary significantly from the accepted value of 120 A/cm^2-K^2 due to defects at the interface, sidewall conduction, and the area of the diode not being representative of the electrically active region. An effective way to avoid having to make any assumptions about the active area is to use the activation energy measurement. This allows the investigation of unusual or unknown interfaces where the true value of the contact area may be unknown.

If Eq. 7.1 and Eq. 7.2 are multipled by A, the electrically active area, and rearranged we obtain

$$ln(\frac{I_F}{T^2}) = ln(AA^{**}) - (\frac{q\phi_B}{kT}) \tag{7.3}$$

where $q\phi_B$ is the activation energy. Thus the slope of $ln(I_F/T^2)$ verses $1/T$ yields the barrier height and the intercept at $1/T$=0 gives the product of the electrically active are A and the effective Richardson constant A^{**}. This plot is commonly referred to as a Richardson plot. While these plots are commonly used to extract Schottky barrier heights, any thermionic emission type transport will give a barrier height using this method. Idealities near 1 are a good indicator that the model is a good approximation. Deviations away imply multiple transport mechanisms may be present.

7.2.1 CoTiSb/InGaAs Heterojunctions

From chapter 6, a valence band offset of ΔE_v=0.30 eV is expected between CoTiSb and InGaAs. If CoTiSb has a bandgap larger than ~0.45 eV then a type II band alignment would be expected. Because CoTiSb is n-type, an n-n heterojunction between CoTiSb and InGaAs may give insights into the conduction band offset between the two materials. The device structure depicted in Fig. 7.4(a) with a 20 nm thick CoTiSb layer grown on 400 nm thick n-type InGaAs with a doping density of 3x10^{17} Si/cm^3 grown on highly-doped InP (001) was grown, fabricated, and the current-voltage (I-V) characteristics measured.

The J-V characteristics of a 100 μm diameter diode is shown Fig. 7.4(b). At room temperature linear I-Vs were observed indicative of Ohmic behavior with a resistance on the order of the contact leads (<1 Ω). As the device was cooled to 2K, an increase in resistance as well as a slight deviation away from linearity was observed. These deviations from Ohmic behavior indicate that a barrier to electron transport is present, but is likely smaller than 0.05 eV. At these lower temperatures, tunneling or field emission likely dominates the electron transport of the diodes. The inferred barrier is much smaller than the Schottky barrier heights observed in Al, Ni, Ti, Pt, and Pd contacts on n-InGaAs which ranged from 0.2 eV to 0.32 eV [170, 171]. If the conduction band of CoTiSb is above InGaAs, the observed barrier may be much smaller than the actual conduction band offset because in-gap or defect states in the CoTiSb may increase the tunneling or field-emission current through the CoTiSb layer. While a 4 point measurement was used, only 1 contact could be made to the top of the device due to the size of the device. The second top contact was connected on the chip carrier DIP. Smaller devices may enable better determination of the I-V characterisitics of these n-n structures. In addition, a lower doping in the InGaAs layer would also decrease the conductivity and possibly make the barrier more pronounced.

A CoTiSb on p-type InGaAs heterojunction was also grown. The p-InGaAs was grown with 400 nm thick Be doped layer (a doping of $\sim 1.5\times10^{17}$ Be/cm^3) with a 80 nm graded doping profile to 2×10^{18} Be/cm^3 on highly doped p-type InP(001) substrate. The sample structure is shown in Fig. 7.5(a). Here a n-p structure is expected. Fig. 7.5(b) shows J-V curves for 500 μm, 1 mm, 1.5mm, and 2 mm diameter devices. Clear rectification can be observed for all diameters. The devices show comparable current densities suggesting the majority of the transport is through the bulk of the diode. In forward bias a clear exponential dependence can be observed consistent with a diodelike transport. In Fig. 7.5(c) the temperature dependence of the J-V curve of a 500 μm diameter diode is shown. As the device is cooled the J-V curves shift toward higher bias. In Fig. 7.5(d) the temperature dependence of forward bias near room temperature is

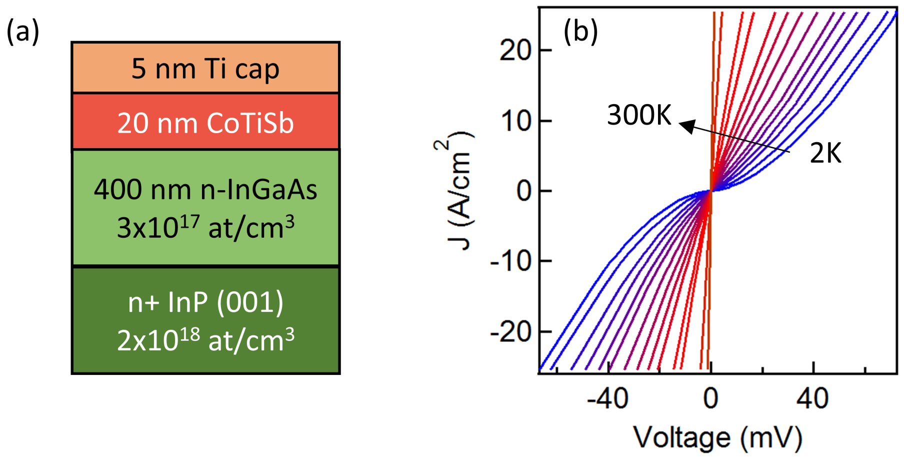

Figure 7.4. (a) Sample structure with doping profile of a 20 nm thick CoTiSb on n-type InGaAs/InP(001). (b) Current density versus voltage characteristics for temperatures between 2 K and 300K for a 100 μm diameter diode. Room temperature displays Ohmic behavior with small deviations away at low-temperature.

plotted. The saturation current density and ideality factor were determined from the intercept and slope of the semilogarithmic J-V plot. Here idealities between 1.0 and 1.2 were observed within this temperature range, indicating thermionic emission is dominating in forward bias. A Richardson plot was constructed, shown in the inset, which gave an effective barrier height of ϕ_B=0.36 eV and Richardson constant of A**=0.97 A cm^{-2}. The measured barrier height is only slightly larger than the ΔE_v expected from the valence band offsets (ΔE_v=0.30 eV) suggesting that hole transport is dominating. The measured barrier height is similar to some reported metal Schottky barrier heights which range from under 0.2 eV for Ti [172] to as much as 0.62 eV for Al [173]. Although the observed behavior is consistent with the measured valence-band offset, CoTiSb behaving more like a Schottky barrier to p-InGaAs cannot be ruled out.

7.2.2 CoTiSb/InAlAs Heterojunctions

To investigate the CoTiSb/InAlAs interface, again two heterostructures were grown, one on n-type InAlAs to examine the conduction band offset, and one

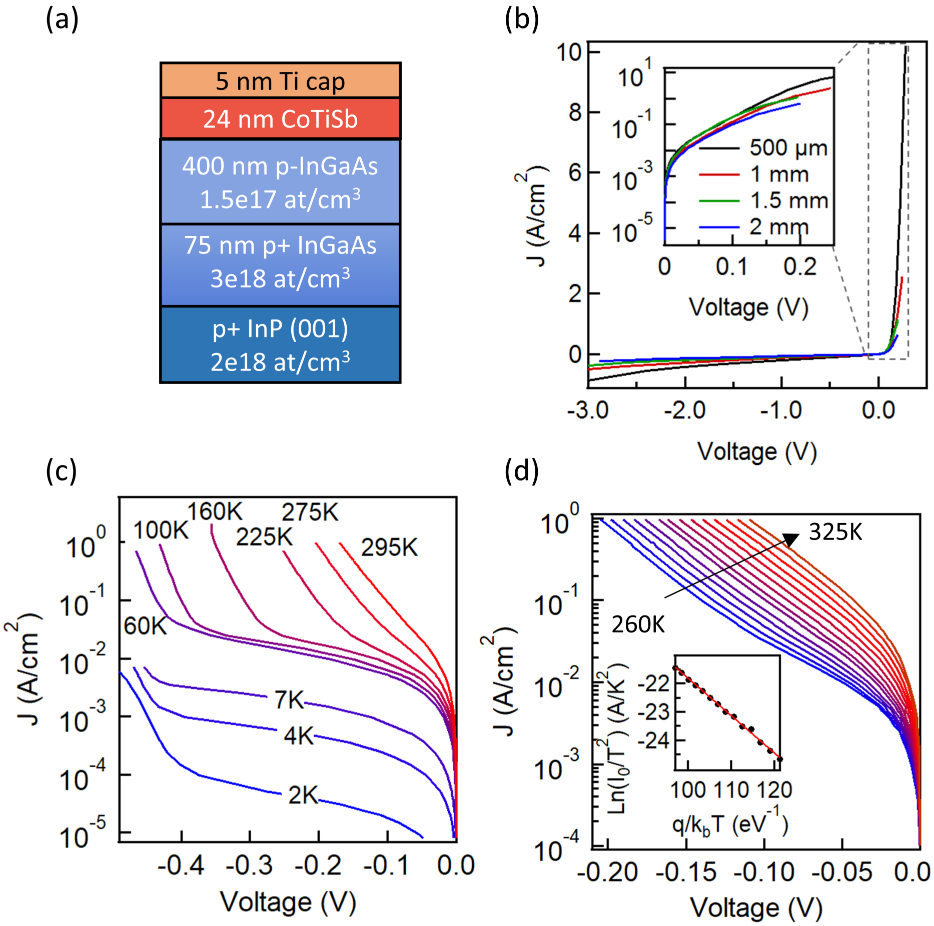

Figure 7.5. (a) Sample structure with doping profile of a 24 nm thick CoTiSb on p-type InGaAs/InP(001). (b) Current density versus voltage characteristics for 500 μm, 1 mm, 1.5 mm, and 2 mm diodes on a linear scale. The inset shows forward bias on a log scale. (c) Temperature dependence of the current density versus voltage for a 500 μm wide diode between 2 K and 295 K. (d) Near room temperature J-V characteristics betwen 260 K and 325 K. The inset shows the extracted saturation current over T^2 plotted against q/k_BT, giving an effective barrier height of ϕ_B=0.36 eV.

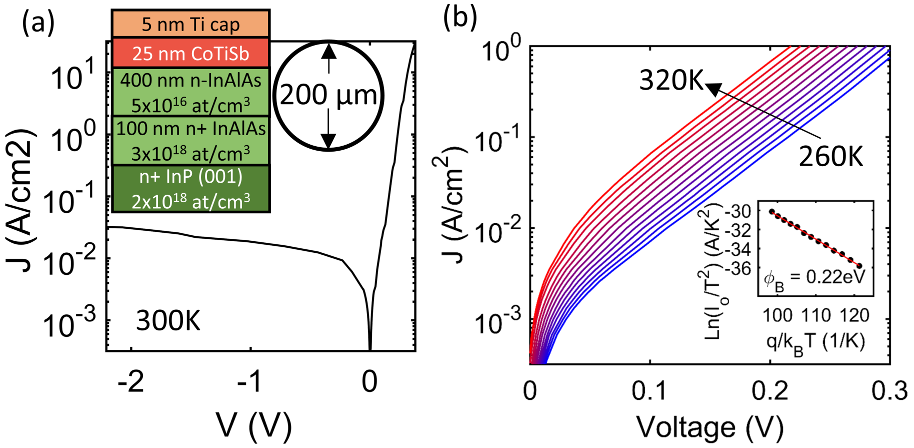

Figure 7.6. (a) J-V charactersistices of a 500 μm diode for a 25 nm thick CoTiSb layer on n-type InAlAs/InP(001). The sample structure with doping profile is shown as an inset. (b) Near room temperature J-V characteristics betwen 260 K and 325 K. The inset shows the extracted saturation current over T^2 plotted against q/k_BT, giving an effective barrier height of ϕ_B=0.22 eV.

on p-type InAlAs to probe the valence band offset. Both the n-type and p-type InAlAs were grown with a doping of ~5x10^{16} at/cm^3 with Si and Be respectively with a graded buffer on highly doped InP(001) substrates. Fig. 7.6(a) shows a semilog plot of J-V characteristics of a 200 μm diameter device. Clear rectification can be observed suggesting the presence of a barrier. The forward bias curves (shown in Fig. 7.6b) were again fit as a function of temperature between 260 K and 320K where idealities near 1 were observed. From the Richardson plot an effective barrier height of ϕ_B=0.22 eV is extracted. This suggests the conduction band offset between CoTiSb and InAlAs is approximately 0.22 eV, with the conduction band of InAlAs lying above CoTiSb. Unfortunately, without a good estimate of the doping level in CoTiSb, and therefore the energy spacing between the conduction band in CoTiSb and the Fermi level, a more accurate estimate adjusting for this is not possible.

Fig. 7.7(a) shows a J-V curve for 500 μm diameter diode of CoTiSb on p-InAlAs. Again strong rectification can be observed. Here the sign reversal of the voltage dependence is consistent with hole transport. In Fig. 7.7(b) the near room temperature J-V curves are plotted. From the fits an effective barrier

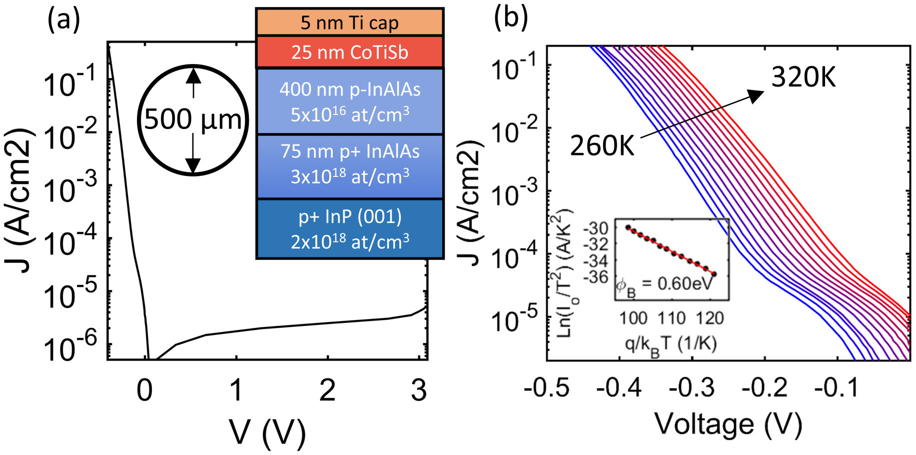

Figure 7.7. (a) J-V charactersistices of a 500 μm diode for a 25nm thick CoTiSb layer on n-type InAlAs/InP(001). The sample structure with doping profile is shown as an inset. (b) Near room temperature J-V characteristics betwen 260 K and 325 K. The inset shows the extracted saturation current, I_o, divided by T^2 plotted against q/k_BT, giving an effective barrier height of ϕ_B=0.60 eV.

height of ϕ_B=0.60 eV can be estimated. Similar to that observed with p-InGaAs, the barrier height extracted is similar to the valence band offset measured in XPS (ΔE$_v$=0.58 eV) again suggesting hole transport is dominating.

7.2.3 Refined Band Alignments from Heterojunctions

From the observed transport behavior in these four devices one can build a better description of the band alignments within the InAlAs/CoTiSb/InGaAs system. As discussed previously, the carrier concentration within CoTiSb depends strongly on composition and, in particular, any defects present. Because of the challenges introduced by matching three elemental fluxes, variations in the atomic flux ratios of ~1-2% between growths are not unexpected. If CoTiSb has a carrier concentration >>10^{17}cm^{-3}, we would expect the Fermi level to lie in the conduction band or within an impurity band acting effectively as the conduction band. If CoTiSb was behaving more like a bad metal than a semiconductor then the barrier heights observed with InAlAs and InGaAs should be similar to what is observed with metals. However this is not what we observe. Schottky barrier heights of 0.56 to 0.73 eV and 0.72 to 0.91 eV were reported for n-type and p-type InAlAs, respectively [174]. The barrier heights measured here are substantially lower than these reported values. Thus an alternative explanation is needed.

The observation that the barrier height of the CoTiSb layer with the p-type III-V material is only slightly larger than the valence-band offset measured by XPS suggests that the Fermi level of the CoTiSb is near the valence band edge rather than the conduction band edge. If the effective bandgap of CoTiSb was only a few meV this would be plausible. However, the observation of a relatively small barrier with n-type InAlAs (ϕ_B=0.22 eV) indicates this is not the case. An alternative explanation would be a relatively low carrier concentration within the CoTiSb layer ($\leq 10^{17}$ e^-/cm^3) that allows the Fermi level to effectively float from near the conduction band edge to near the valence band edge depending on what material, and in particular its carrier concentration as well as type, the CoTiSb is in contact with. Because the CoTiSb is relatively thin, the band bending is not able to change the Fermi level position relative to the band-edges significantly.

To demonstrate this, the band structures of each of the four heterojunctions was calculated using a 1D Poisson solver. The carrier concentration and bandgap of the CoTiSb layer were used as adjustable parameters to match the bandstructure to the observed transport behavior. Figure 7.8 shows the results of the band structure calculations. A barrier height of ϕ_B=0.22 eV would be expected between CoTiSb and InAlAs for a bandgap E_g^{CoTiSb}=0.68 eV, ΔE_c=0.22, and carrier concentration of $\sim 10^{17}$ e^-/cm^3 within the CoTiSb layer. This carrier concentration and a CoTiSb thickness of 25 nm would show the Fermi level $\sim$0.2 eV from the valence band edge when in contact with p-type III-V, giving an effective barrier height determined mostly by the valence band offset, as seen experimentally.

Using the estimated bandgap of E_g^{CoTiSb}=0.68 eV and the valence band offsets the band alignments between CoTiSb and the III-V compounds InAlAs and

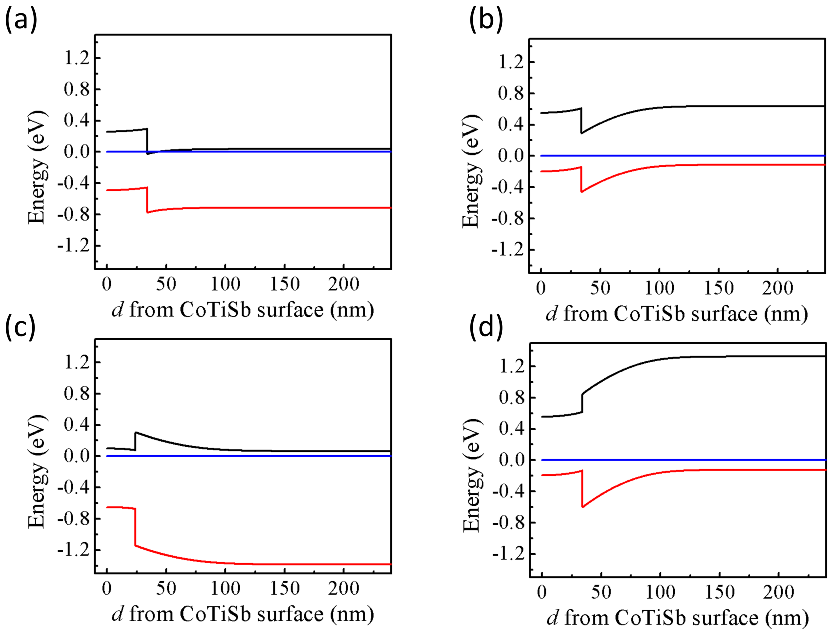

Figure 7.8. 1D Poisson calculated band structures for a 25 nm thick CoTiSb layer with 10^{17} electrons/cm^3 in contact with (a) n-type InGaAs (b) p-type InGaAs, (c) n-type InAlAs, and (d) p-type InAlAs layers. The III-V layers are 400 nm thick low doping (5x10^{16} carriers/cm^2) with a 100 nm graded to high doping layer (3x10^{18} carriers/cm^3) in contact with degenerately doped InP of the same electrical type.

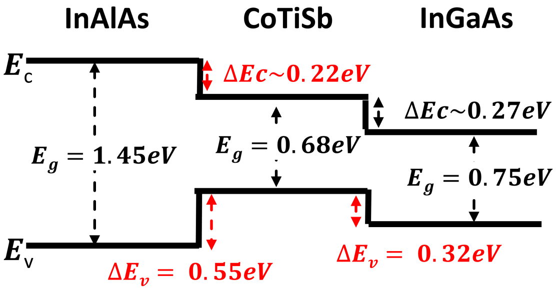

Figure 7.9. Band alignments of CoTiSb with InAlAs and InGaAs combining XPS measurements with electrical transport measurements of heterostructures.

InGaAs can be refined and is presented in Fig. 7.9. Here a type I and type II band alignment is expected with InAlAs and InGaAs respectively. While the inferred bandgap is smaller than that expected by density functional theory (DFT) using the GGA (E_g^{CoTiSb}=1.0 eV) and HSE06 (E_g^{CoTiSb}=1.45 eV) approximations it is consistent with previous estimates from the thermoelectric properties, $E_g \sim$0.57 eV [62]. In addition, a bandgap $\geq$0.6 eV and 0.7 eV was observed in ARPES and STS [60], respectively; all of these are consistent with this result.

7.3 CoTi$_{1-x}$Fe$_x$Sb based GMR structures

CoTi$_{0.7}$Fe$_{0.3}$Sb/CoTiSb/CoTi$_{0.7}$Fe$_{0.3}$Sb heterostructures were grown by MBE using similar methods to those outlined in Chapters 3 and 5. A growth temperature of 280°C was used to minimize reactions with the underlying buffer layer, while still promoting high quality epitaxial growth. Three structures were grown to examine the thickness dependence of the spacer and top electrode layer. For all three structures a bottom electrode thickness of 20 nm was used. The first structure included a 5 nm CoTiSb spacer layer and a 3 nm CoTi$_{0.7}$Fe$_{0.3}$Sb top electrode. The second structure had a thicker CoTiSb spacer layer of 10 nm and, again, a 3 nm CoTi$_{0.7}$Fe$_{0.3}$Sb top electrode. The final structure had the same 10 nm thick spacer layer, but a thicker 5 nm thick CoTi$_{0.7}$Fe$_{0.3}$Sb layer for the top electrode. All three structures were grown on 400 nm thick highly conductive n-type InGaAs/InP(001).

The in-plane magnetization curves for the three structures at 5, 100, and 200 K are shown in Fig. 7.10. In all three structures a double switch could observed at 5 K and 100 K. In addition an exchange bias of over 1000 Oe is is present at 5 K. Notably, for all three devices by 200 K the double switch could no longer be observed indicating that top electrode likely undergoes a magnetic transition between 100 and 200 K for these thin thicknesses. Therefore these devices would only be expected to operate at low temperature.

Each of the heterostructures was fabricated into an MTJ like structure as described in the beginning of the chapter. The fabricated devices were then screened using a 2-point resistance measurement using a probe station. Due to the challenges introduced by the fabrication process a relatively low yield of working devices was observed. Almost all of the devices smaller than $15\times7.5\mu\text{m}^2$ showed open behavior suggesting the SiO_2 layer did not fully lift off on these smallest devices. For the larger devices, over half showed resistances that scaled with area. From each of the processed chips, 5-7 devices were wired up for electrical characterization. For each wired up device, two dI/dV measurements were performed, sweeping the applied bias at a 5000 Oe applied field and sweeping field near zero-bias for MR measurements at room temperature and 2 K following. The 2 K measurements were performed following a zero-field warm up to 320 K and subsequent 5000 Oe field cool. Consistent with SQUID no dependence on field was observed at room temperature. However, at low temperature a selection of devices showed switching behavior consistent with the expected GMR behavior. The GMR of one such device, from structure 2, is shown in Fig. 7.11. While only a modest 0.5% GMR was observed, the field dependence agrees with that expected from the SQUID measurements shown in Fig. 7.10(b).

While the actual GMR results of the $CoTi_{0.7}Fe_{0.3}Sb$ devices is very underwhelming, only one set of samples were grown, and one run of fabrication performed. Clear optimization is necessary within both of these areas. On the growth side, clear 3D spots were visible in the RHEED during growth of the Heusler layers indicating either the stoichiometry or temperature was slightly

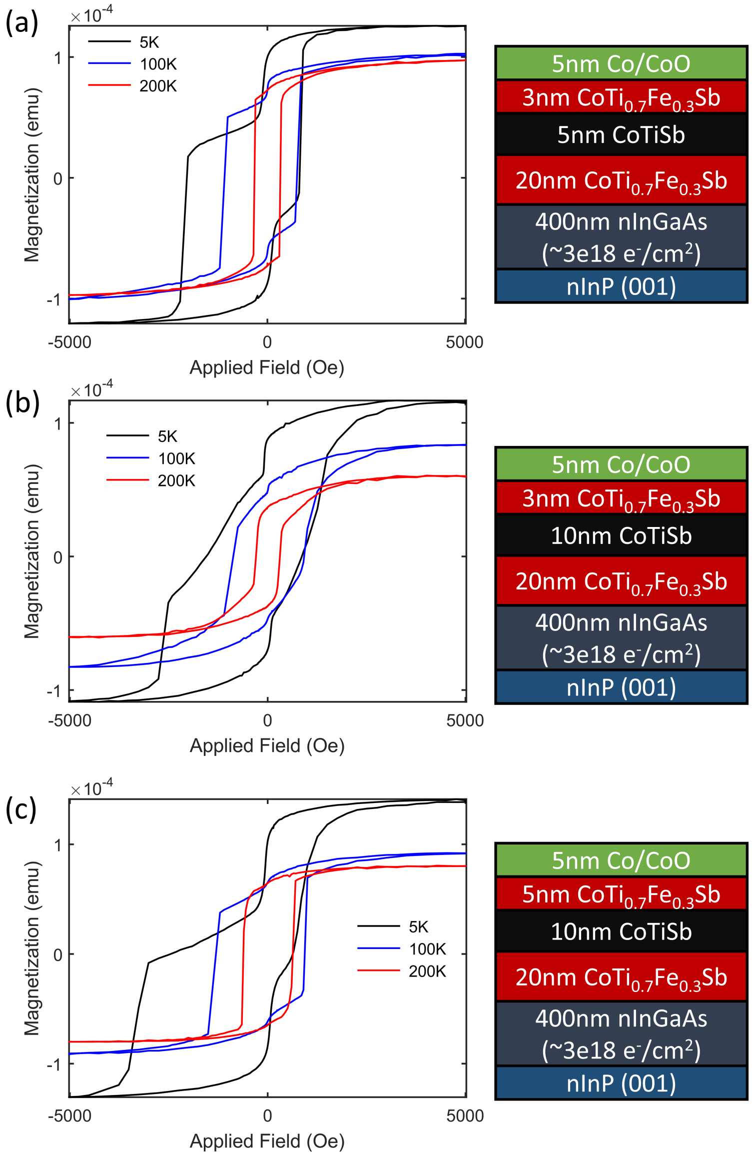

Figure 7.10. In-plane magnetization versus applied field (along the [110] crystallographic direction) curves at 5K, 100K, and 200K for (a) 3 nm thick top electrode with 5 nm CoTiSb spacer, (b) 3 nm thick top electrode with 10 nm CoTiSb spacer, and (c) 5 nm thick top electrode with 10 nm thick CoTiSb spacer. The sample structures are included to the right of each plot.

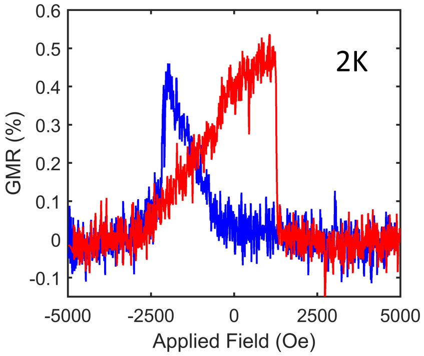

Figure 7.11. GMR trace of $CoTi_{0.7}Fe_{0.3}Sb$/CoTiSb/$CoTi_{0.7}Fe_{0.3}Sb$ GMR structure at 2 K fabricated using the self-aligned process described in the text. GMR is ∼0.5%.

off from the optimal. By adjusting the fluxes slightly a drastic improvement in the surface morphology and roughness (∼1.5 nm) would be expected. Within the fabrication steps, additional steps or adjustment of the process times may be necessary from that originally developed by A. McFadden for Co_2MnSi based MTJs [169] due to the difference in materials system. By optimizing these parameters a much greater % yield as well as GMR could be expected, a necessary requirement for any future applications.

7.4 CoTiSb/NiTiSn Heterostructures

In Chapter 6 the valence-band offsets between the semiconducting half Heusler compounds CoTiSb and NiTiSn were measured. Here a small valence-band offset of ΔE_v=0.17 eV was measured. From this a type I, straddled, band alignment between CoTiSb, the larger bandgap material, and NiTiSn is expected. This alignment is analogous to that seen between AlAs and GaAs. For such an alignment the formation of a two-dimension electron gas (2DEG) at the interface is possible. In addition, due to the difference in total charge between Co and Ni, a difference in the polarity of the compounds may be expected, similar to that seen in the complex oxides [175, 176] and Ge/GaAs interfaces [177]. In a simplified picture, a Ti/Sb layer would carry an effective charge of 1+ (Ti^{4+} + Sb^{3-}), donating the extra electron to Co (Co^{1+}). In contrast a Ti/Sn layer would have a net charge of 0 ($Ti^{4+} + Sn^{4-}$), making Ni carry an effective charge of 0 (Ni^{0}). While this picture is quite simple, from DFT this covalent + ionic picture is expected [61]. This could lead to a polar (CoTiSb) non-polar (NiTiSn) interface similar to that seen in the complex oxides [175]. In this section we explore the transport properties of this semiconductor half-Heusler interface.

Previous work by A. Rice found that NiTiSn layers were achievable on III-V buffer layers only through *in-situ* transfer with an CoTiSb layer used as a diffusion barrier layer between the III-V layer and the NiTiSn layer [166]. Direct growth on the III-V layers leads to a reacted interfacial layer. Growth on a CoTiSb layer on the arsenic decapped III-V layer is possible at lower growth temperatures, but when the substrate is heated to 380°C reactions are visible in both the RHEED and X-ray diffraction (XRD) patterns. It was suggested that small pinholes, occasionally visible in optical micrographs, following arsenic desorption appear to be present through the CoTiSb layer allowing Ni or Sn to react with the underlying buffer layer [166]. Therefore all structures for this section were grown in the III-V MBE system and transferred under UHV to the Heusler MBE for subsequent CoTiSb layer growth. The same seed growth technique discussed in Chapter 3 was used with CoTiSb layers nucleated at 260°C and after 4 nm of growth, continued at 375°C growth temperature. For the NiTiSn layers, a growth temperature of 375°C was used. No evidence of reactions or interdiffusion was observed at the Heusler-Heusler interface using XPS and scanning tunnelling electron microscopy [166]. RHEED images of the CoTiSb and NiTiSn layers are shown in Fig. 7.12(a). Bright streaky (2x1) surface reconstructions could be observed for each layer. XRD showed no signs of additional phase formation, and finite thickness fringes from both layers (Fig. 7.12b).

The sheet resistances of varying thicknesses of NiTiSn on a 25 nm thick CoTiSb buffer layer are shown in Fig. 7.13(a). Also included for comparison is the sheet resistance of a 25 nm thick NiTiSn grown directly on an MgO(001) sub-

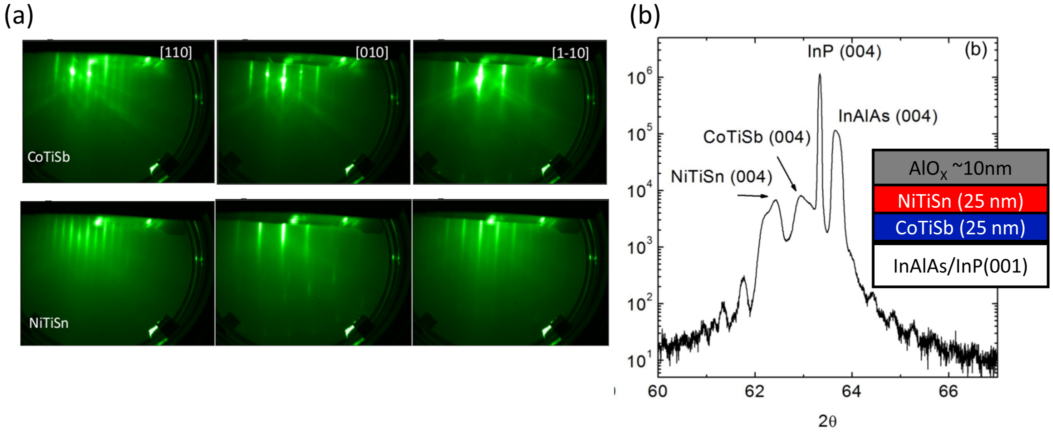

Figure 7.12. (a) RHEED images of CoTiSb and NiTiSn layers grown on InAlAs/InP(001) along the [110], [010], and [-110] crystallographic directions. (b) XRD 2θ-ω scan centered on the (002) reflection. Peaks from the CoTiSb, NiTiSn, InAlAs, and InP layers are all visible. Overlapping thickness fringes from both Heusler layers are also visible.

strate. While the room temperature sheet resistances of the 25 nm thick films are quite comparable, a notably different temperature dependence can be observed from those grown on CoTiSb to the one grown on MgO. NiTiSn films grown on MgO show thermally activated behavior with an increasing resistance for decreasing temperature. In contrast, the NiTiSn grown on CoTiSb layers show metallic transport between 100 and 300 K with a small increase at low temperatures. In addition, the sheet resistance appears to be saturating for thicker NiTiSn layers rather than continuing to drop with thickness. In Fig. 7.13(b) the sheet resitance of a 25 nm thick CoTiSb layer grown on InAlAs/InP(001) is included for comparison. CoTiSb displays an order of magnitude higher resistance at room temperature and over three orders of magnitude higher resistance at 2 K. Thus the observed sheet resistance in the NiTiSn/CoTiSb layers must originate either from the NiTiSn layer, or from the NiTiSn/CoTiSb heterointerface.

To investigate the heterointerface further, heterojunctions with varying number of interfaces were grown. In Fig. 7.14(a) the sheet resistances for heterojunctions of CoTiSb with NiTiSn of varying number of interfaces is shown. In each structure the CoTiSb and NiTiSn layers were 25 nm thick. Here we see

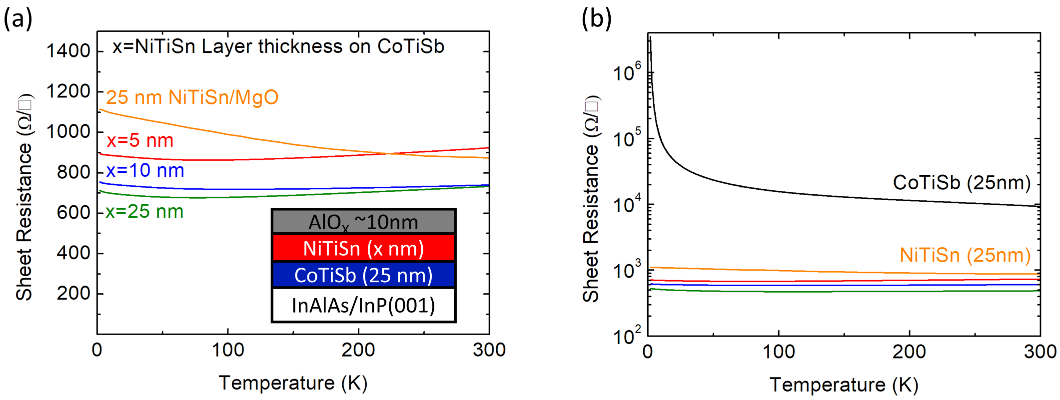

Figure 7.13. (a) Sheet resistance plotted against temperature for 5, 10, and 25 nm thick NiTiSn layers grown on CoTiSb/InAlAs/InP(001). (b) Same plot as (a) but with CoTiSb also included for comparison. CoTiSb is an order of magnitude more resistive at room temperature and even more at low temperature.

a clear decrease in the sheet resistance for each heterointerface introduced. If the resistance was arising only from the bulk of the NiTiSn layer, only a small decrease in resistance would be expected for the two interface structure over the one interface structure because, as was shown previously, CoTiSb is effectively insulating when compared to NiTiSn. However, a systematic decrease in resistance for each additional interface was observed; thus it can be inferred that a form of 2 dimensional transport at the interface is present in this system.

The 2D carrier concentration extracted from the measured hall voltage for heterostructures of varying NiTiSn thicknesses and number of heterointerfaces is shown in Fig. 7.14(b). Both a 3D bulk contribution from NiTiSn as well as a 2D contribution from the interface are expected to contribute to the measured density. Therefore the measured carrier density was fit to a simple model composed of two components: (1) a fix number of charges contribute for each heterointerface and (2) a 3D contribution that depends on the total NiTiSn thickness:

$$n_{2D}^{meas} = A \times n_{2D}^{interface} + t \times n_{3D}^{NiTiSn} \tag{7.4}$$

where A is the number of interfaces and t the total thickness of the NiTiSn layers.

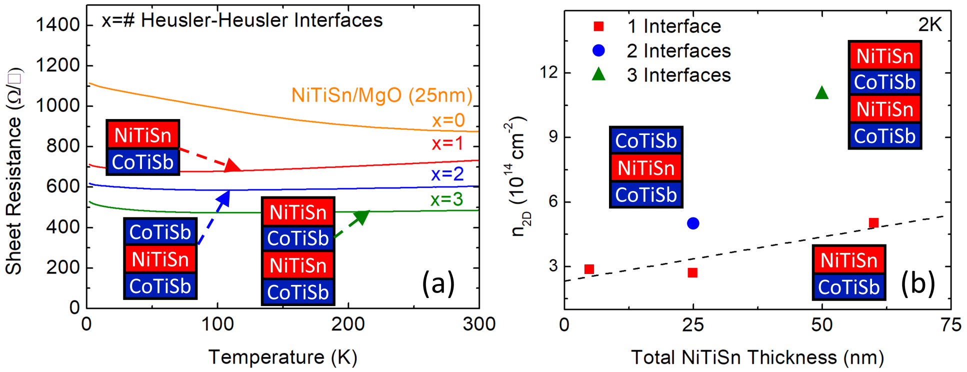

Figure 7.14. (a) Sheet resistance plotted against temperature for CoTiSb/NiTiSn heterostructures with 1, 2, and 3 interfaces. Each CoTiSb and NiTiSn layer is 25 nm thick. (b) Carrier density of each of the films plotted against the total NiTiSn thickness within the heterostructure.

Here a $n_{2D}^{interface}$=2.7×10^{14} carriers/cm^2 and n_{3D}^{NiTiSn}=4×10^{19} carriers/cm^3 was found. The fit for one heterointerface is shown as a dashed line.

Finally, the low temperature magnetoresistance was measured for a one CoTiSb/NiTiSn interface heterostructure and is plotted in Fig. 7.15. Here a zero-field peak could be observed at 2.1 K, As the temperature is increased to 4 K, the magnitude of the peak decreases, with a small zero-field dip being observable at intermediate temperatures, that then disappears. The peak and dip resemble weak-localization and weak anti-localizaiton respectively, which are characteristic of 2D systems. Notably, neither of these features are present in layers of NiTiSn or CoTiSb when grown separately.

While no direct observation of a 2DEG being present at the NiTiSn/CoTiSb interface was made, mounting evidence suggests that interface transport is present. Metallic sheet resistance that decreases, scaling with number of interfaces rather than NiTiSn thickness, is observed. A 2D carrier density of ∼2.7×10^{14} carriers/cm^2 per heterointerface is estimated.

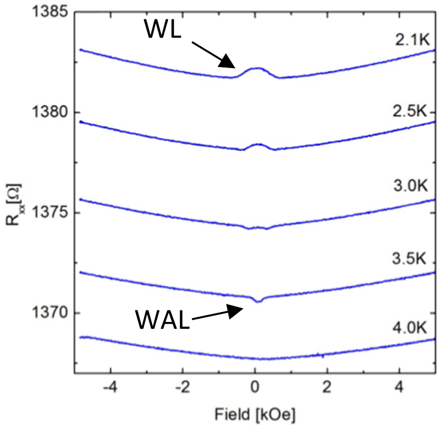

Figure 7.15. Temperature dependence of the magnetoresistance for a 25 nm thick NiTiSn layer on 25 nm thick CoTiSb grown on InAlAs/InP(001). Here the zero-field peak at 2K, possible weak localization, transforms to a zero-field dip, weak antilocalization, as the temperature increases. These effects are possible signatures of 2D transport.

7.5 Summary

The band alignment between CoTiSb and the III-V compounds InAlAs and InGaAs was explored using vertical transport. Here good agreement between the measured valence-band offset and those obtained from transport was found. However, the conduction band offsets predicted by DFT are found to be inconsistent with the transport behavior observed. A smaller bandgap for CoTiSb of 0.68 eV is estimated and used to explain the observed transport behavior.

$Co_{0.7}Fe_{0.3}Sb$/CoTiSb/$CoTi_{0.7}Fe_{0.3}Sb$ giant magnetoresistance (GMR) multilayer structures were successfully grown and the magnetic and preliminary electronic characteristics measured. Here an exchange biased double switch was observed in magnetic hysterisis loops, indicative the heterostructure should behave like a GMR multilayer device. However, due to film surface roughness and challenges introduced by the fabrication process, a relatively low device yield was obtained. Despite the challenges a GMR of ∼0.5% was observed for one of the structures grown.

Finally, the transport properties at the NiTiSn/CoTiSb heterointerface were explored. Here, signatures of interface transport are present, although clear evidence of a true 2DEG are missing.

Chapter 8

Summary and Future Work

8.1 Summary

In this dissertation, the semiconducting half-Heusler, CoTiSb, has been used as a model system to examine the tunability of half-Heusler compound properties as well the interface characteristics with other compounds. In particular, the growth, magnetic, and electronic properties have been investigated.

The semiconductor to metal transition in $\mathrm{Co_{1-x}Ni_xTiSb}$ films was examined using electrical transport, Seebeck measurement, and angle-resolved photoemission spectroscopy (ARPES) measurements. The temperature dependent electrical transport measurements suggest that films of composition $x \leq 0.1$ show transport dominated by thermally activated behavior. Low-energy electron diffraction and scanning tunnelling microscopy demonstrate smooth clean film surfaces are achievable following *ex-situ* transfer of the films, and (3 x 1)-, (2x1)-, and c(2x4)-surface reconstructions of $\mathrm{Co_{1-x}Ni_xTiSb}$ were observed upon Sb cap desorption depending on annealing temperature. ARPES experiments for determining the electronic band structure were performed to investigate the effects of nickel as well as surface reconstruction. For the different reconstructions and compositions, the Γ - Δ - X direction was measured by varying the photon energy between 14 and 150 eV. A surface state could be observed in all photoelectron spectra. The position and shape of the surface state depended on both surface reconstruction and composition. The appearance of the conduction band minimum at the bulk X point below the Fermi level occurs for compositions with x>0.1, suggesting a crossover from semiconductor to metallic behaviour. Finally evidence of Fermi level pinning that depended on surface reconstruction was observed.

The influence of Fe on the structural, electronic, and magnetic properties was studied in CoTi$_{1-x}$Fe$_x$Sb thin films and compared to that expected from density functional theory. The films are epitaxial and single crystalline, as measured by reflection high-energy electron diffraction and X-ray diffraction. Using *in-situ* X-ray photoelectron spectroscopy (XPS), only small changes in the valence band are detected for x≤0.5. For films with x≥0.05, ferromagnetism is observed in SQUID magnetometry with a saturation magnetization that scales linearly with Fe content. A dramatic decrease in the magnetic moment per formula unit occurs when the Fe is substitutionally alloyed on the Co site indicating a strong dependence on the magnetic moment with site occupancy. A crossover from both in-plane and out-of-plane magnetic moments to only in-plane moment occurs for higher concentrations of Fe. Ferromagnetic resonance indicates a transition from weak to strong interaction with a reduction in inhomogeneous broadening as Fe content is increased. Temperature dependent transport reveals a semiconductor to metal transition with thermally activated behavior for x≤0.5. Anomalous Hall effect and large negative magnetoresistance (up to -18.5% at 100 kOe for x=0.3) are observed for higher Fe content films. Evidence of superparamagnetism for x=0.3 and x=0.2 suggests for moderate levels of Fe, demixing of the CoTi$_{1-x}$Fe$_x$Sb films into Fe rich and Fe deficient regions may be present. Atom probe tomography is used to examine the Fe distribution in a x=0.3 film. Statistical analysis reveals a nonhomogeneous distribution of Fe atoms throughout the film, which was used to explain the observed magnetic and electrical behavior.

The valence-band offsets, ΔE_v, between CoTiSb and the lattice-matched

III-Vs $In_{0.53}Ga_{0.47}As$ and $In_{0.52}Al_{0.48}As$, as well as another semiconducting half-Heusler, NiTiSn, heterojunction interfaces have been measured using XPS. Valence-band offsets of 0.30 eV, 0.58 eV, and 0.17 eV were measured for CoTiSb/$In_{0.53}Ga_{0.47}As$, CoTiSb/$In_{0.52}Al_{0.48}As$, and CoTiSb/NiTiSn respectively. By combining these measurements with previously reported XPS ΔE_v ($In_{0.53}Ga_{0.47}As/In_{0.52}Al_{0.48}As$) data, the results suggest that band offset transitivity is satisfied. In addition, the film growth order of the interfaces between CoTiSb and $In_{0.53}Ga_{0.47}As$ and CoTiSb and NiTiSn is explored and does not appear to affect the band offsets. Good agreement is found between the DFT calculated valence-band offsets and those determined from XPS.

Finally, a number of heterostructures including CoTiSb are synthesized, fabricated, and characterized. The measured and calculated band alignments are compared to those inferred from electrical transport measurements performed on diodes of CoTiSb/InAlAs and CoTiSb/InGaAs heterostructures. Effective barrier heights of $\leq$0.05, 0.22, 0.36, and 0.60 eV are found for CoTiSb/n-InGaAs, CoTiSb/n-InAlAs, CoTiSb/p-InGaAs, and CoTiSb/p-InAlAs heterojunctions, respectively. These allow a refinement of the band-alignment expected by decreasing the bandgap of CoTiSb to $\sim$0.7 eV and limiting the carrier concentration of CoTiSb to $\leq 10^{17}$ electrons/cm^3. With these two parameters good agreement is found between the valence band offsets from XPS and vertical transport. GMR multilayer devices incorporating $CoTi_{0.7}Fe_{0.3}Sb$ magnetic electrodes show favorable switching behavior, but require significant development to be used in actual devices. NiTiSn/CoTiSb heterostructures display transport properties suggestive of interface conduction with interface carrier densities of approximately 2.7×10^{14} electrons/cm^2.

8.2 Future Work

This work has demonstrated the tunability of Heusler compounds, showing that both the electronic and magnetic structure can be modified by alloying.

In addition, the interface properties with other compounds has been measured and shown to be in good agreement with DFT calculations, suggesting these theoretical models of Heusler interface properties can be accurate. However this work has only scratched the surface on the integration of Heusler compounds into functional devices. A number of challenges and open questions still need to be addressed.

One of the largest challenges with Heusler thin film growth will continue to be the control of stoichiometry. While careful control of elemental flux helps mitigate this significantly, small deviations are inevitable. These small deviations ultimately lead to in-gap states and lower the effective band-gap. Limited experiments were done for this dissertation examining the existence of a growth window, similar to that used for the MBE growth of III-As and III-Sb compounds. Preliminary results suggest a growth limited regime may exist. However small changes in the Co to Ti flux greatly affect the resulting surface morphology. To be able to grow a truly stoichiometric 1:1:1 compound, using a metal-organic precursor for Ti or Co may enable a strictly self limiting regime. In addition, higher growth temperatures may be favorable, in which case a less reactive buffer layer may be desirable to further reduce anti-site and other intrinsic defects. By reducing in-gap defects a better estimate of the true band gap may be possible. Initial optical measurements showed no clear indication of a band gap between 1 and 1.5 eV where DFT predicts, but did show a slow rise in absorption consistent with in-gap states being present. Transport measurements were suggestive of a smaller band-gap but this may vary with stoichiometry and defect density. Further studies of the optical and electrical characteristics to probe the bandgap as a function of stoichiometry may elucidate whether the smaller observed bandgap is real or a result of in-gap states.

Beyond controlling for stoichiometry and intrinsic disorder, another challenge will be understanding, limiting, and potentially controlling the nano-phase separation that may be present in quatenary half-Heuslers. In the Fe alloyed CoTiSb very little evidence of phase separation was observed in initial characterization.

If not for the superparamagnetic behavior observed, it is likely it would have gone unrecognized. This nano-phase separation was subtle but very measurable using atom probe tomography. If this nano-phase separation is present in other quatenary Heuslers, it has likely gone undetected and may be important to observe and quantify in other systems to use these compounds in devices. While for many applications the phase separation would be undesirable, it could be an interesting direction for Heusler based thermoelectrics. The nano-precipitates could be useful for lowering the thermal conductivity while still maintaining a high electrical resistivity.

Finally, significantly more effort must be placed on the synthesis and characterization of Heusler compound based heterostructures. This work demonstrated a number of simple half-Heusler based heterostructures including diodes, GMR multilayer devices, and semiconducting bilayers. While these devices are interesting as a proof of concept that Heusler compounds can be integrated into functional devices, they do not offer any additional functionality that cannot be achieved with conventional semiconductors and ferromagnets. To achieve multifunctional heterostructures significant development must be done to overcome the challenges encountered by mixing Heusler compounds containing different elements and lattice parameters. Much of this will be in the design, for example lattice parameter and elemental reactivity considerations, while perhaps much more will be in the fabrication as very little is known on the processing of these compounds. With a number of exciting predictions experimentally verified within the last few years, considerable opportunity has emerged to create new multifunctional heterostructures for applications that may not even exist yet.

Bibliography

[1] D. C. Tsui, H. L. Stormer, and A. C. Gossard. Two-Dimensional Magnetotransport in the Extreme Quantum Limit. *Physical Review Letters*, 48 (22):1559–1562, 1982. doi:10.1103/PhysRevLett.48.1559.

[2] T. Graf, C. Felser, and S. S. Parkin. Simple rules for the understanding of Heusler compounds. *Progress in Solid State Chemistry*, 39(1):1–50, 2011. doi:10.1016/j.progsolidstchem.2011.02.001.

[3] C. J. Palmstrøm. Heusler compounds and spintronics. *Progress in Crystal Growth and Characterization of Materials*, 62(2):371–397, 2016. doi:10.1016/j.pcrysgrow.2016.04.020.

[4] S. Picozzi, A. Continenza, and A. J. Freeman. Co_2MnX (X-Si, Ge, Sn) Heusler compounds: An ab initio study of their structural, electronic, and magnetic properties at zero and elevated pressure. *Physical Review B*, 66 (9):094421, 2002. doi:10.1103/PhysRevB.66.094421.

[5] R. D. Groot and F. Mueller. New class of materials: Half-metallic ferromagnets. *Physical Review Letters*, 50(25):2024–2027, 1983.

[6] M. I. Katsnelson, V. Y. Irkhin, L. Chioncel, A. I. Lichtenstein, and R. A. de Groot. Half-metallic ferromagnets: From band structure to many-body effects. *Reviews of Modern Physics*, 80(2):315–378, 2008. doi:10.1103/RevModPhys.80.315.

[7] J. Tobola, J. Pierre, S. Kaprzyk, R. V. Skolozdra, and M. A. Kouacou.

Crossover from semiconductor to magnetic metal in semi-Heusler phases as a function of valence electron concentration. *Journal of Physics: Condensed Matter*, 10(5):1013–1032, 1998. doi:10.1088/0953-8984/10/5/011.

[8] H. C. Kandpal, V. Ksenofontov, M. Wojcik, R. Seshadri, and C. Felser. Electronic structure, magnetism and disorder in the Heusler compound Co_2TiSn. *Journal of Physics D: Applied Physics*, 40(6):1587–1592, 2007. doi:10.1088/0022-3727/40/6/S13.

[9] J. Toboła and J. Pierre. Electronic phase diagram of the XTZ (X=Fe, Co, Ni; T=Ti, V, Zr, Nb, Mn; Z=Sn, Sb) semi-Heusler compounds. *Journal of Alloys and Compounds*, 296(1-2):243–252, 2000. doi:10.1016/S0925-8388(99)00549-6.

[10] W. Al-Sawai, H. Lin, R. Markiewicz, L. A. Wray, Y. Xia, S.-Y. Xu, M. Z. Hasan, and A. Bansil. Topological electronic structure in half-Heusler topological insulators. *Physical Review B*, 82(12):125208, 2010. doi:10.1103/PhysRevB.82.125208.

[11] S. Chadov, X. Qi, J. Kübler, and G. Fecher. Tunable multifunctional topological insulators in ternary Heusler compounds. *Nature Materials*, 9 (7):541–545, 2010. doi:10.1038/nmat2770.

[12] J. A. Logan, S. J. Patel, S. D. Harrington, C. M. Polley, B. D. Schultz, T. Balasubramanian, A. Janotti, A. Mikkelsen, and C. J. Palmstrøm. Observation of a topologically non-trivial surface state in half-Heusler PtLuSb (001) thin films. *Nature Communications*, 7:11993, 2016. doi:10.1038/ncomms11993.

[13] Z. Wang, M. G. Vergniory, S. Kushwaha, M. Hirschberger, E. V. Chulkov, A. Ernst, N. P. Ong, R. J. Cava, and B. A. Bernevig. Time-Reversal Breaking Weyl Fermions In Magnetic Heuslers. *Physical Review Letters*, 117(23):236401, 2016.

[14] G. Chang, S.-Y. Xu, H. Zheng, B. Singh, C.-H. Hsu, I. Belopolski, D. S. Sanchez, G. Bian, N. Alidoust, H. Lin, and M. Z. Hasan. Room-temperature magnetic topological semimetal state in half-metallic Heusler Co_2TiX (X=Si, Ge, or Sn). *Scientific Reports* 6(1):38839, 2016.

[15] J. Winterlik, G. Fecher, A. Thomas, and C. Felser. Superconductivity in palladium-based Heusler compounds. *Physical Review B*, 79(6):1–9, 2009. doi:10.1103/PhysRevB.79.064508.

[16] T. Klimczuk, C. H. Wang, K. Gofryk, F. Ronning, J. Winterlik, G. H. Fecher, J.-C. Griveau, E. Colineau, C. Felser, J. D. Thompson, D. J. Safarik, and R. J. Cava. Superconductivity in the Heusler family of intermetallics. *Physical Review B*, 85(17):174505, 2012. doi:10.1103/PhysRevB.85.174505.

[17] Z. H. Liu, M. Zhang, Y. T. Cui, Y. Q. Zhou, W. H. Wang, G. H. Wu, X. X. Zhang, and G. Xiao. Martensitic transformation and shape memory effect in ferromagnetic Heusler alloy Ni_2FeGa. *Applied Physics Letters*, 82 (3):424–426, 2003. doi:10.1063/1.1534612.

[18] J. W. Dong, J. Xie, and J. Lu. Shape memory and ferromagnetic shape memory effects in single-crystal Ni_2MnGa thin films. *Journal of Applied Physics*, 95(5):2593, 2004.

[19] K. Mastronardi, D. Young, C. C. Wang, P. Khalifah, R. J. Cava, and A. P. Ramirez. Antimonides with the half-Heuslers structure: New thermoelectric materials. *Appl. Phys. Lett.*, 74(10):1415–1417, 1999. doi:10.1063/1.123596.

[20] J. Yang, H. Li, T. Wu, W. Zhang, L. Chen, and J. Yang. Evaluation of half-Heusler compounds as thermoelectric materials based on the calculated electrical transport properties. *Advanced Functional Materials*, 18(19): 2880–2888, 2008. doi:10.1002/adfm.200701369.

[21] S.-W. Kim, Y. Kimura, and Y. Mishima. High temperature thermoelectric properties of TiNiSn-based half-Heusler compounds. *Intermetallics*, 15(3): 349–356, 2007. doi:10.1016/j.intermet.2006.08.008.

[22] P. C. Canfield, J. D. Thompson, W. P. Beyermann, A. Lacerda, M. F. Hundley, E. Peterson, Z. Fisk, and H. R. Ott. Magnetism and heavy fermion-like behavior in the RBiPt series. *Journal of Applied Physics*, 70 (10):5800–5802, 1991. doi:10.1063/1.350141.

[23] J. Pierre, R. Skolozdra, J. Tobola, S. Kaprzyk, C. Hordequin, M. A. Kouacou, I. Karla, R. Currat, and E. Leliévre-Berna. Properties on request in semi-Heusler phases. *Journal of Alloys and Compounds*, 262-263(97):101–107, 1997. doi:10.1016/S0925-8388(97)00337-X.

[24] N. Shutoh and S. Sakurada. Thermoelectric properties of the $\mathrm{Ti}_x(\mathrm{Zr}_{0.5}\mathrm{Hf}_{0.5})_{1-x}\mathrm{NiSn}$ half-Heusler compounds. *Journal of Alloys and Compounds*, 389(1-2):204–208, 2005. doi:10.1016/j.jallcom.2004.05.078.

[25] T. Zhu, C. Fu, H. Xie, Y. Liu, and X. Zhao. High Efficiency Half-Heusler Thermoelectric Materials for Energy Harvesting. *Advanced Energy Materials*, 5(19):1500588, 2015. doi:10.1002/aenm.201500588.

[26] Y. Liu, H. Xie, C. Fu, G. J. Snyder, X. Zhao, and T. Zhu. Demonstration of a phonon-glass electron-crystal strategy in (Hf,Zr)NiSn half-Heusler thermoelectric materials by alloying. *Journal of Materials Chemistry A*, 3 (45):22716–22722, 2015. doi:10.1039/C5TA04418A.

[27] I. Žutić, J. Fabian, and S. Sarma. Spintronics: Fundamentals and applications. *Reviews of modern physics*, 76(2):323–410, 2004.

[28] K. Inomata, S. Okamura, R. Goto, and N. Tezuka. Large Tunneling Magnetoresistance at Room Temperature Using a Heusler Alloy with the B2 Structure. *Japanese Journal of Applied Physics*, 42(Part 2, No. 4B):L419–L422, 2003. doi:10.1143/JJAP.42.L419.

[29] H. Kubota, J. Nakata, M. Oogane, Y. Ando, A. Sakuma, and T. Miyazaki. Large Magnetoresistance in Magnetic Tunnel Junctions Using Co-Mn-Al Full Heusler Alloy. *Japanese Journal of Applied Physics*, 43(No. 7B):L984–L986, 2004. doi:10.1143/JJAP.43.L984.

[30] T. Ishikawa, T. Marukame, K.-i. Matsuda, T. Uemura, M. Arita, and M. Yamamoto. Structural and magnetic properties of epitaxially grown full-Heusler alloy Co_2MnGe thin films deposited using magnetron sputtering. *Journal of Applied Physics*, 99(8):08J110, 2006. doi:10.1063/1.2170980.

[31] T. Taira, T. Ishikawa, N. Itabashi, K.-i. Matsuda, T. Uemura, and M. Yamamoto. Spin-dependent tunnelling characteristics of fully epitaxial magnetic tunnel junctions with a Heusler alloy Co_2MnGe thin film and a MgO barrier. *Journal of Physics D: Applied Physics*, 42(8):084015, 2009. doi:10.1088/0022-3727/42/8/084015.

[32] C. Herbort, E. A. Jorge, and M. Jourdan. Morphology induced magnetoresistance enhancement of tunneling junctions with the Heusler electrode $Co_2Cr_{0.6}Fe_{0.4}Al$. *Applied Physics Letters*, 94(14):142504, 2009. doi:10.1063/1.3114425.

[33] K. Yakushiji, K. Saito, S. Mitani, K. Takanashi, Y. K. Takahashi, and K. Hono. Current-perpendicular-to-plane magnetoresistance in epitaxial $Co_2MnSi/Cr/Co_2MnSi$ trilayers. *Applied Physics Letters*, 88(22):222504, 2006. doi:10.1063/1.2207987.

[34] Y. Sakuraba, T. Iwase, K. Saito, S. Mitani, and K. Takanashi. Enhancement of spin-asymmetry by $L2_1$-ordering in $Co_2MnSi/Cr/Co_2MnSi$ current-perpendicular-to-plane magnetoresistance devices. *Applied Physics Letters*, 94(1):012511, 2009. doi:10.1063/1.3068492.

[35] K. Nikolaev, P. Kolbo, T. Pokhil, X. Peng, Y. Chen, T. Ambrose, and O. Mryasov. All-Heusler alloy current-perpendicular-to-plane gi-

ant magnetoresistance. *Applied Physics Letters*, 94(22):222501, 2009. doi:10.1063/1.3126962.

[36] X. Y. Dong, C. Adelmann, J. Q. Xie, C. J. Palmstrom, X. Lou, J. Strand, P. a. Crowell, J.-P. Barnes, and a. K. Petford-Long. Spin injection from the Heusler alloy Co_2MnGe into $Al_{0.1}Ga_{0.9}As/GaAs$ heterostructures. *Applied Physics Letters*, 86(10):102107, 2005. doi:10.1063/1.1881789.

[37] G. Bona, F. Meier, and M. Taborelli. Spin polarized photoemission from NiMnSb. *Solid State Communications*, 56(4):391–394, 1985.

[38] Y. Miyoshi, Y. Bugoslavsky, M. H. Syed, T. Robinson, L. F. Cohen, L. J. Singh, Z. H. Barber, C. E. a. Grigorescu, S. Gardelis, J. Giapintzakis, and W. Van Roy. Comparison of free surface polarization of NiMnSb and Co_2MnSi. *Applied Physics Letters*, 88(14):142512, 2006. doi:10.1063/1.2193787.

[39] L. J. Singh, Z. H. Barber, Y. Miyoshi, Y. Bugoslavsky, W. R. Branford, and L. F. Cohen. Structural, magnetic, and transport properties of thin films of the Heusler alloy Co_2MnSi. *Applied Physics Letters*, 84(13):2367, 2004. doi:10.1063/1.1690868.

[40] C. T. Tanaka, J. Nowak, and J. S. Moodera. Spin-polarized tunneling in a half-metallic ferromagnet. *Journal of Applied Physics*, 86(11):6239, 1999. doi:10.1063/1.371678.

[41] S. Hashemifar, P. Kratzer, and M. Scheffler. Preserving the Half-Metallicity at the Heusler Alloy $Co_2MnSi(001)$ Surface: A Density Functional Theory Study. *Physical Review Letters*, 94(9):096402, 2005. doi:10.1103/PhysRevLett.94.096402.

[42] K. Nagao, M. Shirai, and Y. Miura. Ab initio calculations of spin polarization at $Co_2CrAl/GaAs$ interfaces. *Journal of Physics: Condensed Matter*, 16(48):S5725–S5728, 2004. doi:10.1088/0953-8984/16/48/036.

[43] T. Block, C. Felser, G. Jakob, J. Ensling, B. Mühling, P. Gütlich, and R. Cava. Large negative magnetoresistance effects in $Co_2Cr_{0.6}Fe_{0.4}Al$. *Journal of Solid State Chemistry*, 176(2):646–651, 2003. doi:10.1016/j.jssc.2003.07.002.

[44] C. Felser and B. Heitkamp. Investigation of a novel material for magnetoelectronics: $Co_2Cr_{0.6}Fe_{0.4}Al$. *Journal of Physics: Condensed Matter*, 7019, 2003.

[45] I. Galanakis. Appearance of half-metallicity in the quaternary Heusler alloys. *Journal of Physics: Condensed Matter*, 16(18):3089–3096, 2004. doi:10.1088/0953-8984/16/18/010.

[46] B. Balke, G. Fecher, H. Kandpal, C. Felser, K. Kobayashi, E. Ikenaga, J.-J. Kim, and S. Ueda. Properties of the quaternary half-metal-type Heusler alloy $Co_2Mn_{1-x}Fe_xSi$. *Physical Review B*, 74(10):104405, 2006. doi:10.1103/PhysRevB.74.104405.

[47] S. Wurmehl, G. H. Fecher, K. Kroth, F. Kronast, H. a. Dürr, Y. Takeda, Y. Saitoh, K. Kobayashi, H.-J. Lin, G. Schönhense, and C. Felser. Electronic structure and spectroscopy of the quaternary Heusler alloy $Co_2Cr_{1-x}Fe_xAl$. *Journal of Physics D: Applied Physics*, 39(5):803–815, 2006. doi:10.1088/0022-3727/39/5/S06.

[48] G. H. Fecher, A. Gloskovskii, K. Kroth, J. Barth, B. Balke, C. Felser, F. Schäfers, M. Mertin, W. Eberhardt, S. Mähl, and O. Schaff. Bulk sensitive photo emission spectroscopy of $C1_b$ compounds. *Journal of Electron Spectroscopy and Related Phenomena*, 156-158:97–101, 2007. doi:10.1016/j.elspec.2006.11.022.

[49] N. Tezuka, N. Ikeda, S. Sugimoto, and K. Inomata. 175% tunnel magnetoresistance at room temperature and high thermal stability using $Co_2FeAl_{0.5}Si_{0.5}$ full-Heusler alloy electrodes. *Applied Physics Letters*, 89 (25):252508, 2006. doi:10.1063/1.2420793.

[50] W. Wang, H. Sukegawa, R. Shan, and K. Inomata. Fabrication of fully epitaxial magnetic tunnel junctions using $L2_1$-ordered $Co_2FeAl_{0.5}Si_{0.5}$ electrodes and their tunneling magnetoresistance characteristics. *Applied Physics Letters*, 93(12):122506, 2008. doi:10.1063/1.2988649.

[51] T. Marukame and M. Yamamoto. Tunnel magnetoresistance in fully epitaxial magnetic tunnel junctions with a full-Heusler alloy thin film of $Co_2Cr_{0.6}Fe_{0.4}Al$ and a MgO tunnel barrier. *Journal of Applied Physics*, 101(8):083906, 2007. doi:10.1063/1.2718284.

[52] R. Shan, H. Sukegawa, W. Wang, M. Kodzuka, T. Furubayashi, T. Ohkubo, S. Mitani, K. Inomata, and K. Hono. Demonstration of Half-Metallicity in Fermi-Level-Tuned Heusler Alloy $Co_2FeAl_{0.5}Si_{0.5}$ at Room Temperature. *Physical Review Letters*, 102(24):246601, 2009. doi:10.1103/PhysRevLett.102.246601.

[53] H. Lin, L. Wray, Y. Xia, S. Xu, S. Jia, R. Cava, A. Bansil, and M. Hasan. Half-Heusler ternary compounds as new multifunctional experimental platforms for topological quantum phenomena. *Nature Mater.*, 9(7):546, 2010. doi:10.1038/nmat2771.

[54] D. Hsieh, Y. Xia, D. Qian, L. Wray, F. Meier, J. Dil, J. Osterwalder, L. Patthey, A. Fedorov, H. Lin, A. Bansil, D. Grauer, Y. Hor, R. Cava, and M. Hasan. Observation of Time-Reversal-Protected Single-Dirac-Cone Topological-Insulator States in Bi_2Te_3 and Sb_2Te_3. *Physical Review Letters*, 103(14):146401, 2009. doi:10.1103/PhysRevLett.103.146401.

[55] P. Bach, A. S. Bader, C. Ruster, C. Gould, C. R. Becker, G. Schmidt, L. W. Molenkamp, W. Weigand, C. Kumpf, E. Umbach, R. Urban, G. Woltersdorf, and B. Heinrich. Molecular-beam epitaxy of the half-Heusler alloy NiMnSb on (In,Ga)As/InP (001). *Applied Physics Letters*, 83(3):521, 2003. doi:10.1063/1.1594286.

[56] X. Dong, J. W. Dong, J. Xie, and T. Shih. Growth temperature controlled

magnetism in molecular beam epitaxially grown Ni_2MnAl Heusler alloy. *Journal of Crystal Growth*, 254:384–389, 2003.

[57] S. J. Patel. *Growth and Electronic Structure of Heusler Compounds for Use in Electron Spin Based Devices*. PhD thesis, University of California - Santa Barbara, 2015.

[58] J. K. Kawasaki, L. I. M. Johansson, B. D. Schultz, and C. J. Palmstrøm. Growth and transport properties of epitaxial lattice matched half Heusler CoTiSb/InAlAs/InP(001) heterostructures. *Applied Physics Letters*, 104 (2):022109, 2014. doi:10.1063/1.4862191.

[59] S. J. Patel, J. K. Kawasaki, J. Logan, B. D. Schultz, J. Adell, B. Thiagarajan, A. Mikkelsen, and C. J. Palmstrøm. Surface and electronic structure of epitaxial PtLuSb (001) thin films. *Applied Physics Letters*, 104(20): 201603, 2014. doi:10.1063/1.4879475.

[60] J. K. Kawasaki. *Epitaxial growth, surface, and electronic properties of unconventional semiconductors: RE-V/III-V nanocomposites and semiconducting Half Heusler alloys*. Thesis, University of California Santa Barbara, 2014.

[61] H. C. Kandpal, C. Felser, and R. Seshadri. Covalent bonding and the nature of band gaps in some half-Heusler compounds. *Journal of Physics D: Applied Physics*, 39(5):776–785, 2006. doi:10.1088/0022-3727/39/5/S02.

[62] P. Qiu, X. Huang, X. Chen, and L. Chen. Enhanced thermoelectric performance by the combination of alloying and doping in TiCoSb-based half-Heusler compounds. *Journal of Applied Physics*, 106(10):103703, 2009. doi:10.1063/1.3238363.

[63] H. Muta, T. Kanemitsu, K. Kurosaki, and S. Yamanaka. High-temperature thermoelectric properties of Nb-doped MNiSn (M=Ti, Zr) half-Heusler compound. *Journal of Alloys and Compounds*, 469(1-2):50–55, 2009. doi:10.1016/j.jallcom.2008.02.041.

[64] B. Balke, J. Barth, M. Schwall, G. H. Fecher, and C. Felser. An Alternative Approach to Improve the Thermoelectric Properties of Half-Heusler Compounds. *Journal of Electronic Materials*, 40(5):702–706, 2011. doi:10.1007/s11664-011-1517-0.

[65] T. Sekimoto, K. Kurosaki, H. Muta, and S. Yamanaka. Thermoelectric properties of Sn-doped TiCoSb half-Heusler compounds. *Journal of Alloys and Compounds*, 407:326–329, 2006. doi:10.1016/j.jallcom.2005.06.036.

[66] M. Zhou, C. Feng, L. Chen, and X. Huang. Effects of partial substitution of Co by Ni on the high-temperature thermoelectric properties of TiCoSb-based half-Heusler compounds. *Journal of Alloys and Compounds*, 391 (1-2):194–197, 2005. doi:10.1016/j.jallcom.2004.07.074.

[67] T. Wu, W. Jiang, X. Li, Y. Zhou, and L. Chen. Thermoelectric properties of p -type Fe-doped TiCoSb half-Heusler compounds. *Journal of Applied Physics*, 102(10):1–6, 2007. doi:10.1063/1.2809377.

[68] K. Gofryk, D. Kaczorowski, T. Plackowski, A. Leithe-Jasper, and Y. Grin. Magnetic and transport properties of rare-earth-based half-Heusler phases RPdBi: Prospective systems for topological quantum phenomena. *Phys. Rev. B.*, 84(035208):1–6, 2011. doi:10.1103/PhysRevB.84.035208.

[69] F. Aliev, N. Brandt, V. Moshchalkov, V. Kozyrkov, R. Skolozdra, and A. Belogorokhov. Gap at the Fermi level in the intermetallic vacancy system RNiSn (R= Ti, Zr, Hf). *Z. Phys. B.*, 75(2):167–171, 1989.

[70] C. , C. Canali, G. Otiaviani, and A. A. Quaranta. A review of some charge transport properties of silicon. *Solid-State Electronics*, 20:77–89, 1977.

[71] N. Y. Sun, Y. Q. Zhang, W. R. Che, J. Qin, and R. Shan. Structural, magnetic, and transport properties of Fe-doped CoTiSb epitaxial thin films. *Journal of Applied Physics*, 118(17):173905, 2015. doi:10.1063/1.4935145.

[72] S. Ouardi, G. H. Fecher, B. Balke, X. Kozina, G. Stryganyuk, C. Felser, S. Lowitzer, D. Ködderitzsch, H. Ebert, and E. Ikenaga. Electronic transport properties of electron- and hole-doped semiconducting $C1_b$ Heusler compounds: $NiTi_{1-x}M_xSn$ (M=Sc,V). *Physical Review B*, 82(8):085108, 2010. doi:10.1103/PhysRevB.82.085108.

[73] S. Öüt and K. M. Rabe. Band gap and stability in the ternary intermetallic compounds NiSn M (M =Ti,Zr,Hf): A first-principles study. *Physical Review B*, 51(16):10443–10453, 1995. doi:10.1103/PhysRevB.51.10443.

[74] Y. G. Yu, X. Zhang, and A. Zunger. Natural off-stoichiometry causes carrier doping in half-Heusler filled tetrahedral structures. *Physical Review B*, 95(8):085201, 2017. doi:10.1103/PhysRevB.95.085201.

[75] B. Balke, G. H. Fecher, A. Gloskovskii, J. Barth, K. Kroth, C. Felser, R. Robert, and A. Weidenkaff. Doped semiconductors as half-metallic materials: Experiments and first-principles calculations of $CoTi_{1-x}M_xSb$ (M=Sc, V, Cr, Mn, Fe). *Physical Review B*, 77(4):045209, 2008. doi:10.1103/PhysRevB.77.045209.

[76] S. Ouardi, G. H. Fecher, C. Felser, M. Schwall, S. S. Naghavi, A. Gloskovskii, B. Balke, J. Hamrle, K. Postava, J. Pištora, S. Ueda, and K. Kobayashi. Electronic structure and optical, mechanical, and transport properties of the pure, electron-doped, and hole-doped Heusler compound CoTiSb. *Physical Review B*, 86(4):045116, 2012. doi:10.1103/PhysRevB.86.045116.

[77] M. Hichour, D. Rached, R. Khenata, M. Rabah, M. Merabet, A. H. Reshak, S. Bin Omran, and R. Ahmed. Theoretical investigations of NiTiSn and CoVSn compounds. *Journal of Physics and Chemistry of Solids*, 73(8): 975–981, 2012. doi:10.1016/j.jpcs.2012.03.014.

[78] J. Schmitt, Z. M. Gibbs, G. J. Snyder, and C. Felser. Resolving the true band gap of ZrNiSn half-Heusler thermoelectric materials. *Mater. Horiz.*, 2(1):68–75, 2015. doi:10.1039/C4MH00142G.

[79] L. L. Wang, L. Miao, Z. Y. Wang, W. Wei, R. Xiong, H. J. Liu, J. Shi, and X. F. Tang. Thermoelectric performance of half-Heusler compounds TiNiSn and TiCoSb. *Journal of Applied Physics*, 105(1):013709, 2009. doi:10.1063/1.3056384.

[80] S. Datta and B. Das. Electronic analog of the electro-optic modulator. *Applied Physics Letters*, 56:665–667, 1990. doi:10.1063/1.102730.

[81] J.-M. Hu, L.-Q. Chen, and C.-W. Nan. Multiferroic Heterostructures Integrating Ferroelectric and Magnetic Materials. *Advanced Materials*, 28(1): 15–39, 2016. doi:10.1002/adma.201502824.

[82] C. J. Palmstrøm. Epitaxy of dissimilar materials. *Annual Review of Materials Science*, 25:389–415, 1995.

[83] T. Jaeger, C. Mix, M. Schwall, X. Kozina, J. Barth, B. Balke, M. Finsterbusch, Y. U. Idzerda, C. Felser, and G. Jakob. Epitaxial growth and thermoelectric properties of TiNiSn and Zr$_{0.5}$Hf$_{0.5}$NiSn thin films. *Thin Solid Films*, 520(3), 2011. doi:10.1016/j.tsf.2011.08.008.

[84] X. Kozina, T. Jaeger, S. Ouardi, A. Gloskowskij, G. Stryganyuk, G. Jakob, T. Sugiyama, E. Ikenaga, G. H. Fecher, and C. Felser. Electronic structure and symmetry of valence states of epitaxial NiTiSn and NiZr$_{0.5}$Hf$_{0.5}$Sn thin films by hard x-ray photoelectron spectroscopy. *Applied Physics Letters*, 99(22):221908, 2011. doi:10.1063/1.3665621.

[85] J. R. Arthur. Interaction of Ga and As$_2$ Molecular Beams with GaAs Surfaces. *Journal of Applied Physics*, 39(8):4032–4034, 1968. doi:10.1063/1.1656901.

[86] S. Hüfner. *Photoelectron Spectroscopy: Principles and Applications*. 2003.

[87] J. Yeh and I. Lindau. Atomic subshell photoionization cross sections and asymmetry parameters: 1 Z 103. *Atomic Data and Nuclear Data Tables*, 32(1):1–155, 1985. doi:10.1016/0092-640X(85)90016-6.

[88] M. P. Seah and W. A. Dench. Quantitative electron spectroscopy of surfaces: A standard data base for electron inelastic mean free paths in solids. *Surface and Interface Analysis*, 1(1):2–11, 1979. doi:10.1002/sia.740010103.

[89] C. N. Berglund and W. E. Spicer. Photoemission Studies of Copper and Silver: Theory. *Physical Review*, 136(4A):A1030–A1044, 1964. doi:10.1103/PhysRev.136.A1030.

[90] S. D. Harrington, J. A. Logan, and J. Osiecki. IgorPro ARPES Code `https://github.com/PalmstromLab/ARPES-Code`

[91] J. R. Waldrop. Measurement of semiconductor heterojunction band discontinuities by x-ray photoemission spectroscopy. *Journal of Vacuum Science & Technology A: Vacuum, Surfaces, and Films*, 3(3):835, 1985. doi:10.1116/1.573326.

[92] D. W. Niles, G. Margaritondo, P. Perfetti, C. Quaresima, and M. Capozi. Heterojunction band discontinuity control by ultrathin intralayers. *Applied Physics Letters*, 47(10):1092–1094, 1985. doi:10.1063/1.96339.

[93] E. A. Kraut, R. Grant, J. R. Waldrop, and S. P. Kowalczyk. Precise Determination of the Valence-Band Edge in X-Ray Photoemission Spectra: Application to Measurement of Semiconductor Interface Potentials. *Physical Review Letters*, 44(24):1620–1623, 1980.

[94] S. Chen, X. Pan, C. Xu, J. Huang, and Z. Ye. X-ray photoelectron spectroscopy study of energy-band alignments of ZnO on buffer layer Lu_2O_3. *Physics Letters A*, 380(7-8):970–972, 2016. doi:10.1016/j.physleta.2015.12.038.

[95] Y. Zhu, N. Jain, D. K. Mohata, S. Datta, D. Lubyshev, J. M. Fastenau, A. K. Liu, and M. K. Hudait. Band offset determination of mixed As/Sb type-II staggered gap heterostructure for n-channel tunnel field

effect transistor application. *Journal of Applied Physics*, 113(2):024319, 2013. doi:10.1063/1.4775606.

[96] S. A. Chambers and T. J. Irwin. Epitaxial growth and band bending of n - and p -type Ge on GaAs(001). *Physical Review B*, 38(11):7484–7492, 1988. doi:10.1103/PhysRevB.38.7484.

[97] S. A. Chambers, Y. Liang, Z. Yu, R. Droopad, J. Ramdani, and K. Eisenbeiser. Band discontinuities at epitaxial $SrTiO_3$/Si(001) heterojunctions. *Applied Physics Letters*, 77(11):1662–1664, 2000. doi:10.1063/1.1310209.

[98] J. Tao, J. W. Chai, Z. Zhang, J. S. Pan, and S. J. Wang. The energy-band alignment at molybdenum disulphide and high- k dielectrics interfaces. *Applied Physics Letters*, 104(23):232110, 2014. doi:10.1063/1.4883865.

[99] U. Resch, N. Esser, Y. Raptis, W. Richter, J. Wasserfall, A. Förster, and D. Westwood. Arsenic passivation of MBE grown GaAs(100): structural and electronic properties of the decapped surfaces. *Surface Science*, 269-270:797–803, 1992. doi:10.1016/0039-6028(92)91351-B.

[100] U. Resch-Esser, N. Esser, B. Brar, and H. Kroemer. Microscopic structure of GaSb(001) c(2x6) surfaces prepared by Sb decapping of MBE-grown samples, 1997.

[101] S. Adachi. *Properties of Group-IV, III-V and II-VI Semiconductors*. John Wiley & Sons, Ltd, Chichester, UK, 2005. ISBN 9780470090343. doi:10.1002/0470090340.

[102] J. Ma, V. I. Hegde, K. Munira, Y. Xie, S. Keshavarz, D. T. Mildebrath, C. Wolverton, A. W. Ghosh, and W. H. Butler. Computational investigation of half-Heusler compounds for spintronics applications. *Physical Review B*, 95(2):024411, 2017. doi:10.1103/PhysRevB.95.024411.

[103] P. A. Lee. Disordered electronic systems. *Reviews of Modern Physics*, 57 (2), 1985.

[104] B. Johs and J. S. Hale. Dielectric function representation by B-splines. *Phys. Status Solidi A*, 205(4):715–719, 2008. doi:10.1002/pssa.200777754.

[105] J. P. Perdew, A. Ruzsinszky, G. I. Csonka, O. A. Vydrov, G. E. Scuseria, L. A. Constantin, X. Zhou, and K. Burke. Restoring the Density-Gradient Expansion for Exchange in Solids and Surfaces. *Physical Review Letters*, 100(13):136406, 2008. doi:10.1103/PhysRevLett.100.136406.

[106] M. L. Cohen and J. R. Chelikowsky. *Electronic Structure and Optical Properties of Semiconductors*, volume 75 of *Springer Series in Solid-State Sciences*. Springer Berlin Heidelberg, Berlin, Heidelberg, 1988. ISBN 978-3-642-97082-5. doi:10.1007/978-3-642-97080-1.

[107] M. Zahedifar and P. Kratzer. Band structure and thermoelectric properties of half-Heusler semiconductors from many-body perturbation theory. *Physical Review B*, 97(3):035204, 2018. doi:10.1103/PhysRevB.97.035204.

[108] Y. Stadnyk, V. A. Romaka, M. Shelyapina, Y. Gorelenko, L. Romaka, D. Fruchart, A. Tkachuk, and V. Chekurin. Impurity band effect on $\mathrm{TiCo}_{1-x}\mathrm{Ni}_x\mathrm{Sb}$ conduction: Donor impurities. *Journal of Alloys and Compounds*, 421(1-2):19–23, 2006. doi:10.1016/j.jallcom.2005.11.008.

[109] L. Romaka, M. Shelyapina, Y. Stadnyk, D. Fruchart, E. Hlil, and V. Romaka. Peculiarity of metalinsulator transition due to composition change in the semiconducting $\mathrm{TiCo}_{1-x}\mathrm{Ni}_x\mathrm{Sb}$ solid solution. *Journal of Alloys and Compounds*, 416(1-2):46–50, 2006. doi:10.1016/j.jallcom.2005.08.051.

[110] V. A. Romaka, M. G. Shelyapina, Y. V. Stadnyk, D. Fruchart, L. P. Romaka, and V. F. Chekurin. Role of the impurity band during the insulator-metal transition as the composition of highly doped and compensated $\mathrm{TiCo}_{1x}\mathrm{Ni}_x\mathrm{Sb}$ semiconductor alloy is varied. Donor impurities. *Semiconductors*, 40(7):776–780, 2006. doi:10.1134/S1063782606070074.

[111] M. Ogawa. Alloying reaction in thin nickel films deposited on GaAs. *Thin Solid Films*, 70(1):181–189, 1980. doi:10.1016/0040-6090(80)90426-5.

[112] S. H. Chen, C. B. Carter, C. J. Palmstrom, and T. Ohashi. Transmission electron microscopy studies on lateral reaction of GaAs with Ni. *Applied Physics Letters*, 48(12):803, 1986. doi:10.1063/1.96675.

[113] L. Offernes, P. Ravindran, and A. Kjekshus. Electronic structure and chemical bonding in half-Heusler phases. *Journal of Alloys and Compounds*, 439 (1-2):37–54, 2007. doi:10.1016/j.jallcom.2006.08.316.

[114] M. T. Sieger, T. Miller, and T.-C. Chiang. Reflection high-energy electron diffraction and photoemission study of GaSb(100) reconstructions. *Scientific Reports*, 61:38839, 1995. doi:10.1038/srep38839.

[115] I. Vitomirov, A. Raisanen, and A. Finnefrock. Geometric ordering, surface chemistry, band bending, and work function at decapped GaAs (100) surfaces. *Physical Review B*, 46(20), 1992.

[116] S. J. Patel, J. A. Logan, S. D. Harrington, B. D. Schultz, and C. J. Palmstrøm. Surface reconstructions and transport of epitaxial PtLuSb (001) thin films grown by MBE. *Journal of Crystal Growth*, 436(001):145–149, 2016. doi:10.1016/j.jcrysgro.2015.12.003.

[117] R. A. de Groot, F. M. Mueller, P. G. V. Engen, and K. H. J. Buschow. New class of materials: Half-metallic ferromagnets. *Physical Review Letters*, 50: 2024–2027, 1983. doi:10.1103/PhysRevLett.50.2024.

[118] K. Kroth, B. Balke, G. H. Fecher, V. Ksenofontov, C. Felser, and H.-J. Lin. Diluted magnetic semiconductors with high Curie temperature based on $C1_b$ compounds: $CoTi_{1-x}Fe_xSb$. *Applied Physics Letters*, 89(20):202509, 2006. doi:10.1063/1.2388876.

[119] P. Hohenberg and W. Kohn. Inhomogeneous Electron Gas. *Physical Review*, 136(3B):B864–B871, 1964. doi:10.1103/PhysRev.136.B864.

[120] W. Kohn and L. J. Sham. Self-Consistent Equations Including Exchange and Correlation Effects. *Physical Review*, 140(4A):A1133–A1138, 1965. doi:10.1103/PhysRev.140.A1133.

[121] G. Kresse and J. Furthmüller. Efficient iterative schemes for ab initio total-energy calculations using a plane-wave basis set. *Physical Review B*, 54(16):11169–11186, 1996. doi:10.1103/PhysRevB.54.11169.

[122] G. Kresse and J. Furthmüller. Efficiency of ab-initio total energy calculations for metals and semiconductors using a plane-wave basis set. *Computational Materials Science*, 6(1):15–50, 1996. doi:10.1016/0927-0256(96)00008-0.

[123] P. E. Blöchl. Projector augmented-wave method. *Physical Review B*, 50 (24):17953–17979, 1994. doi:10.1103/PhysRevB.50.17953.

[124] G. Kresse and D. Joubert. From ultrasoft pseudopotentials to the projector augmented-wave method. *Physical Review B*, 59(3):1758–1775, 1999. doi:10.1103/PhysRevB.59.1758.

[125] A. Zunger, S.-H. Wei, L. G. Ferreira, and J. E. Bernard. Special quasirandom structures. *Physical Review Letters*, 65(3):353–356, 1990. doi:10.1103/PhysRevLett.65.353.

[126] A. van de Walle, P. Tiwary, M. de Jong, D. Olmsted, M. Asta, A. Dick, D. Shin, Y. Wang, L.-Q. Chen, and Z.-K. Liu. Efficient stochastic generation of special quasirandom structures. *Calphad*, 42:13–18, 2013. doi:10.1016/j.calphad.2013.06.006.

[127] K. C. Hass, L. C. Davis, and A. Zunger. Electronic structure of random $Al_{0.5}Ga_{0.5}As$ alloys: Test of the “special-quasirandom-structures” description . *Physical Review B*, 42(6):3757–3760, 1990. doi:10.1103/PhysRevB.42.3757.

[128] G. Ghosh, A. van de Walle, and M. Asta. First-principles calculations of the structural and thermodynamic properties of bcc, fcc and hcp solid solutions in the AlTM (TM=Ti, Zr and Hf) systems: A comparison of cluster expansion and supercell methods. *Acta Materialia*, 56(13):3202–3221, 2008. doi:10.1016/j.actamat.2008.03.006.

[129] D. Shin, R. Arróyave, Z.-K. Liu, and A. Van de Walle. Thermodynamic properties of binary hcp solution phases from special quasirandom structures. *Physical Review B*, 74(2):024204, 2006. doi:10.1103/PhysRevB.74.024204.

[130] S. D. Harrington, A. Sharan, A. D. Rice, J. A. Logan, A. P. McFadden, M. Pendharkar, D. J. Pennachio, N. S. Wilson, Z. Gui, A. Janotti, and C. J. Palmstrøm. Valence-band offsets of CoTiSb/$In_{0.53}Ga_{0.47}$ As and CoTiSb/$In_{0.52}Al_{0.48}$As heterojunctions. *Applied Physics Letters*, 111(6): 061605, 2017. doi:10.1063/1.4985200.

[131] H. Ohno, A. Shen, F. Matsukura, A. Oiwa, A. Endo, S. Katsumoto, and Y. Iye. (Ga,Mn)As: A new diluted magnetic semiconductor based on GaAs. *Applied Physics Letters*, 69(3):363–365, 1996. doi:10.1063/1.118061.

[132] S. D. Harrington, A. D. Rice, T. L. Brown-Heft, B. Bonef, A. Sharan, A. P. McFadden, J. A. Logan, M. Pendharkar, M. M. Feldman, O. Mercan, A. G. Petukhov, A. Janotti, L. Colakerol Arslan, and C. J. Palmstrøm. Growth, electrical, structural, and magnetic properties of half-Heusler $CoTi_{1-x}Fe_xSb$. *Physical Review Materials*, 2(1):014406, 2018. doi:10.1103/PhysRevMaterials.2.014406.

[133] P. Stamenov and J. M. D. Coey. Sample size, position, and structure effects on magnetization measurements using second-order gradiometer pickup coils. *Review of Scientific Instruments*, 77(1):015106, 2006. doi:10.1063/1.2149190.

[134] D. Orgassa, H. Fujiwara, T. C. Schulthess, and W. H. Butler. Disorder dependence of the magnetic moment of the half-metallic ferromagnet NiMnSb from first principles. *Journal of Applied Physics*, 87(9):5870–5871, 2000. doi:10.1063/1.372550.

[135] M. Endo, S. Kanai, S. Ikeda, F. Matsukura, and H. Ohno. Electric-field effects on thickness dependent magnetic anisotropy of sputtered

MgO/$Co_{40}Fe_{40}B_{20}$/Ta structures. *Applied Physics Letters*, 96(21):212503, 2010. doi:10.1063/1.3429592.

[136] M. J. Pechan, C. Yu, D. Carr, and C. J. Palmstrøm. Remarkable strain-induced magnetic anisotropy in epitaxial Co_2MnGa (001) films. *Journal of Magnetism and Magnetic Materials*, 286(SPEC. ISS.):340–345, 2005. doi:10.1016/j.jmmm.2004.09.090.

[137] J. J. Krebs, B. T. Jonker, and G. A. Prinz. Properties of Fe single-crystal films grown on (100)GaAs by molecular-beam epitaxy. *Journal of Applied Physics*, 61(7):2596–2599, 1987. doi:10.1063/1.337886.

[138] G. Wastlbauer and J. A. C. Bland. Structural and magnetic properties of ultrathin epitaxial Fe films on GaAs(001) and related semiconductor substrates. *Advances in Physics*, 54(2):137–219, 2005. doi:10.1080/00018730500112000.

[139] N. I. Kourov, V. V. Marchenkov, A. V. Korolev, L. A. Stashkova, S. M. Emel'yanova, and H. W. Weber. Specific features of the properties of half-metallic ferromagnetic Heusler alloys Fe_2MnAl, Fe_2MnSi, and Co_2MnAl. *Physics of the Solid State*, 57(4):700–708, 2015. doi:10.1134/S1063783415040149.

[140] Z. Liu, X. Ma, F. Meng, and G. Wu. Magnetic and anomalous transport properties in Fe_2MnAl. *Journal of Alloys and Compounds*, 509(7):3219–3222, 2011. doi:10.1016/j.jallcom.2010.12.070.

[141] N. Nagaosa, J. Sinova, S. Onoda, A. H. MacDonald, and N. P. Ong. Anomalous Hall effect. *Reviews of Modern Physics*, 82(2):1539–1592, 2010. doi:10.1103/RevModPhys.82.1539.

[142] Y. Tian, L. Ye, and X. Jin. Proper Scaling of the Anomalous Hall Effect. *Physical Review Letters*, 103(8):087206, 2009. doi:10.1103/PhysRevLett.103.087206.

[143] C. P. Bean and J. D. Livingston. Superparamagnetism. *Journal of Applied Physics*, 30(4):S120–S129, 1959. doi:10.1063/1.2185850.

[144] J. M. Mena, H. G. Schoberth, T. Gruhn, and H. Emmerich. Nanophase separation in CoSb-based half-Heusler thermoelectrics: A multiscale simulation study. *Phys. Status Solidi A*, 213(3):706–715, 2016. doi:10.1002/pssa.201532457.

[145] V. A. Dinh, K. Sato, and H. Katayama-Yoshida. First principle study of spinodal decomposition thermodynamics in half-heusler alloy $\mathrm{CoTi}_{1-x}\mathrm{Fe}_x\mathrm{Sb}$. *Journal of Superconductivity and Novel Magnetism*, 23 (1):75–78, 2010. doi:10.1007/s10948-009-0573-7.

[146] D. Larson, E. Marquis, P. Rice, T. Prosa, B. Geiser, S.-H. Yang, and S. Parkin. Manganese diffusion in annealed magnetic tunnel junctions with MgO tunnel barriers. *Scripta Materialia*, 64(7):673–676, 2011. doi:10.1016/j.scriptamat.2010.12.021.

[147] H. Bouchikhaoui, P. Stender, D. Akemeier, D. Baither, K. Hono, A. Hütten, and G. Schmitz. On the role of Ta cap in the recrystallization process of CoFeB layers. *Applied Physics Letters*, 103(14):142412, 2013. doi:10.1063/1.4824033.

[148] K. Thompson, D. Lawrence, D. Larson, J. Olson, T. Kelly, and B. Gorman. In situ site-specific specimen preparation for atom probe tomography. *Ultramicroscopy*, 107(2-3):131–139, 2007. doi:10.1016/j.ultramic.2006.06.008.

[149] F. Vurpillot, B. Gault, B. P. Geiser, and D. Larson. Reconstructing atom probe data: A review. *Ultramicroscopy*, 132:19–30, 2013. doi:10.1016/j.ultramic.2013.03.010.

[150] B. Bonef, H. Boukari, A. Grenier, I. Mouton, P.-H. Jouneau, H. Kinjo, and S. Kuroda. Atomic Scale Structural Characterization of Epitaxial

(Cd,Cr)Te Magnetic Semiconductor. *Microscopy and Microanalysis*, 23 (04):717–723, 2017. doi:10.1017/S1431927617000642.

[151] J. Zhou, J. Odqvist, M. Thuvander, and P. Hedström. Quantitative Evaluation of Spinodal Decomposition in Fe-Cr by Atom Probe Tomography and Radial Distribution Function Analysis. *Microscopy and Microanalysis*, 19(03):665–675, 2013. doi:10.1017/S1431927613000470.

[152] J. Hernández-Saz, M. Herrera, F. J. Delgado, S. Duguay, T. Philippe, M. Gonzalez, J. Abell, R. J. Walters, and S. I. Molina. Atom-scale compositional distribution in InAlAsSb-based triple junction solar cells by atom probe tomography. *Nanotechnology*, 27(30):305402, 2016. doi:10.1088/0957-4484/27/30/305402.

[153] H. Kroemer. Heterostructure devices: A device physicist looks at interfaces. *Surface Science*, 132(1-3):543–576, 1983. doi:10.1016/0039-6028(83)90561-7.

[154] A. Seidl, A. Görling, P. Vogl, J. A. Majewski, and M. Levy. Generalized Kohn-Sham schemes and the band-gap problem. *Physical Review B*, 53 (7):3764–3774, 1996. doi:10.1103/PhysRevB.53.3764.

[155] J. Heyd, G. E. Scuseria, and M. Ernzerhof. Hybrid functionals based on a screened Coulomb potential. *Journal of Chemical Physics*, 118(18):8207–8215, 2003. doi:10.1063/1.1564060.

[156] J. Heyd, G. E. Scuseria, and M. Ernzerhof. Erratum: Hybrid functionals based on a screened Coulomb potential. *The Journal of Chemical Physics*, 124(21):219906, 2006. doi:10.1063/1.2204597.

[157] J. P. Perdew, K. Burke, and M. Ernzerhof. Generalized Gradient Approximation Made Simple. doi:10.1103/PhysRevLett.77.3865.

[158] A. Janotti and C. G. Van de Walle. Absolute deformation potentials and band alignment of wurtzite ZnO, MgO, and CdO. *Physical Review B*, 75 (12):121201, 2007. doi:10.1103/PhysRevB.75.121201.

[159] I. M. Vitomitrov, A. Raisanen, A. C. Finnefrock, R. E. Viturro, L. J. Brillson, P. D. Kirchner, G. D. Pettit, and J. M. Woodall. Geometric ordering, surface chemistry, band bending, and work function at decapped GaAs(100) surfaces. *Physical Review B*, 46(20):13293, 1992.

[160] J. R. Waldrop, E. A. Kraut, C. W. Farley, and R. W. Grant. Measurement of InP/$In_{0.53}Ga_{0.47}As$ and $In_{0.53}Ga_{0.47}As$/$In_{0.52}Al_{0.48}$ As heterojunction band offsets by x-ray photoemission spectroscopy. *Journal of Applied Physics*, 69(1):372–378, 1991. doi:10.1063/1.347724.

[161] J. L. Lyons, A. Janotti, and C. G. Van de Walle. Role of Si and Ge as impurities in ZnO. *Physical Review B*, 80(20):205113, 2009. doi:10.1103/PhysRevB.80.205113.

[162] A. Janotti, J. L. Lyons, and C. G. Van De Walle. Hybrid functional calculations of native point defects in InN. *Phys. Status Solidi A*, 209(1): 65–70, 2012. doi:10.1002/pssa.201100216.

[163] R. Magri, S. Froyen, and A. Zunger. Electronic structure and density of states of the random $Al_{0.5}Ga_{0.5}As$, $GaAs_{0.5}P_{0.5}$, and $Ga_{0.5}In_{0.5}As$ semiconductor alloys. *Physical Review B*, 44(15):7947–7964, 1991. doi:10.1103/PhysRevB.44.7947.

[164] P. Qiu, J. Yang, X. Huang, X. Chen, and L. Chen. Effect of antisite defects on band structure and thermoelectric performance of ZrNiSn half-Heusler alloys. *Applied Physics Letters*, 96(15):152105, 2010. doi:10.1063/1.3396981.

[165] J. K. Kawasaki, T. Neulinger, R. Timm, M. Hjort, A. a. Zakharov, A. Mikkelsen, B. D. Schultz, and C. J. Palmstrom. Epitaxial growth and surface studies of the Half Heusler compound NiTiSn (001). *Journal of Vacuum Science & Technology B: Microelectronics and Nanometer Structures*, 31(4):04D106, 2013. doi:10.1116/1.4807715.

[166] A. Rice. *Semiconducting Half-Heusler Systems Grown by Molecular Beam Epitaxy*. PhD thesis, University of California - Santa Barbara, 2017.

[167] A. P. McFadden, T. Brown-Heft, D. Pennachio, N. S. Wilson, J. A. Logan, and C. J. Palmstrøm. Oxygen migration in epitaxial CoFe/MgO/Co_2MnSi magnetic tunnel junctions. *Journal of Applied Physics*, 122(11):113902, 2017. doi:10.1063/1.5003089.

[168] A. Rice, J. Kawasaki, N. Verma, D. Pennachio, B. Schultz, and C. Palmstrøm. Structural and electronic properties of molecular beam epitaxially grown Ni_{1+x}TiSn films. *Journal of Crystal Growth*, 467:71–76, 2017. doi:10.1016/j.jcrysgro.2017.03.015.

[169] A. P. McFadden. *Heusler Compound Heterostructures and Epitaxial Magnetic Tunnel Junctions for Spintronic Applications*. PhD thesis, 2017.

[170] H. Tamura, A. Yoshida, S. Muto, and S. Hasuo. Schottky Barrier Height of Al/n-$In_{0.53}Ga_{0.47}As$ and Nb/n-$In_{0.53}Ga_{0.47}As$ Diodes. *Japanese Journal of Applied Physics*, 26(Part 2, No. 1):L7–L9, 1987. doi:10.1143/JJAP.26.L7.

[171] S. Mehari, A. Gavrilov, S. Cohen, P. Shekhter, M. Eizenberg, and D. Ritter. Measurement of the Schottky barrier height between Ni-InGaAs alloy and $In_{0.53}Ga_{0.47}As$. *Applied Physics Letters*, 101(7):072103, 2012. doi:10.1063/1.4746254.

[172] R. Wang, M. Xu, P. D. Ye, and R. Huang. Schottky-barrier height modulation of metal/$In_{0.53}Ga_{0.47}As$ interfaces by insertion of atomic-layer deposited ultrathin Al_2O_3. *Journal of Vacuum Science & Technology B: Microelectronics and Nanometer Structures*, 29(4):041206, 2011. doi:10.1116/1.3610972.

[173] L. Chauhan, S. Gupta, P. Jaiswal, N. Bhat, S. Shivashankar, and G. Hughes. Modification of metal-InGaAs Schottky barrier behaviour by atomic layer deposition of ultra-thin Al_2O_3 interlayers. *Thin Solid Films*, 589:264–267, 2015. doi:10.1016/j.tsf.2015.05.046.

[174] L. Sadwick, C. Kim, K. Tan, and D. Streit. Schottky barrier heights of n-type and p-type $Al_{0.48}In_{0.52}As$. *IEEE Electron Device Letters*, 12(11): 626–628, 1991. doi:10.1109/55.119219.

[175] A. Ohtomo, D. A. Muller, J. L. Grazul, and H. Y. Hwang. Artificial charge-modulationin atomic-scale perovskite titanate superlattices. *Nature*, 419 (6905):378–380, 2002. doi:10.1038/nature00977.

[176] A. Ohtomo and H. Y. Hwang. A high-mobility electron gas at the $LaAlO_3/SrTiO_3$ heterointerface. *Nature*, 427(6973):423–426, 2004. doi:10.1038/nature02308.

[177] W. R. Frensley and H. Kroemer. Theory of the energy-band lineup at an abrupt semiconductor heterojunction. *Physical Review B*, 16(6):2642–2652, 1977. doi:10.1103/PhysRevB.16.2642.